AN EXPERIMENTAL INVESTIGATION OF FLOW OVER SIMPLE BLUNT BODIES AT A MACH NUMBER OF 5.8

Thesis by

Eugene M. Wisenbaker

In Partial Fulfillment of the Requirements

For the Degree of

Aeronautical Engineer

California Institute of Technology

Pasadena, California

1957

ACKNOWLEDGMENTS

The author wishes to express sincere appreciation to Professor Lester Lees who first saw the need for this work and who gave so freely of his time and knowledge in helping carry it to completion. He is also indebted to Dr. James Kendall, Mr. Robert E. Oliver, and Mr. Paul Baloga for their invaluable help and suggestions, to Mr. Sam Roman and the rest of the GALCIT hypersonic wind tunnel staff without whose help the tunnel could not have been run, to Mrs. Elizabeth Fox who typed the manuscript, to Mrs. H. Van Gieson who aided in numerous ways with the many procedural details, and to Mr. George Carlson who so skillfully made the models.

A special debt of gratitude is also due the Bureau of Aeronautics of the Navy Department which supported the entire three years of graduate study.

ABSTRACT

Shock stand-off distances and shock shapes were measured and/or observed for a series of 14 blunt-nosed bodies at a Mach number of 5.8 and Reynolds number per inch of 2.22×10^5. Nine of these bodies had hemisphere-segment noses designed to include the entire range of possible nose radii of curvature from flat-faced to hemispherical. Two models characterized by sharp shoulders and concave hemisphere-segment noses were also tested. Three additional models representing the round-shouldered, flat-faced type completed the set of 14. All models had cylindrical afterbodies 1.50 inches in diameter, and were yawed at angles of 0, 4, and 8 degrees.

Stand-off distances are compared to the theoretical predictions of Hayes, Probstein, and Heybey where applicable, and shock shape is compared to that given by Hayes for the body with infinite nose radius of curvature. Results of the stand-off distance comparisons varied from under prediction by a factor of two to over prediction by the same amount. Hayes' shock shape approximated that actually observed very closely. It was generally found that body shape in the sonic region greatly influenced the shock shape and stand-off distance.

Static pressure distributions were measured on three representative bodies selected as follows: (1) a hemisphere-segment body having a ratio of nose radius to base diameter of 1.30 and falling in the middle of the range from hemisphere to flat-nosed; (2) a flat-faced body with sharp shoulder; and (3) a flat-faced body with a rounded shoulder of 5/16 inch radius. Pressures very close to stagnation values generally were found to be present over a large area of the nose in the case of the flat-faced body. Rounding of the shoulder tended to reduce values of $C_p/C_{p_{max}}$ below those observed at corresponding points on the completely flat-faced body, except in the region near

the body axis. The pressure distributions are compared where applicable with the modified Newtonian approximation and with Probstein's approximation to $C_p/C_{p_{max}}$ for zero angle of yaw. Agreement with the modified Newtonian values was generally good near the axis, but deteriorated rapidly in the shoulder regions, except in the case of the rounded shoulder body.

LIST OF SYMBOLS

a	speed of sound, feet per second
C_p	pressure coefficient, $\frac{p - p_\infty}{\frac{1}{2}\rho_\infty U_\infty^2}$, dimensionless
D	diameter of afterbody, inches
h	nose rise, also referred to as the maximum height of hemisphere segment, inches
k	density ratio across a normal shock, $\frac{\rho_1}{\rho_2}$, dimensionless
M	Mach number, dimensionless
p	pressure, pounds per square inch
r	shoulder radius, inches
R	nose radius of curvature, inches
S	distance measured along model surface from the longitudinal axis, inches
S^*	distance to sonic point measured along body surface, inches
U_∞	free stream velocity, feet/sec.
y	coordinate distance from longitudinal axis, inches
α	angle of yaw, degrees
δ_1	shock standoff distance measured along longitudinal axis, inches
δ_2	shock standoff distance measured as the shortest distance from the sonic point on the shock to the body, inches
$\delta_{H(M)}$	shock standoff distance measured along extended body axis for hemisphere-cylinder as a function of Mach number, divided by afterbody diameter, dimensionless.
θ_*	oblique shock angle at which sonic flow first occurs behind the shock, degrees
ρ	air density, lb. sec.^{2}/ft.^{4}

Subscripts

$(\ )_1$	measured along longitudinal axis of the model
$(\ )_2$	measured from sonic point on shock

$( )_{\infty}$ free stream conditions

$( )_{*}$ conditions at sonic line or sonic point

$( )_{max}$ maximum or stagnation value

I. INTRODUCTION

The problem of aerodynamic heating is one among many facing the engineer since the perfection of such high thrust devices as the jet engine and the rocket motor have made flight at hypersonic speeds possible. Just as the so called "sonic" barrier forced profound changes in aircraft design following World War II, it is now apparent that the "thermal" barrier in its turn will force missiles and rockets to take on configurations somewhat different from those of today's conventional aircraft.

In recent years a tremendous effort toward the solution of this aerodynamic heating problem has been made, and it is becoming increasingly evident that the answer lies in some form of blunt-nosed body which due to its "bluntness" is free of the sharp shoulders and points which do not lend themselves readily to the installation of heat removal equipment. It also appears that Nature is aware of the aerodynamicist's troubles, for it provides an additional dividend as an inducement to the selection of the blunt-nosed body for use at hypersonic speeds. As pointed out by Eggers, Resinkoff, and Dennis (Ref. 1) this added advantage is that of minimum drag for a given length provided the body is not too blunt.

It is the purpose of this investigation to study a particularly simple class of bodies for which some theoretical calculations have already been made by Probstein (Ref. 2), Hayes (Ref. 3), Serbin (Ref. 4), and Heybey (Ref. 5). Time and available facilities also limited the investigations to a nominal Mach number of 5.8 as dictated by the use of Leg 1 of the GALCIT 5 x 5 inch hypersonic wind tunnel.

The bodies chosen are of two types, the first having hemisphere-segment noses and cylindrical afterbodies. These nose shapes were selected to cover the complete range from the true hemisphere to the flat-faced or infinite nose radius body, as well as to permit a brief investigation of the flow over a concave nose. There were eleven models of this type tested. The only body shape parameter in this case is the radius of curvature of the nose. The second type of body had a flat nose, cylindrical afterbody, and rounded shoulder. Three models were investigated in this class, and if the flat-faced model and the true hemisphere are thought of as being limiting cases of shoulder rounding, there were effectively five bodies available for analysis. Here again there is only one body shape parameter.

The investigation itself proceeded along two distinct lines. The first was a study of shock shape and stand-off distance from schlieren photographs of flow over the various hemisphere-segment and round-shouldered bodies. The second consisted of a study of surface pressure distributions over the nose and in the shoulder region of one flat-faced body, one hemisphere-segment body falling in the mid-range between the flat-faced and hemispherical, and one round-shouldered body. Wherever possible an attempt was made to compare the measured surface pressures with the Newtonian approximation in the form proposed by Lees (Ref. 6) as well as to compare them with the Probstein approximation (Ref. 2).

II. EQUIPMENT AND PROCEDURE

A. Wind Tunnel

The GALCIT 5 x 5 inch hypersonic wind tunnel (Leg 1) was used exclusively in this investigation. This tunnel is of the continuous flow, closed-return type, and can be operated at reservoir pressures between approximately one and six atmospheres.

The test section Mach number of Leg 1 is nominally 5.8, and the reservoir pressure and temperature were 88.7 pounds per square inch absolute and 225 deg. F respectively. These conditions correspond to a Reynolds number per inch of 2.22×10^5, and insured no condensation in the test section.

A schematic of the entire wind tunnel installation is shown in Fig. 1, and two views of the test section with a model mounted in it can be seen in Fig. 2.

B. Models

The fourteen dummy models used in the schlieren studies were machined from solid brass stock. Each model was originally made with an afterbody diameter of 1.50 inches. Because of difficulties encountered in starting the flow, however, the concave-nosed bodies were subsequently machined down to an afterbody diameter of 1.25 inches. Nine of the models had noses of hemisphere-segments ranging in radius of curvature from 0.75 inches (a complete hemisphere) to infinity (flat). Three additional models had flat noses with rounded shoulders of 1/8, 3/16, and 5/16 inch radii. The two remaining bodies had concave nose radii of one and two inches to make a total of fourteen bodies. A photograph

showing the complete array of models is shown in Fig. 3, and dimensioned drawings showing the details of their construction can be seen in Figs. 4 and 5.

Three pressure models were also constructed of brass. These models consisted of one flat-nosed body (infinite radius of curvature), one hemisphere-segment body (1.95 inch nose radius of curvature), and one flat-nosed, round-shouldered body (5/16 inch shoulder radius). A photograph of these models can be seen in Fig. 6. Pressure orifices 0.016 inch in diameter were drilled in the face and just beyond the shoulder of each model in the positions indicated in Fig. 7. The rounded shoulder model had 10 orifices, while the other two a total of nine each. The orifices were drilled normal to the body surface along one of three equally spaced, meridional planes. These 0.016 inch orifices joined larger passages drilled to intersect them from the rear of the model. (See Fig. 8.) Into each of these larger passages was silver soldered a short length of stainless steel tubing to which saran plastic tubing could be attached. The saran plastic tubes served as a flexible link between the model and the multiple manometer board from which the pressure measurements were taken.

The dummy models were sting-mounted in the tunnel and were screwed directly into the sting. The nose of each model was located approximately $22\frac{1}{2}$ inches down the tunnel from the throat, and very nearly in the center of the observation port through which the schlieren light path shone. The sting itself

was mounted on two vertical struts which extended through the roof of the test section. These struts are 3 5/8 inches apart and are attached to a drive and counter mechanism above the test section. A change of one unit on the counter corresponds to 0.001 inch vertical displacement of the struts, so that it was possible to set any angle of yaw accurately from outside the tunnel even while the tunnel was in operation. All dummy models were tested at angles of yaw of 0, 4, and 8 degrees, and in additional two models were yawed to 12 and 16 degrees.

The pressure models were mounted on the same sting and in approximately the same manner. The only difference in mounting was the interposition of an accurately machined shaft and sleeve between the model and the sting, which permitted rotation of the model about its own axis. This mounting allowed each pressure orifice to fall twice on each of the three equally spaced meridional planes for each complete model revolution. A set screw prevented model rotation after positioning. The saran plastic tubes were tightly wired to the sting and were led out of the tunnel approximately two feet downstream of the model.

Each pressure model was also tested at 0, 4, and 8 degrees of yaw.

C. Test Procedure

Once each dummy model was mounted in the tunnel as described above, an interval of approximately 10 minutes was required to allow the reservoir pressure and temperature to stabilize to the desired values. When tunnel conditions were steady a schlieren photograph was taken at each angle of yaw.

The schlieren photographs were subsequently developed and became the basis of the schlieren studies.

The pressure models were initially placed in the tunnel with the model axis coinciding as nearly with the tunnel axis as possible. The face of the model was approximately $21\frac{1}{2}$ inches down stream of the throat. The saran plastic tubes had previously been secured to the model and pressure checked for leaks. The ends of these tubes were led aft and out of the tunnel through a special port. They were then connected to the manometers, and again the system was checked for leaks. The base of the model had been scribed every thirty degrees to permit accurate model rotation, and one of the three meridional planes designated the base or reference plane.

Once the tunnel was closed and started, it was allowed to run initially from one to one and one half hours to allow conditions to stabilize. Pressure readings were then made at angles of yaw of -8, -4, 0, +4, and +8 degrees. (Because of the axial symmetry of the model the effect of both negative and positive angles of yaw was simply to cut in half the number of rotations required to obtain an apparent model rotation of 12 times.) The test section was then bypassed, the model rotated 30 degrees, and the above procedure repeated after about a 15 minute wait to allow the reservoir pressure and temperature and the manometers to stabilize. This process continued until six rotations had been made and led to a complete set of pressure readings along the intersections of six equally spaced meridional planes with the nose of the model. These pressure data were recorded for later reduction and plotting.

III. DISCUSSION AND RESULTS

A. Schlieren Studies

1. General

The schlieren photographs resulting from the dummy model wind tunnel runs are displayed in Figs. 9 through 53. Because of the large number of photographs taken during this investigation it was decided to limit the actual shock shape and stand-off distance measurements to the unyawed cases only. The remaining photographs are presented to show graphically the effect of angle of yaw on the shocks, but no further comment is intended.

Chronologically, the first measurement made was the stand-off distance of the shock from the nose of the body, δ_1, measured along the extended longitudinal body axis. These measurements were made as accurately as possible on the GALCIT Kodak contour projector to a projected scale which was ten times that of the photograph. The results of these measurements are tabulated in the non-dimensional form in the table on the next page, together with the theoretical predictions of Probstein (Ref. 2), Hayes (Ref. 3), and Heybey (Ref. 5) where applicable.

2. Hemisphere-Segment Bodies (Sharp Shoulders)

Fig. 54 is a plot of the stand-off distances divided by afterbody diameter, $\frac{\delta_1}{D}$, versus the nose radius of curvature divided by the afterbody diameter, $\frac{R}{D}$, for the nine hemisphere-segment bodies with convex noses. In Fig. 55 $\frac{\delta_1}{D}$ is plotted against the reciprocal of $\frac{R}{D}$. In each of these two plots straight line regions were discovered. Reference to Fig. 54 will show that $\frac{\delta_1}{D}$ is a linear function of $\frac{R}{D}$ in the region where the bodies were most

R/D	r/D	δ_1/D Measured	δ_1/D Probstein	δ_1/D Hayes	δ_1/D Heybey
0.500	-	0.080	-	0.0937	0.0700
0.567	-	0.090	-	-	-
0.727	-	0.115	-	-	-
0.920	-	0.145	-	-	-
1.300	-	0.181	-	-	-
1.907	-	0.208	-	-	-
2.880	-	0.226	-	-	-
5.733	-	0.246	-	-	-
∞	-	0.269	0.210	0.498	-
-	0.083	0.237	-	-	-
-	0.125	0.217	-	-	-
-	0.208	0.190	-	-	-

nearly hemispherical. Fig. 55 shows $\frac{\delta_1}{D}$ to be a linear function of the reciprocal of $\frac{R}{D}$ throughout the remainder of the range of hemisphere-segment bodies with the exception of the region in the vicinity of the flat-nosed body. The foregoing observations immediately suggest that the hemisphere-segment bodies can be separated into two sub-categories which it appears natural to refer to as "the near-hemisphere bodies" and the "nearly flat-faced bodies".

a. Near-Hemisphere Bodies

Three of the nine models tested fall in the near-hemisphere category. It has been shown by Oliver (Ref. 7) that the body sonic point on the hemisphere falls at approximately 45 degrees of arc away from the body axis. Reference to Fig. 4 will show that the three near-hemisphere bodies tested included 90, 62, and 44 degrees of arc. The body sonic point on the first two bodies definitely was on the hemisphere-segment nose, and on the third model the sonic point was just beginning to appear at the shoulder. Beyond the sonic point it should be possible to alter the body shape without affecting the flow upstream in the subsonic shock layer. It should even be possible to take any hemisphere-segment and add material to the afterbody portion so as to make it a true hemisphere-cylinder without affecting the stand-off distance, δ_1 . In that case the nose radius of curvature will remain the same but the afterbody diameter of this fictitious hemisphere-cylinder will be increased from its former value of D to twice the nose radius, 2R. Assuming that the stand-off distance divided by afterbody diameter can somehow be calculated or measured for a true hemisphere and is some function of the Mach number, $\delta_H(M)$,

then $\delta_H(M) = \frac{\delta_1}{2R}$ or $\delta_1 = 2\delta_H(M)R$. Dividing through by the afterbody diameter of the real hemisphere segment, D, $\frac{\delta_1}{D} = 2\delta_H(M)\frac{R}{D}$. For any Mach number, however, $\delta_H(M)$ is a constant and $\frac{\delta_1}{D}$, therefore, must be a linear function of R/D in the near hemisphere case.

It is interesting to check the above results with the measured values from this investigation. $\delta_H(5.8)$ was found to be 0.80. Therefore $\frac{\delta_1}{D} = 2(0.80)\frac{R}{D}$. For the body where R/D equalled 0.727 $\frac{\delta_1}{D} = (0.16)(0.727) = 0.116$. A measured value of 0.115 was obtained. If $\frac{\delta_1}{D}$ as a function of R/D is taken directly from the plot on Fig. 54 it is found that

$$\frac{\delta_1}{D} = 0.003 + 0.154\frac{R}{D}$$

and if the constant term is neglected $\frac{\delta_1}{D} = 0.154\frac{R}{D}$, which is approximately the same relation obtained previously.

b. Nearly Flat-Faced Bodies

When the hemisphere-segment nose includes less than 45 degrees between the body axis and a radial to the shoulder, the body sonic point remains fixed at the shoulder. This positioning of the sonic point at the shoulder is the main characteristic of the nearly flat-faced bodies. A simple explanation of the fact that $\frac{\delta_1}{D}$ varies almost inversely as $\frac{R}{D}$ for the smaller values of $\frac{R}{D}$ in this region cannot be given at present. A number of interesting results, however, were obtained.

Reference to Fig. 55 and a few simple calculations lead to the relation

$$\frac{\delta_1}{D} = 0.265 - \frac{0.1095}{R/D}$$

for the range $0.727 < \frac{R}{D} < 2.880$. In the sub-range $0.727 < \frac{R}{D} < 1.50$

the shock sonic point is still between the shoulder region and the body axis, but moves toward the shoulder as $\frac{R}{D}$ is increased. Somewhere near $\frac{R}{D}$ of 1.50 the shock sonic point has reached the shoulder region. It is evident that some sort of continuous transition takes place as $\frac{R}{D}$ increases, and that there is no sharp line of demarcation between the near-hemisphere and nearly flat-faced bodies. It is fortunate, however, that the relation

$$\frac{\delta_1}{D} = 0.265 - \frac{0.1095}{R/D}$$

bridges this gap.

A careful study of the schlieren photographs indicates that for $2.880 \leq \frac{R}{D} \leq \infty$ the shock shape was very nearly circular inside the shoulder region and did not change with $\frac{R}{D}$. Since the shock shape is independent of nose radius of curvature for values of R/D greater than 2.880 it is obvious that the stand-off distance, δ_1, can be computed simply by subtracting the nose rise (maximum height of the hemisphere segment) from the stand-off distance, δ_1, of the flat-faced body. This computation is shown in Fig. 56, and yields the relation

$$\frac{\delta_1}{D} = 0.269 - h$$

or

$$\frac{\delta_1}{D} = 0.269 - \frac{R}{D} + \sqrt{\left(\frac{R}{D}\right)^2 - 0.250}$$

This relation gives $\frac{\delta_1}{D}$ exactly in the region R/D greater than 2.880 and is reasonably accurate throughout the entire region of R/D greater than 1.50.

The constant stand-off distance in the shoulder region is

another important result applying in the range $1.30 \leqslant \frac{R}{D} \leqslant \infty$. In this range it was found that a line perpendicular to the shock at the point where sonic flow occurs just behind the shock in all cases intersects the shoulder very nearly, if not exactly. This fact would seem to confirm a concept first proposed by Busemann and later discussed by Moeckel (Ref. 8). They compare the region between the shock sonic point and the body sonic point to a channel "throat". With this concept in mind it is apparent that the shock positions itself at the shoulder so as to provide sufficient area for all of the fluid passing through the shock into the subsonic shock layer to pass out of the region through this "throat". For this reason the throat height δ_2 was obtained for all bodies, and plotted as the $\frac{\delta_2}{D}$ curve on Fig. 54. In all cases δ_2 was defined as the shortest distance between the sonic point on the shock and the body. For R/D greater than 1.30 this distance corresponded to a sonic point to sonic point measurement, but it should be kept in mind that for the near-hemisphere bodies and those in the transition region the shortest distance from the shock sonic point to the body is not a sonic point to sonic point measurement.

As expected from the statements above $\frac{\delta_2}{D}$ is a horizontal straight line for all values of R/D greater than 1.30. It is also of interest to note that below $R/D = 1.30$ $\frac{\delta_2}{D}$ varies linearly with R/D. At $R/D = 1.30$ there is a sharp "knee" in the $\frac{\delta_2}{D}$ curve. Reference to Fig. 13 will show that when $R/D = 1.30$ the shock is almost concentric with the nose of the body. Fig. 4 also shows that for $R/D = 1.30$ the surface of the nose of the body at the shoulder is at an angle of 67 degrees to the body axis. For $M_\infty = 5.8$ the

bow shock is inclined at 66 degrees 25 minutes to the body axis at the sonic point and the shock layer can, therefore, be thought of as bounded by a parallel-walled channel. For values of R/D greater than 1.30 the channel converges ahead of the shoulder and diverges behind it. For bodies where R/D is less than 1.30 the channel is already diverging by the time the shoulder is reached, and the minimum area or "throat" cannot occur at the shoulder. It was observed that for values of R/D less than 1.30 the shock sonic point moves away from the shoulder region in the direction of the body axis, and δ_2 compensates for this fact by decreasing linearly with R/D. This, briefly, seems to explain the underlying reason for the sharp break in the $\frac{\delta_2}{D}$ curve at R/D = 1.30.

The two concave nosed models were added when it was theorized that shock shape and stand off distance measured from a plane normal to the longitudinal axis through the shoulders of the model would be no different from that observed for the flat-nosed body. This supposition was indeed found to be correct. Because of tunnel starting difficulties the concave models had to be reduced in afterbody diameter from 1.50 inches to 1.25 inches. However, if the flat-nosed body schlieren photograph and either of the concave-nosed body photographs are projected to the same scale and superimposed it is impossible to notice any difference in shock shape or standoff distance.

By utilizing the concept of a "throat" at the shoulder the one dimensional equations of motion (and in particular conservation of mass) can be applied to the nearly flat-faced bodies,

since conditions upstream of the shock and at the shoulder are known or can be calculated. The calculations carried out in Appendix A are an attempt to predict δ_2/D from just such a mass balance as suggested above. Three assumptions which could possibly lead to errors are involved. The first assumption is that the sonic line is straight. The second assumption is that the velocity vector in the shoulder region is perpendicular to the sonic line, and the third is that the density ratio across the shock is the same as for a normal shock. Actually the third assumption need not be made if some approximate shock shape is assumed, but the resulting integral required this author to resort to a numerical method for its evaluation, and the result was substantially the same as if the shock had been assumed normal. It is also felt that the second assumption does not lead to any great error since the assumed velocity vector could only differ from the actual velocity by a factor equal to the cosine of a small angle.

The result of this calculation is considered fairly good in view of the assumptions made. The actual measured value of δ_2/D is 0.186. The calculated value is 0.1978. An error of 6.3 per cent is made. Admittedly this result may have been a fortunate circumstance which applies only at Mach 5.8.

The extension of this calculation to the prediction of δ_1/D is obvious. The only missing link is a reasonably accurate estimation of the shock shape. Hayes (Ref. 3) provides one, and its correspondence to that actually observed is shown in Fig. 57. Correctly positioning the shock in the shoulder region will provide a fairly acceptable stand off distance estimation at all other points.

The results of this estimate can be seen in Appendix A where $\frac{\delta_1}{D}$ is calculated to be 0.255 compared to the measured value of 0.269.

2. Rounded Shoulder Bodies

The next step in the schlieren studies was to plot δ_1/D versus the shoulder radius divided by afterbody diameter, r/D, for the three rounded shoulder models. The two limiting cases of the hemisphere and the flat-nosed model were also added since they properly can belong to either class of body. This plot appears in Fig. 58, and again a straight line relationship between δ_1/D and r/D is observed. As before this can easily be expressed analytically as

$$\delta_1/D = 0.269 - 0.380\,(r/D)$$

for the entire range of r/D at $M_\infty = 5.8$. The important result here is that increased shoulder rounding causes a linear decrease in shock stand-off distance. Reference to Figs. 45, 46, and 47 will also show the effect of shoulder rounding to be that of causing a decrease in shock radius of curvature.

B. Pressure Studies

1. General

Since Oliver (Ref. 7) and to some extent Machell and O'Bryant (Ref. 9) had previously gathered very good pressure data on the hemisphere it was decided not to repeat their work. The intermediate model selected for testing had an R/D of 1.30. The flat-nosed body and a representative rounded shoulder body comprised the remaining two pressure models.

The results of these pressure measurements are plotted in Figs. 59 through 73 in the form $C_p/C_{p_{max}}$ versus S/D, where S is the distance measured from the longitudinal body axis along the face of the body. In all cases where applicable the half plane which assumed a more advanced or upstream position in the flow is plotted on the positive or right side of the S/D = 0 axis.

In each case $C_p/C_{p_{max}}$ is plotted for the intersection of three meridional planes with the nose and afterbody of the model. These planes are a vertical plane, a horizontal plane, and a plane $\pm$ 30 degrees away from the vertical plane. In addition $C_p/C_{p_{max}}$ was also plotted for the R/D = 1.30 model along a plane $\pm$ 60° from the vertical plane. In all cases the pressure distributions are plotted for 0, 4, and 8 degrees of yaw on the same figure in order to show the effects of yawing the model.

The two pressure orifices located beyond the shoulder were not intended to be a means of studying surface pressure distributions along the afterbody, but rather to show that the sonic point generally occurred in the vicinity of the sharp shoulder for the R/D = 1.30 and R/D = ∞ models. Intuitively this result is expected. For this reason all pressure curves were extrapolated from the data point corresponding to the last pressure orifice on the face out to $C_p/C_{p_{max}}$ of 0.517, or the sonic pressure ratio, at the shoulder. No attempt was made to extrapolate the curves any further in the R/D = 1.30 and R/D = ∞ cases because of the fact that the exact nature of the flow between the shoulder and the first pressure orifice beyond the shoulder could not be deduced from the schlieren photographs. It is likely that a weak oblique shock originating at or just behind the

shoulder is present, but this shock is invisible at these low tunnel densities.

2. Unyawed Bodies

a. Flat Nose (R/D = ∞)

In general it can be seen by referring to Figs. 59 through 62 that the Newtonian approximation for the flat-nosed body is completely accurate only near the axis of the body. Beyond S/D of approximately 0.2 in the unyawed case the observed pressure ratios begin to fall away from the $C_p/C_{p_{max}}$ of 1.0 which the Newtonian approximation predicts. However, when it is considered that it is not until after S/D = 0.433 that the actual pressure ratios begin to deviate more than 10 per cent from the Newtonian approximation the agreement is considered fairly good. Immediately beyond the shoulder some slight over-expansion is observed in this case. The Newtonian approximation also predicts zero pressure ratio beyond the shoulder, which is not too far from that actually measured.

Probstein's (Ref. 2) pressure distribution prediction is compared to the observed distribution in Fig. 62. Here agreement is good near the axis and again near the shoulder, but tends to be low at intermediate points.

An attempt to predict the pressure ratio by a Prandtl-Meyer expansion around the shoulder immediately encounters difficulty. Experience has shown that in some cases this method can be applied to such axially symmetric flows as those being considered here with fair results. If an expansion through 90^o is assumed it is felt that a minimum possible pressure ratio could be found below which the actual pressure ratio could not go. For this reason the Prandtl-Meyer prediction was calculated and found to be $C_p/C_{p_{max}} = -0.0231$

as opposed to a measured value of -0.0148 at the orifice nearest the shoulder.

b. Hemisphere-Segment (R/D = 1.30)

In this case it is seen by reference to Figs. 63 through 67 that $C_p/C_{p_{max}}$ falls off more rapidly than for the flat-nose case. This result is exactly as expected because of the rounding of the nose. Here again reference to Fig. 67 shows that the Newtonian approximation predicts pressure ratios which are higher beyond S/D = 0.2 than those observed. Actually a better fit which holds over a wider range of S/D is the Newtonian approximation with the Busemann correction for centrifugal force. This correspondence can be seen in Fig. 67 where it is apparent that $C_p/C_{p_{max}}$ does not depart from that predicted by the theory more than 10 per cent until the flow is quite close to the shoulder. It is felt that the justification for applying the Busemann correction here lies in the fact that the shock is very nearly concentric with the nose of the body.

In this case no over-expansion is observed, and the Prandtl-Meyer expansion method gives $C_p/C_{p_{max}} = -0.0176$ beyond the shoulder, as compared to a value of 0.00122 actually measured.

c. Rounded Shoulder (r/D = 0.208)

Figs. 68 through 71 display the results of the surface pressure investigations over the rounded shoulder body. The modified Newtonian approximation is almost exact until the influence of the rounded shoulder is felt. Fig. 71 compares the modified Newtonian approximation (without the Busemann correction) to the observed pressure distribution. As in the other cases it can be seen that $C_p/C_{p_{max}}$ falls off more rapidly than predicted by the Newtonian

method in the shoulder region. No over-expansion is noted for this body and the Prandtl-Meyer expansion predicts $C_p/C_{p_{max}}$ = -0.00239 as opposed to the measured value of +0.0287.

3. Yawed Bodies

It is apparent from a study of the surface pressure curves in Figs. 59 through 61, Figs. 63 through 66, and Figs. 69 through 70 that no particularly startling results were obtained by yawing the models to angles of 4 and 8 degrees. For these relatively small angles the pressures deviated a noticeable but not marked amount from those observed in the unyawed cases. As expected the stagnation point or region of maximum pressure moved off the axis a slight distance onto the more advanced portion of the nose. Deviations from the unyawed pressure measurements were largest in the shoulder regions. There was no evidence to indicate that the sonic point on either of the two bodies with sharp corners had moved away from the shoulders, and the pressure curves were again extrapolated to $C_p/C_{p_{max}}$ = 0.517 at the S/D point corresponding to the shoulder.

It should also be noted that pressures observed along the horizontal plane of all three models when yawed do not at any point rise as high as the maximum pressure. This result is to be expected if the horizontal plane does not contain the maximum pressure point.

4. Comparison of Surface Pressures Between Bodies

In order to compare the surface pressures over one body to those of another, $C_p/C_{p_{max}}$ is plotted versus S/S*, where S* is the distance along the face of the model to the sonic point. Fig.

72 is such a plot for the flat-nosed body, $R/D = \infty$, the round-nosed body, $R/D = 1.30$, and a hemispherical nosed body, $R/D = 0.500$ (Oliver (Ref. 7)). Fig. 73 is a similar plot comparing the flat-nosed square-shoulder body to one with a flat nose and rounded shoulder. Both of these plots clearly show the effect of rounding either the shoulder or the nose itself to be that of causing a more rapidly falling surface pressure, except in the sonic region. It should be kept in mind that the effect of dividing by S^* rather than D is to distort the body dimensions since S^* is different for each body. However, to plot in the usual manner leads to an equally distorted presentation in which comparisons are just as difficult to make. The main advantage to be derived from plotting in this manner is that it appears to be the most effective means of comparing the way in which the pressures fall off to the sonic value among different bodies.

CONCLUSIONS

Based upon the foregoing results it is concluded that for the conditions under which this investigation was conducted

(1) The shock shape and stand-off distance depend on body shape in the vicinity of the body sonic point, and to a lesser extent than originally supposed on body shape away from the sonic point.

(2) That there are three distinct ranges of R/D in which δ_1/D can be written as a simple, but different, function of R/D.

(3) That for the flat-faced, sharp-shouldered body it is possible to compute the stand-off distance of the shock at the shoulder as well as at the body axis by applying the simple, one-dimensional continuity equation and Hayes' theoretical shock shape approximation. The resulting computations are in fair agreement with the experimental values obtained in this investigation.

(4) That the modified Newtonian approximation can be expected to give good results near the axis of the models tested, fair results between the region near the axis and the region near the shoulder, and poor results close to the shoulder except in the rounded shoulder case. Here the Newtonian prediction is surprisingly good even in the shoulder region.

(5) That the Probstein approximation to $C_p/C_{p_{max}}$ is, as Probstein contends, valid only near the body axis.

REFERENCES

1. Eggers, A. J., Resnikoff, M. M., and Dennis, D. H.: Bodies of Revolution Having Minimum Drag at High Supersonic Airspeeds. NACA TN 3666, February 1956.

2. Probstein, R. F.: Inviscid Flow in the Stagnation Point Region of Very Blunt-Nosed Bodies at Hypersonic Flight Speeds. WADC-TN 56-395, September 1956.

3. Hayes, W. D.: Some Aspects of Hypersonic Flow. Ramo-Wooldridge Corporation, January 1955.

4. Serbin, H.: Hypersonic, Non-Viscous Flow Around a Circular Disk Normal to the Stream. RAND Corporation RM-1713, May 3, 1956.

5. Heybey, W. H.: Shock Distances in Front of Symmetrical Bodies. NAVORD Report 3594, December 1953.

6. Lees, L.: Hypersonic Flow. Institute of the Aeronautical Sciences reprint of an article first appearing in the Fifth International Aeronautical Conference, 1955.

7. Oliver, R. E.: An Experimental Investigation of Flow over Simple Blunt Bodies at a Nominal Mach Number of 5.8. GALCIT Hypersonic Research Project, Memorandum No. 26, June 1, 1955.

8. Moeckel, W. E.: Approximate Method for Predicting Form and Location of Detached Shock Waves of Plane or Axially Symmetric Bodies. NACA TN 1921, July 1949.

9. Machell, R. M. and O'Bryant, W. T.: An Experimental Investigation of Flow over Blunt-Nosed Cones at a Mach Number of 5.8. GALCIT Hypersonic Research Project, Memorandum No. 32, June 15, 1956.

APPENDIX

(A) Calculation of $\frac{\delta_2}{D}$ and $\frac{\delta_1}{D}$ by mass balance and Hayes' theoretical shock shape. (Flat nose body - $\frac{R}{D} = \infty$)

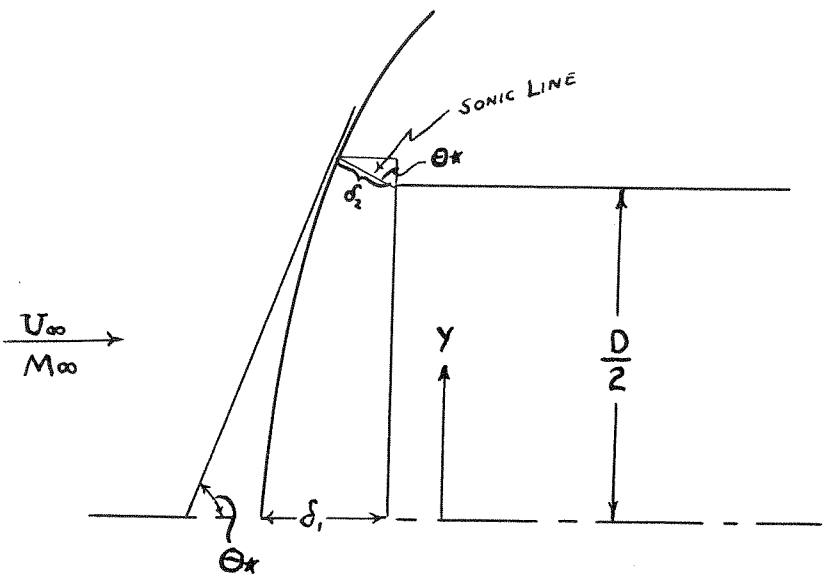

$$\rho_\infty U_\infty A_\infty = \rho_* U_* A_*$$

$$\frac{A_*}{A_\infty} = \frac{\rho_\infty}{\rho_*} \frac{U_\infty}{U_*}$$

$$\frac{A_*}{A_\infty} = \frac{\rho_\infty}{\rho_{\infty_t}} \frac{\rho_{\infty_t}}{\rho_{*_t}} \frac{\rho_{*_t}}{\rho_*} \frac{U_\infty}{M_* a_*} \qquad \text{WHERE } M_* = 1$$

$$\frac{A_*}{A_\infty} = \frac{\rho_\infty}{\rho_{\infty_t}} \frac{\rho_{\infty_t}}{\rho_{*_t}} \frac{\rho_{*_t}}{\rho_*} \frac{U_\infty}{a_*}$$

Using compressible flow tables to evaluate the right-hand side and assuming $M_\infty = 5.8$ so as to check results

$$\frac{A_*}{A_\infty} = \frac{(0.006023)(2.28552)}{(0.6339)(0.03412)} = 0.63646$$

Referring back to figure above it is apparent that

$$A_* = \delta_2 \pi (D + \delta_2 \cos \theta_*)$$

&

$$A_\infty = \pi \left(\frac{D}{2} + \delta_2 \cos \theta_*\right)^2$$

where θ_* is determined from the equation below and equals $66^\circ\ 25'$ for $M_\infty = 5.8$

$$\sin^2 \theta_* = \frac{1}{7 M_\infty^2}\left[3 M_\infty^2 - 2 + \sqrt{3(3 M_\infty^4 - 4 M_\infty^2 + 13)}\right]$$

FOR $\gamma = 1.40$

Therefore

$$\frac{\delta_2 D + \delta_2^2 \cos \theta_*}{\left(\frac{D}{2}\right)^2 + \delta_2 D \cos\theta_* + \delta_2^2 \cos^2 \theta_*} = 0.63646$$

Dividing through by D^2 and rearranging

$$0.25000 + \frac{\delta_2}{D}\cos\theta_* + \left(\frac{\delta_2}{D}\right)^2 \cos^2\theta_* = \frac{1}{0.63646}\left[\frac{\delta_2}{D} + \left(\frac{\delta_2}{D}\right)^2 \cos\theta_*\right]$$

or

$$0.46854\left(\frac{\delta_2}{D}\right)^2 + 1.17111\left(\frac{\delta_2}{D}\right) - 0.25000 = 0$$

$$\frac{\delta_2}{D} = \frac{-1.17111 + \sqrt{1.37150 + 0.46854}}{0.93708}$$

$$\frac{\delta_2}{D} = 0.1978$$

Measured value = 0.186

Difference = 0.0118

% error = $\frac{0.0118}{0.186}$ x 100 = 6.3%

Applying Hayes' theoretical shock shape which is $\delta^2 = \delta_1^2 - \frac{1}{2}ky^2$ (where it must be kept in mind that δ is measured normal to the body face)

At $y = \frac{D}{2} + \delta_2 \cos\theta_*$

$\delta = \delta_2 \sin\theta_*$

Therefore

$$\delta_1^2 = (\delta_2 \sin\theta_*)^2 + \frac{1}{2}\left(\frac{1}{5.224}\right)\left(\frac{D}{2} + \delta_2 \cos\theta_*\right)^2$$

or dividing through by D^2

$$\left(\frac{\delta_1}{D}\right)^2 = \left(\frac{\delta_2}{D}\right)^2 \sin^2\theta_* + (0.095712)\left[0.25000 + \frac{\delta_2}{D}\cos\theta_* + \left(\frac{\delta_2}{D}\right)^2 \cos^2\theta_*\right]$$

Using previous result that $\frac{\delta_2}{D} = 0.1978$,

$\left(\frac{\delta_1}{D}\right)^2 = 0.064973$

$\frac{\delta_1}{D} = 0.255$

Measured = 0.269

Difference = 0.014

% error = $\frac{0.014}{0.269}$ x 100 = 5.2%

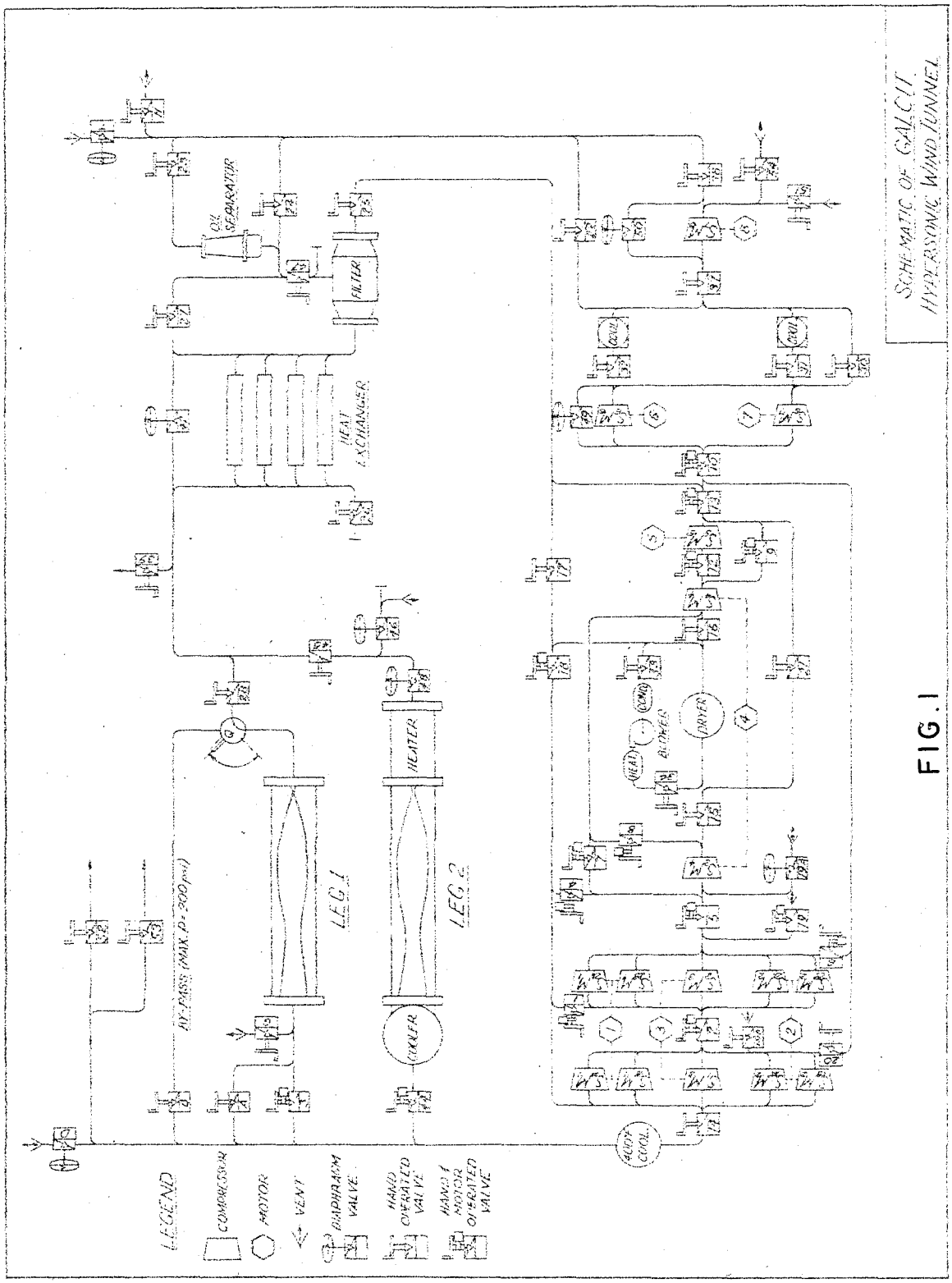
SCHEMATIC OF GALCIT
HYPERSONIC WIND TUNNEL
LEGEND
COMPRESSOR
MOTOR
VENT
DIAPHRAGM VALVE
HAND OPERATED VALVE
REMOTE MOTOR OPERATED VALVE
BY-PASS (MAX. P = 200 psia)
LEG 1
LEG 2
HEATER
COOLER
OIL SEPARATOR
FILTER
HEAT EXCHANGER
DRYER
AUX. COOL

FIG. 1

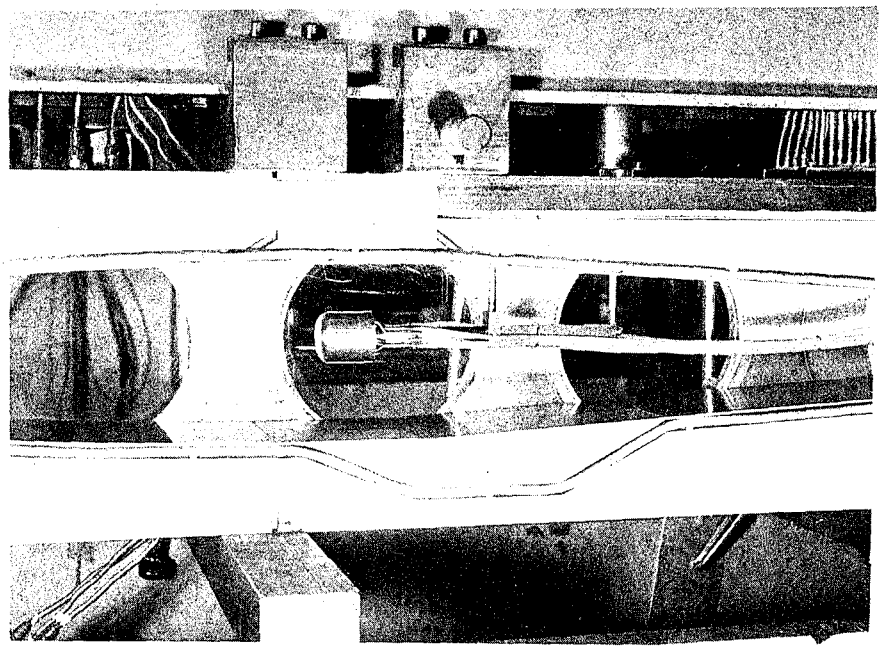

(A)

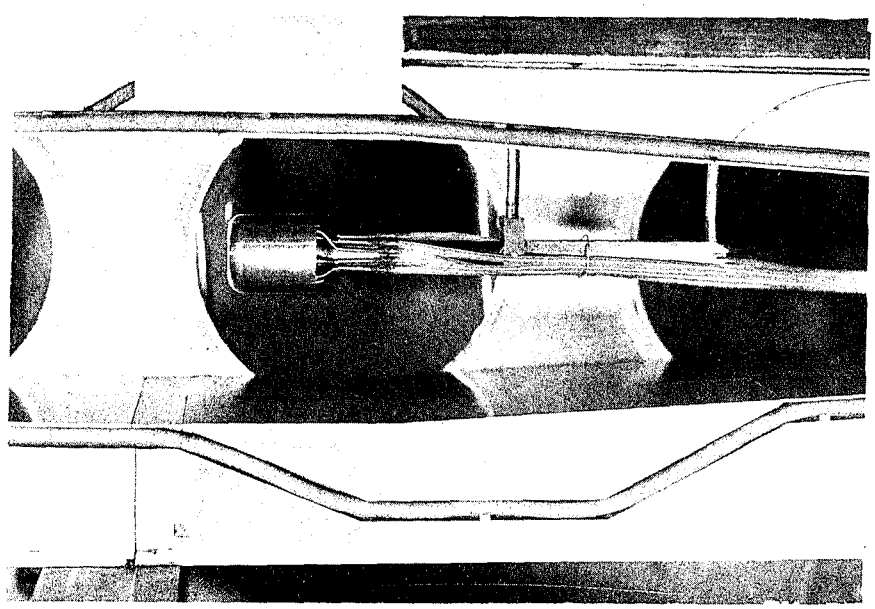

(B)

FIG. 2

TEST SECTION OF HYPERSONIC TUNNEL SHOWING METHOD OF MOUNTING MODELS

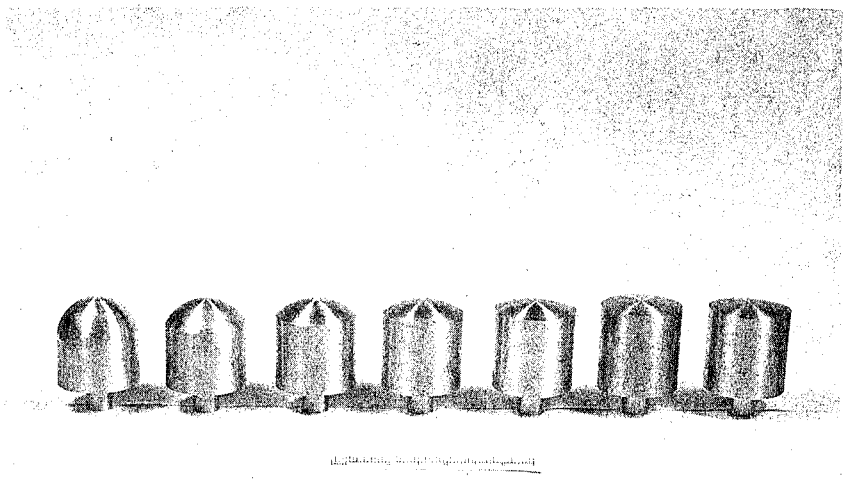

(A)

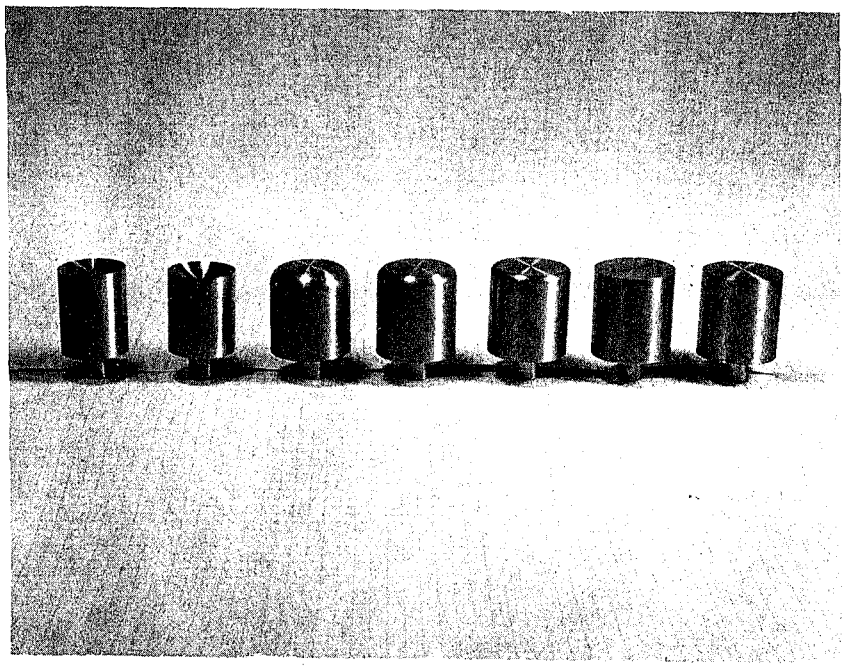

(B)

FIG. 3

PHOTOGRAPHS OF DUMMY MODELS USED IN SCHLIEREN STUDIES

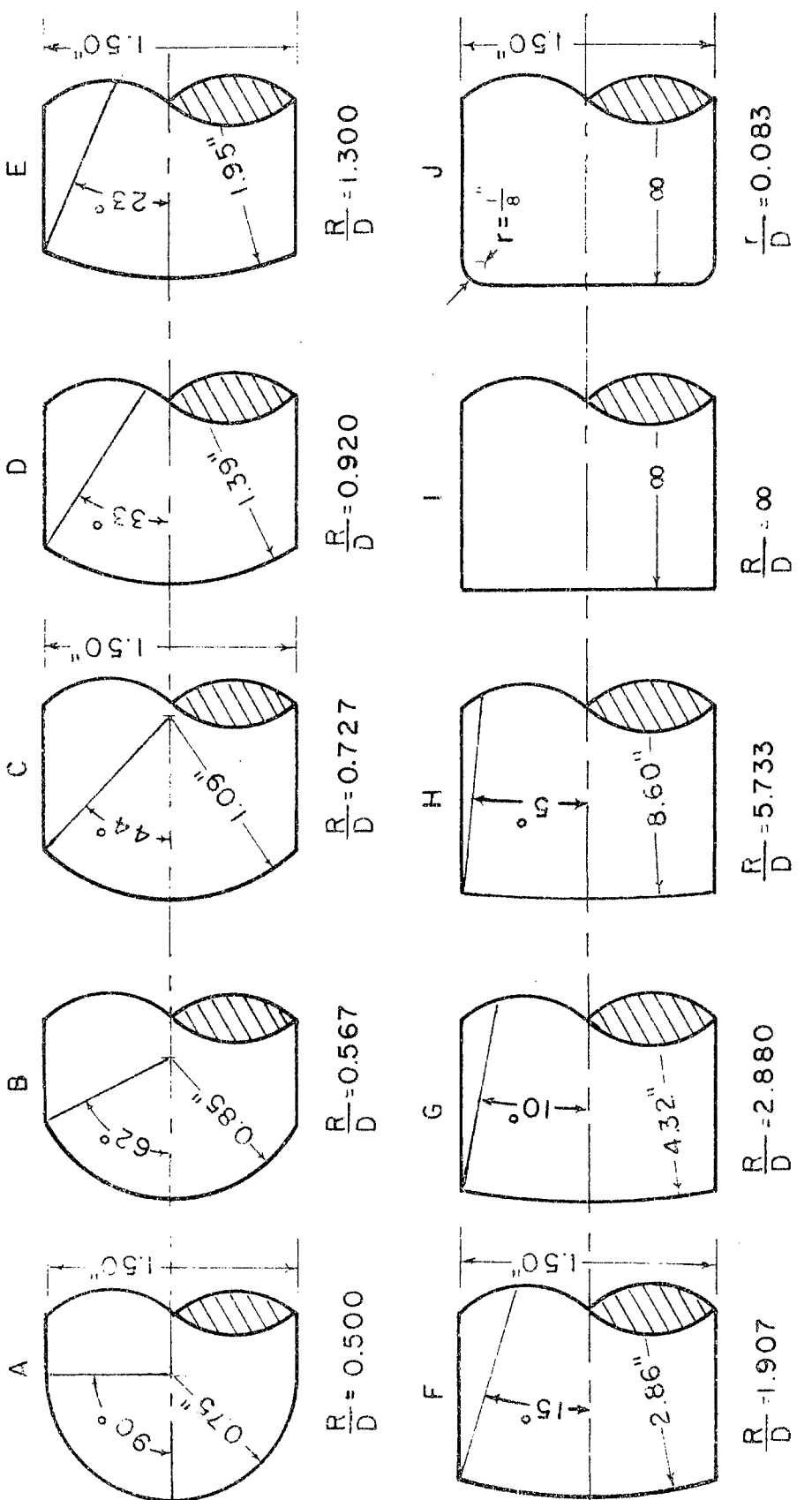

FIG. 4. NOSE CONFIGURATION OF DUMMY MODELS

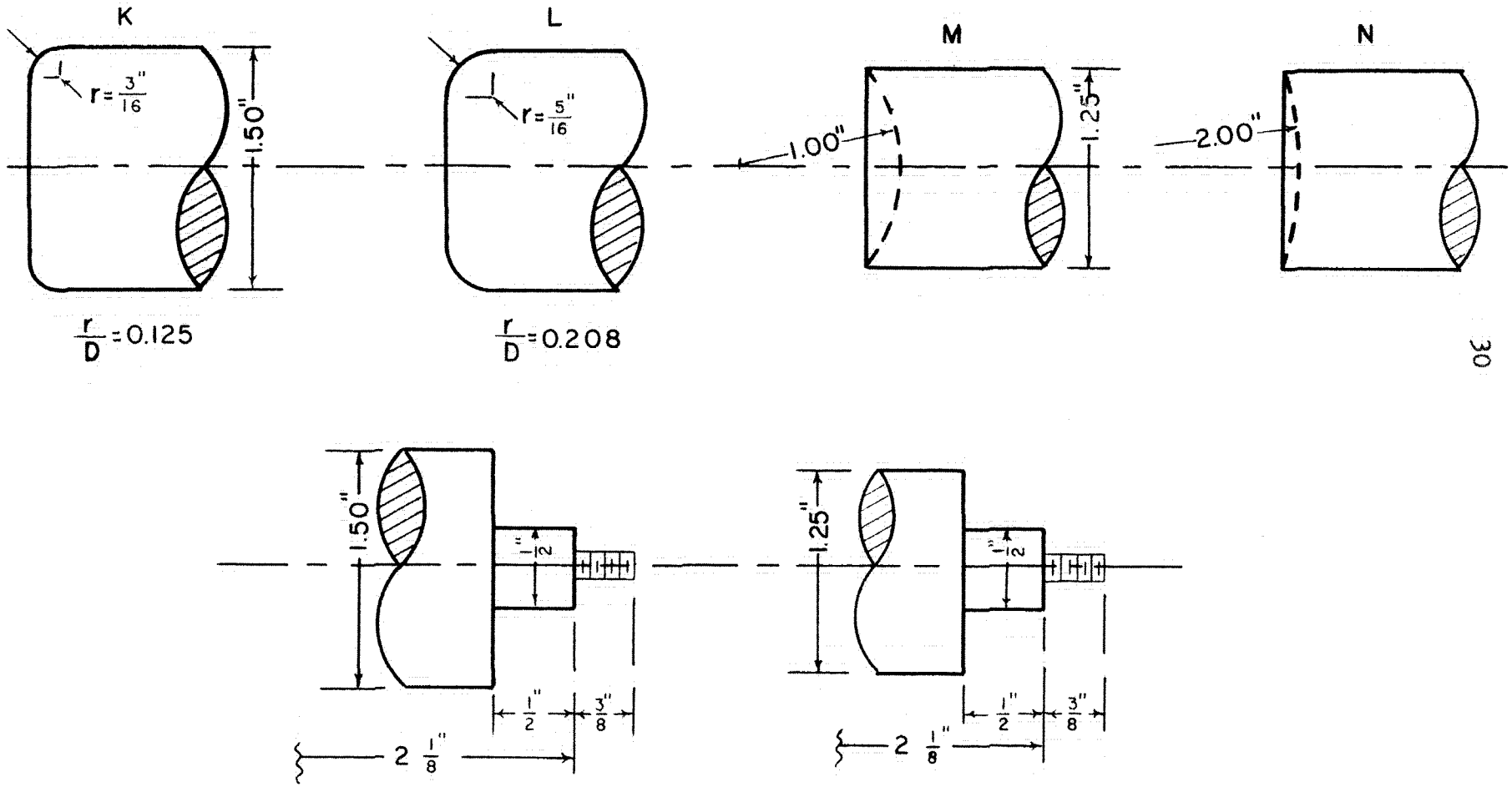

FIG. 5. NOSE AND AFTERBODY CONFIGURATION OF DUMMY MODELS

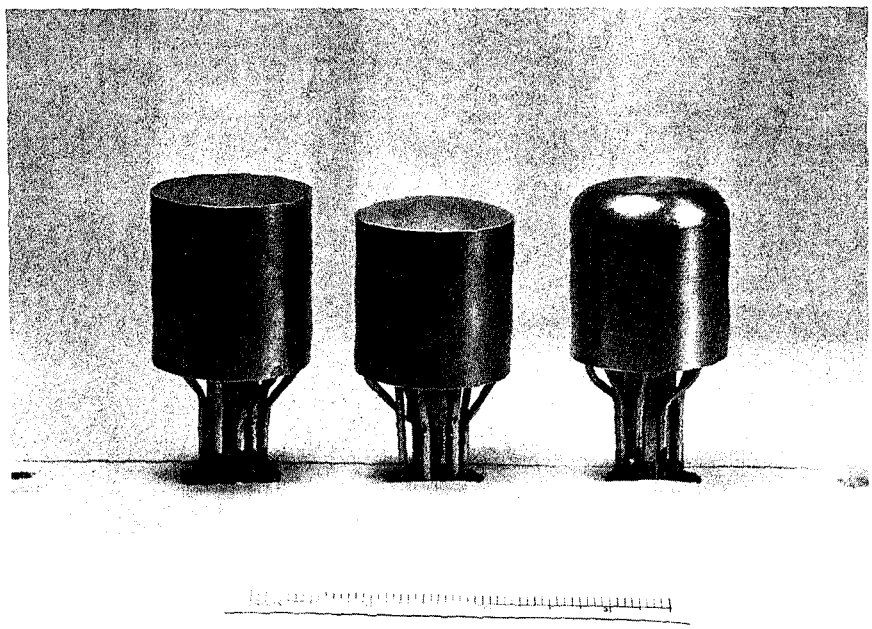

FIG. 6

PHOTOGRAPH OF STATIC PRESSURE MODELS

Orifice	S(in)
1	0.000
2	0.100
3	0.200
4	0.350
5	0.500
6	0.650
7	0.700
8	0.800
9	0.850

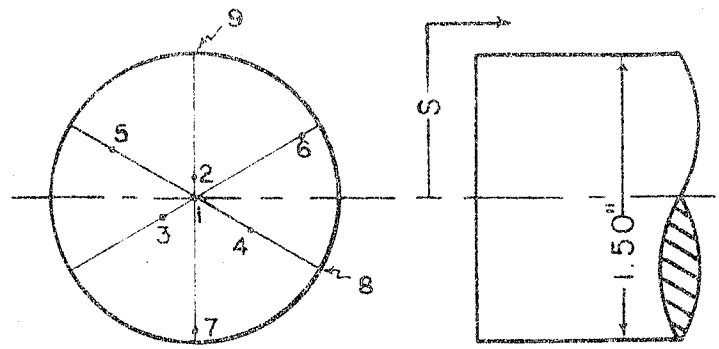

(A) FLAT NOSE MODEL

Orifice	S(in)
1	0.000
2	0.100
3	0.200
4	0.350
5	0.510
6	0.665
7	0.720
8	0.820
9	0.870

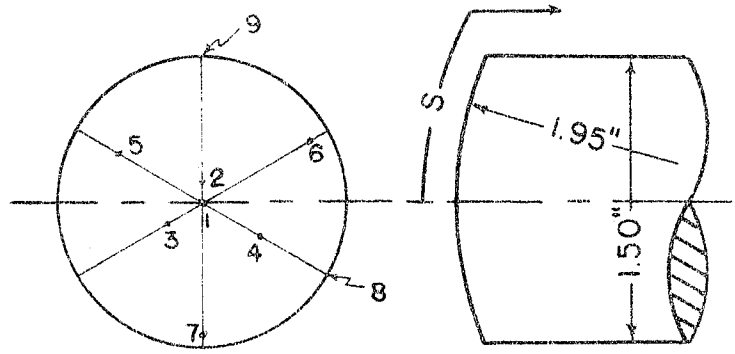

(B) 1.95" NOSE RADIUS MODEL

Orifice	S(in)
1	0.000
2	0.100
3	0.200
4	0.350
5	0.485
6	0.500
7	0.580
8	0.671
9	0.92
10	1.02

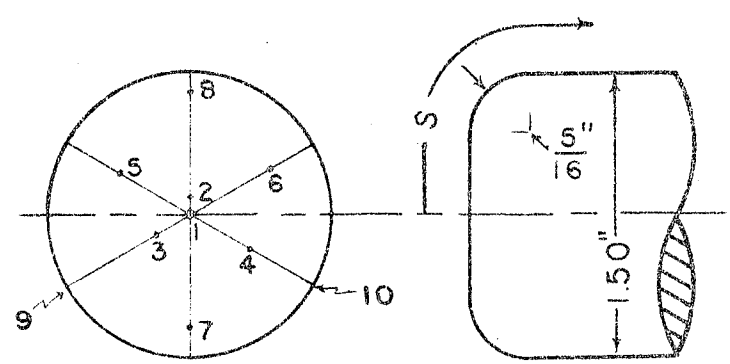

(C) $\frac{5}{16}$" ROUNDED SHOULDER MODEL

FIG 7. PRESSURE MODEL ORIFICE LOCATION

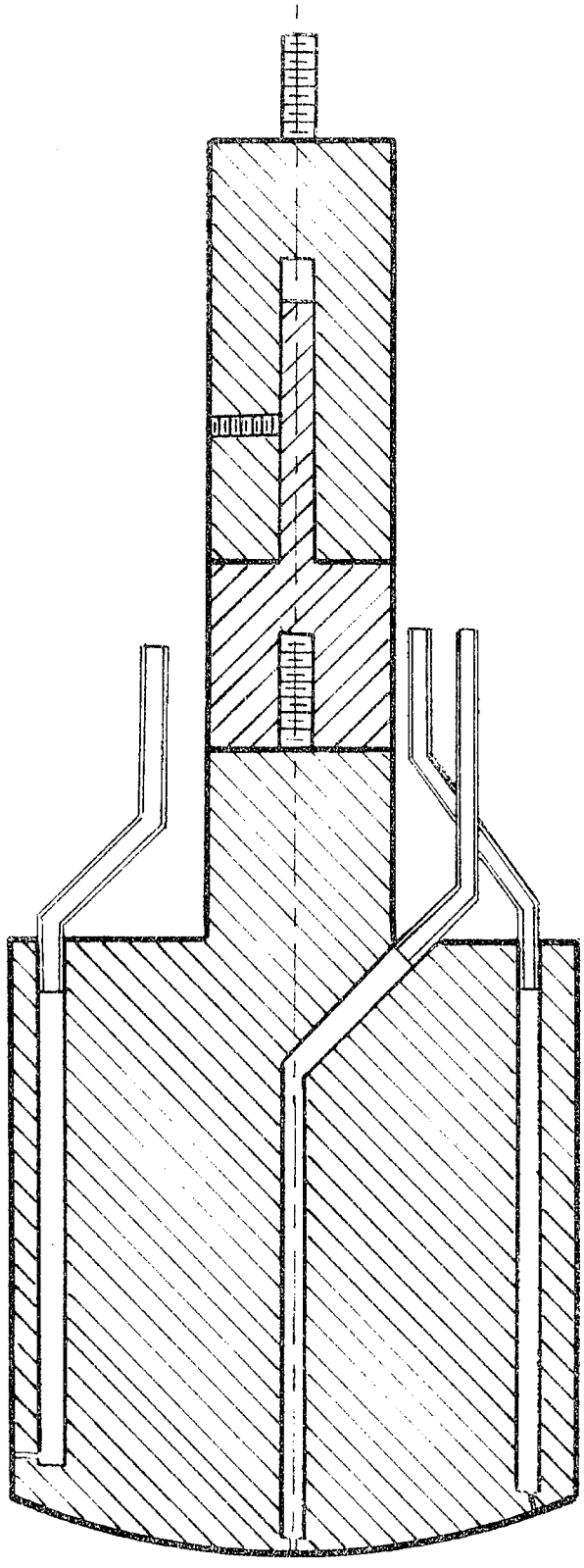

FIG. 6. CUTAWAY VIEW OF TYPICAL PRESSURE MODEL

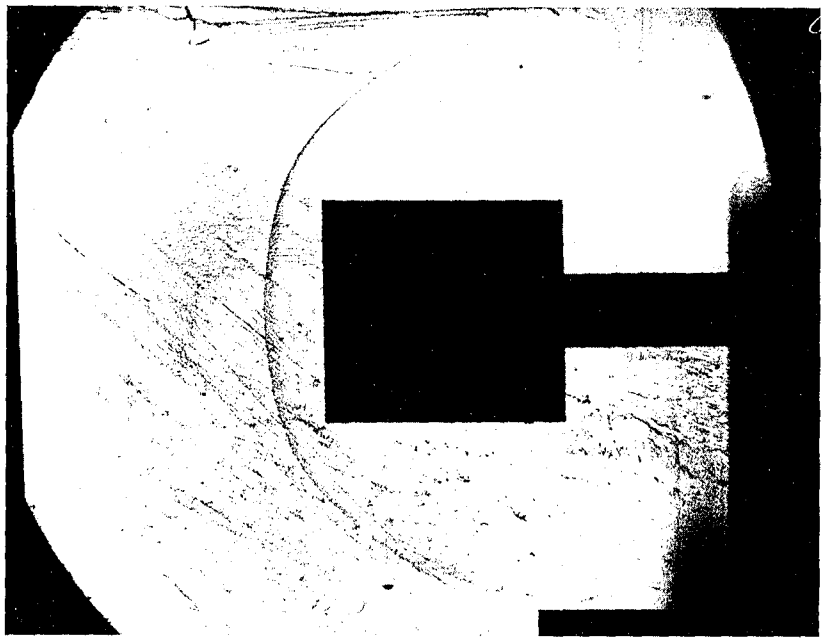

FIG. 9

SCHLIEREN PHOTOGRAPH OF FLAT FACED BLUNT BODY (R/D = ∞) AT ZERO DEGREES ANGLE OF YAW, M = 5.8.

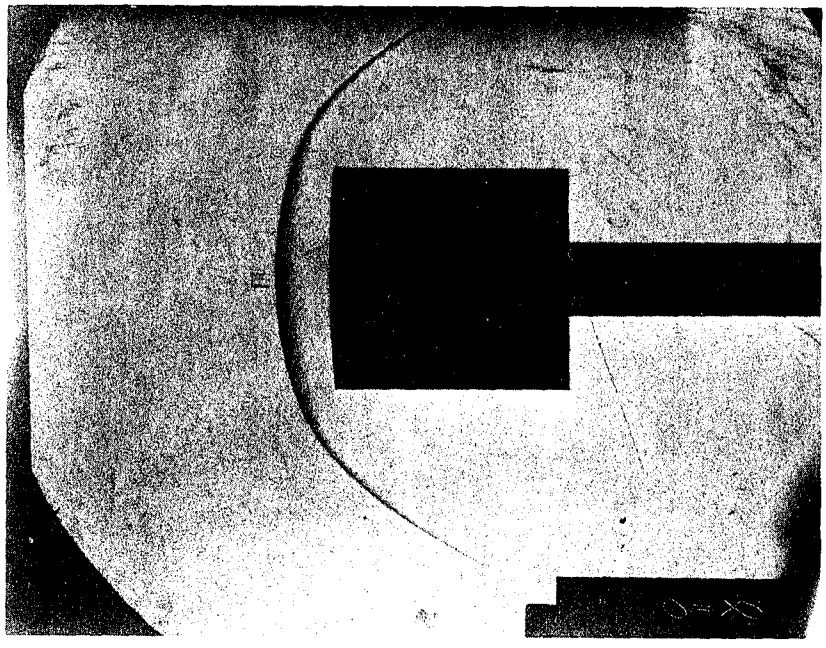

FIG. 10

SCHLIEREN PHOTOGRAPH OF ROUND NOSED BLUNT BODY (R/D = 5.733) AT ZERO DEGREES ANGLE OF YAW, M = 5.8.

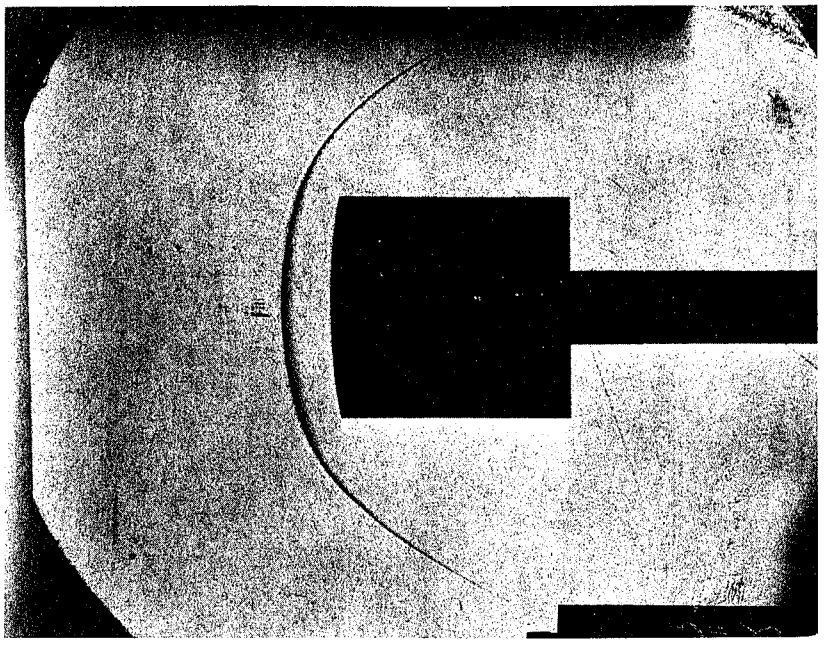

FIG. 11

SCHLIEREN PHOTOGRAPH OF ROUND NOSED BLUNT BODY (R/D = 2.880) AT ZERO DEGREES ANGLE OF YAW, M = 5.8.

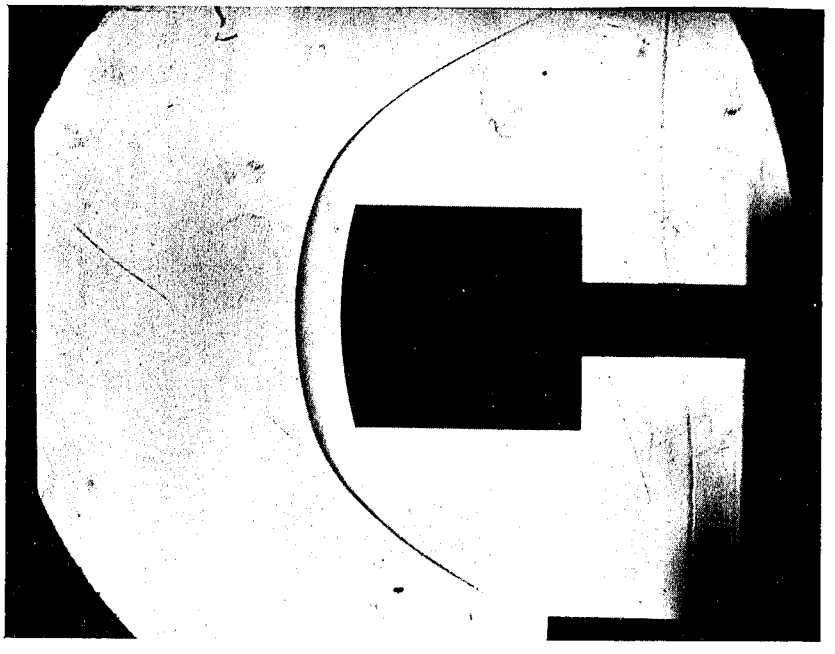

FIG. 12

SCHLIEREN PHOTOGRAPH OF ROUND NOSED BLUNT BODY (R/D = 1.907) AT ZERO DEGREES ANGLE OF YAW, M = 5.8.

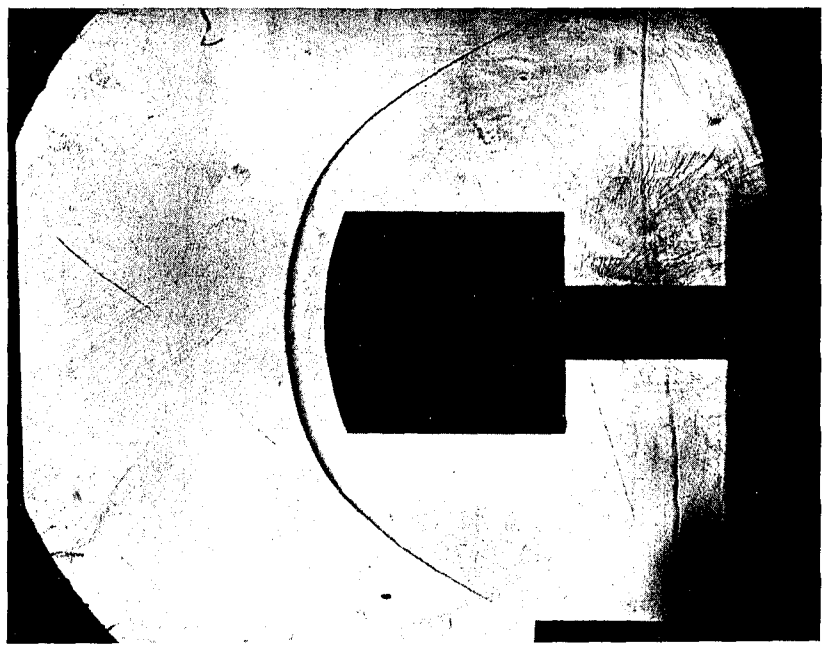

FIG. 13

SCHLIEREN PHOTOGRAPH OF ROUND NOSED BLUNT BODY (R/D = 1.300) AT ZERO DEGREES ANGLE OF YAW, M = 5.8.

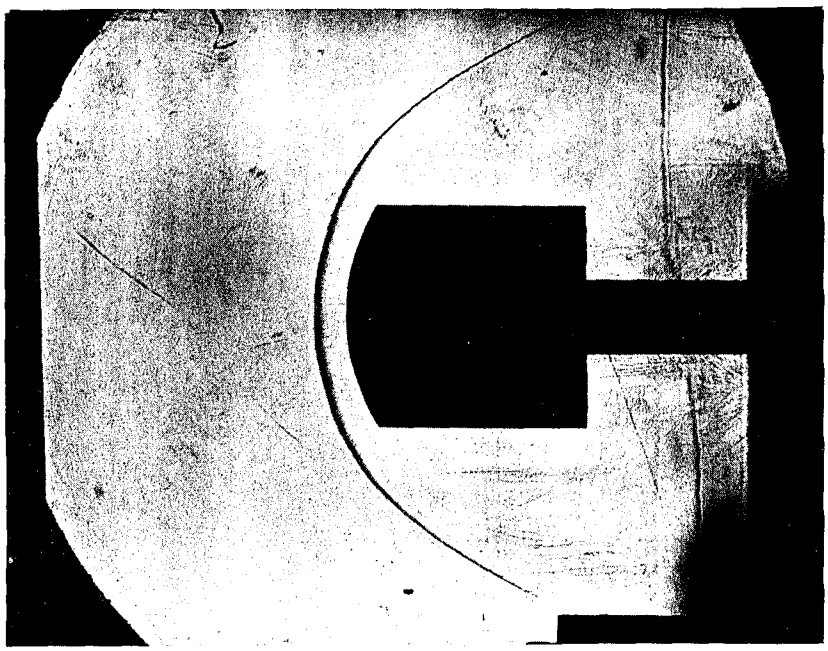

FIG. 14

SCHLIEREN PHOTOGRAPH OF ROUND NOSED BLUNT BODY (R/D = 0.920) AT ZERO DEGREES ANGLE OF YAW, M = 5.8.

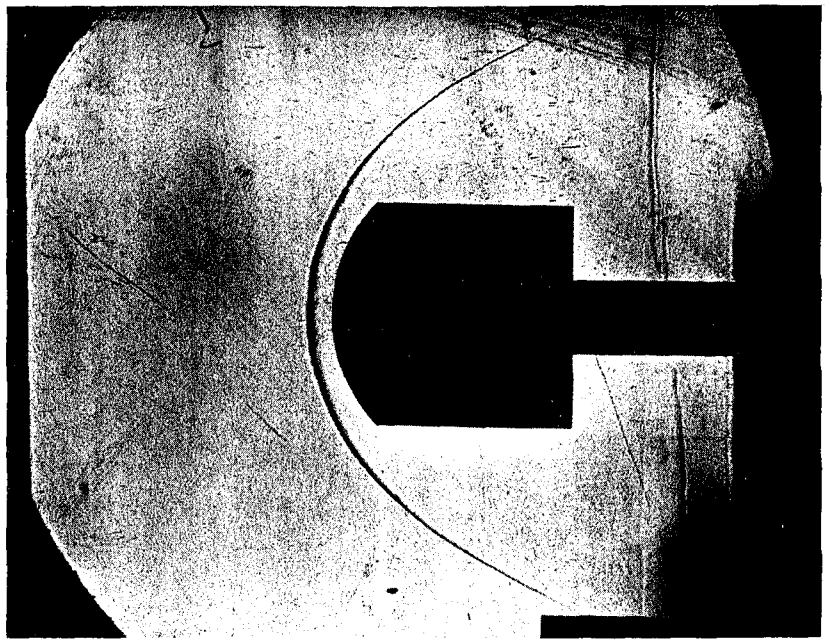

FIG. 15

SCHLIEREN PHOTOGRAPH OF ROUND NOSED BLUNT BODY (R/D = 0.727) AT ZERO DEGREES ANGLE OF YAW, M = 5.8.

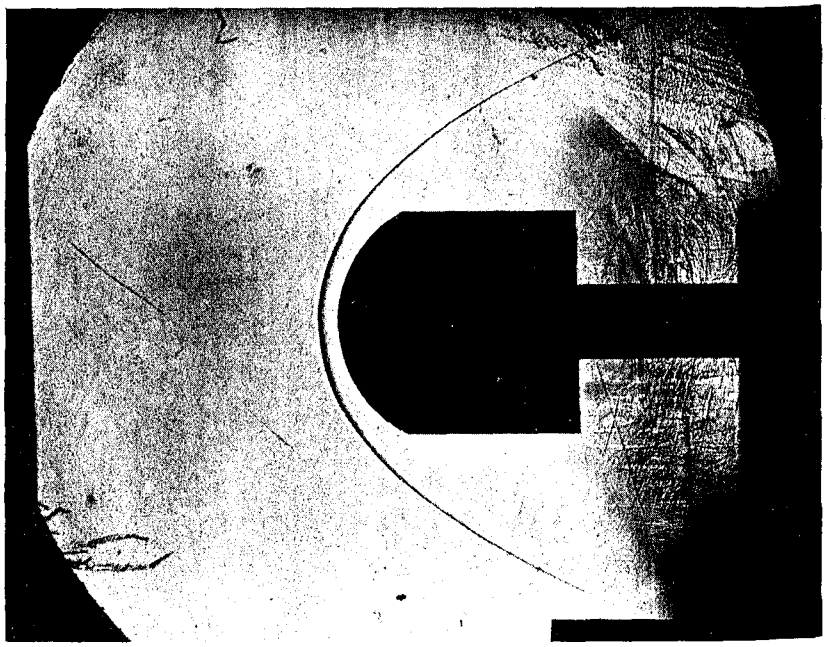

FIG. 16

SCHLIEREN PHOTOGRAPH OF ROUND NOSED BLUNT BODY (R/D = 0.567) AT ZERO DEGREES ANGLE OF YAW, M = 5.8.

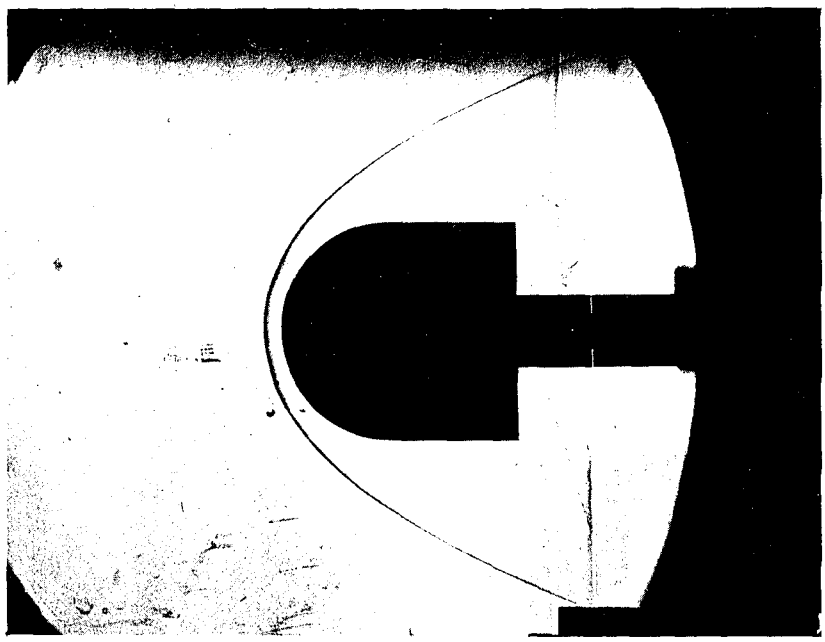

FIG. 17

SCHLIEREN PHOTOGRAPH OF ROUND NOSED BLUNT BODY (R/D = 0.500) (HEMISPHERE) AT ZERO DEGREES ANGLE OF YAW, M = 5.8.

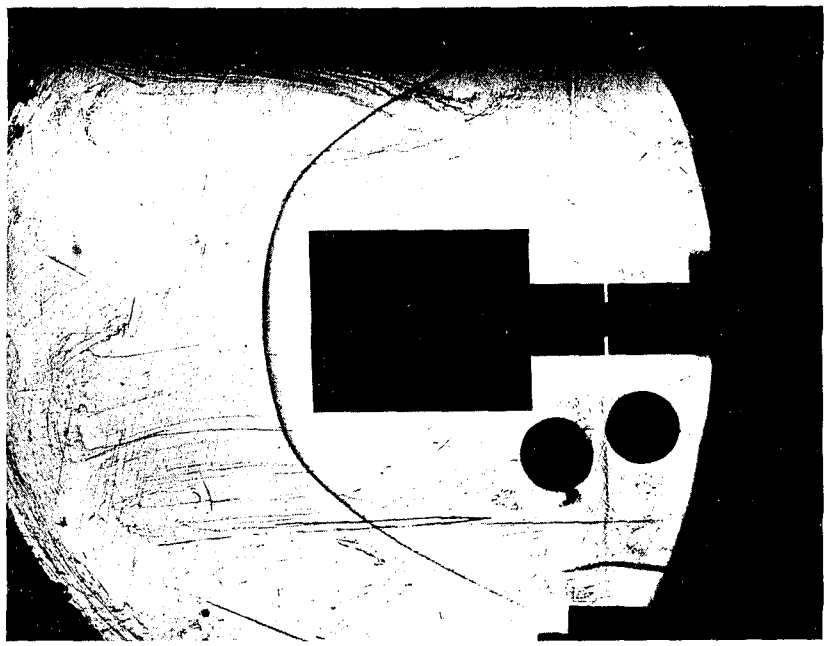

FIG. 18

SCHLIEREN PHOTOGRAPH OF CONCAVE NOSED BLUNT BODY (R/D = 0.800) AT ZERO DEGREES ANGLE OF YAW, M = 5.8.

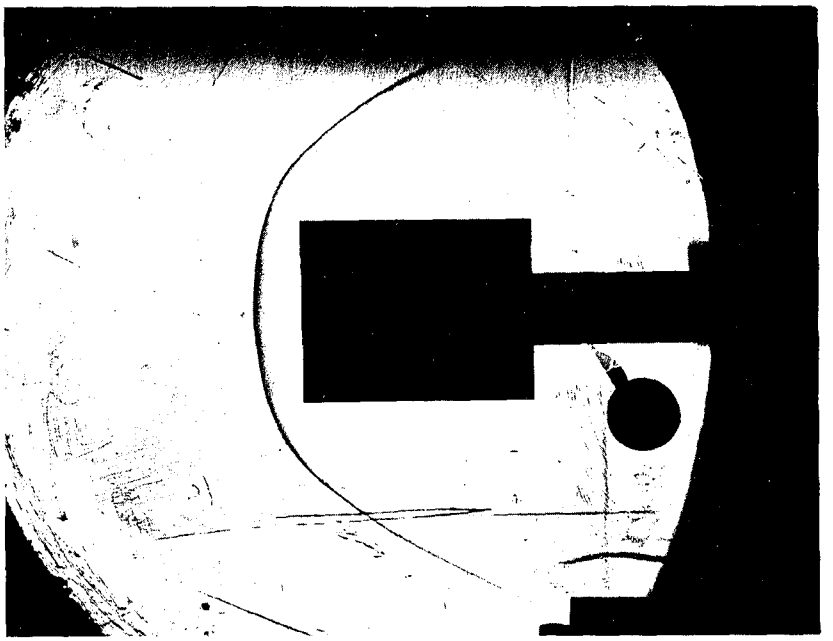

FIG. 19

SCHLIEREN PHOTOGRAPH OF CONCAVE NOSED BLUNT BODY (R/D = 1.600) AT 0 DEGREES ANGLE OF YAW, M = 5.8.

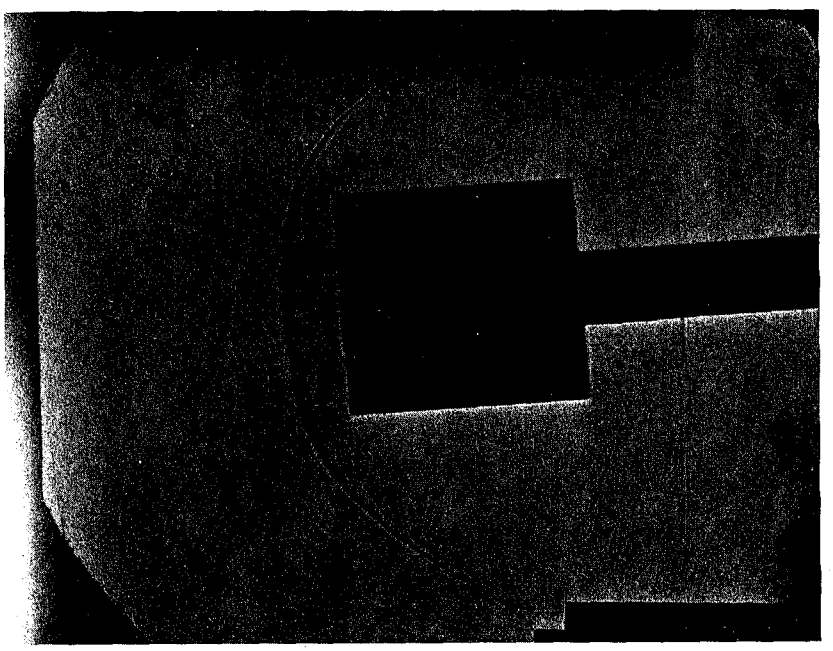

FIG. 20

SCHLIEREN PHOTOGRAPH OF FLAT FACED BLUNT BODY (R/D = ∞) AT 4 DEGREES ANGLE OF YAW, M = 5.8.

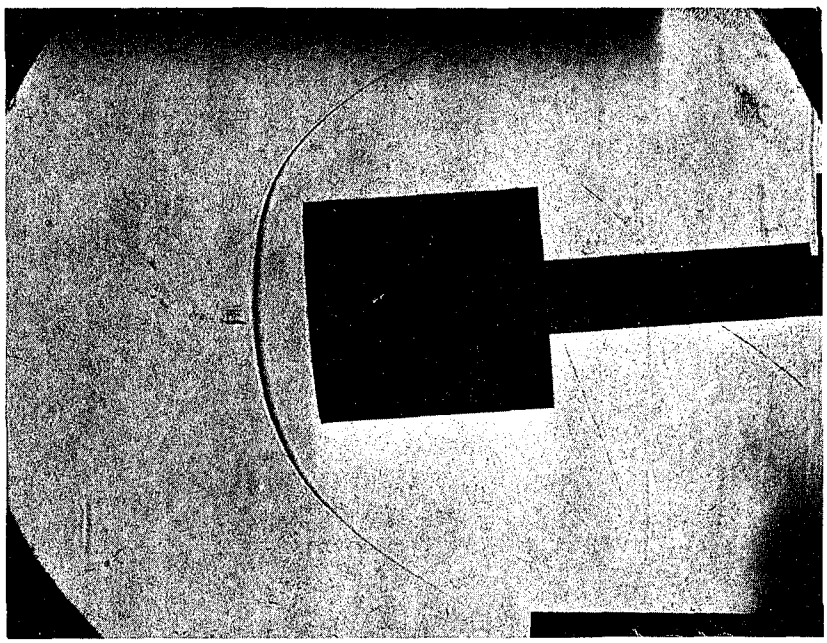

FIG. 21

SCHLIEREN PHOTOGRAPH OF ROUND NOSED BLUNT BODY (R/D = 5.733) AT 4 DEGREES ANGLE OF YAW, M = 5.8.

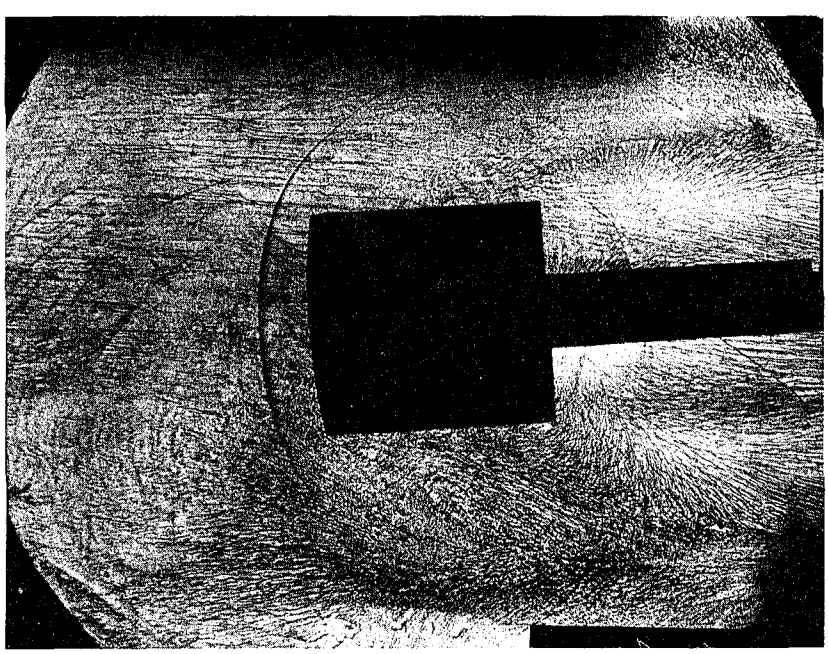

FIG. 22

SCHLIEREN PHOTOGRAPH OF ROUND NOSED BLUNT BODY (R/D = 2.880) AT 4 DEGREES ANGLE OF YAW, M = 5.8.

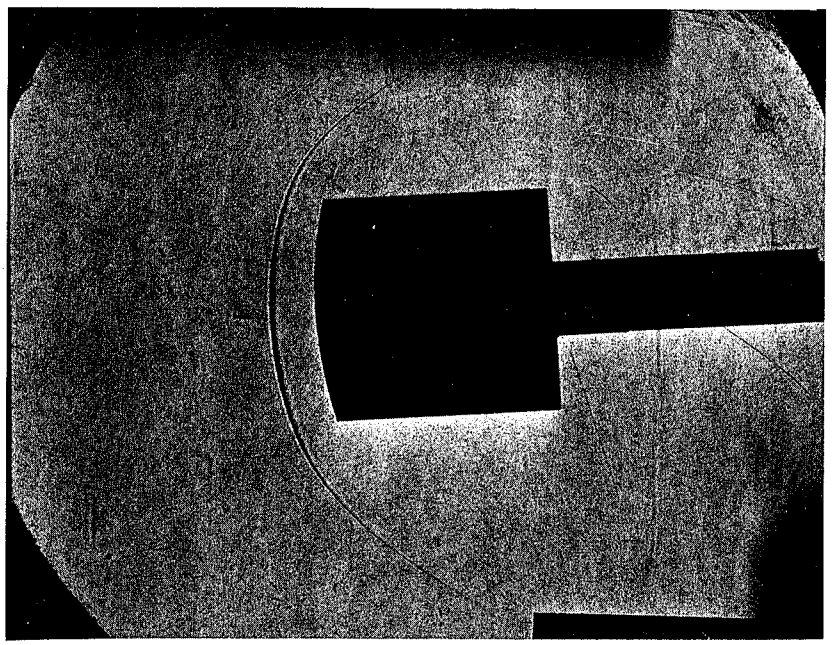

FIG. 23

SCHLIEREN PHOTOGRAPH OF ROUND NOSED BLUNT BODY (R/D = 1.907) AT 4 DEGREES ANGLE OF YAW, M = 5.8.

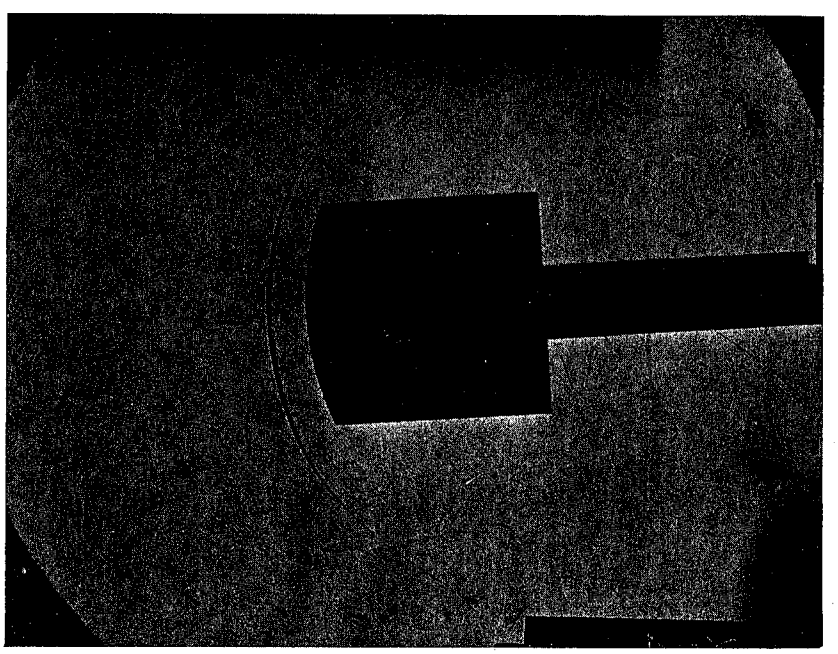

FIG. 24

SCHLIEREN PHOTOGRAPH OF ROUND NOSED BLUNT BODY (R/D = 1.300) AT 4 DEGREES ANGLE OF YAW, M = 5.8.

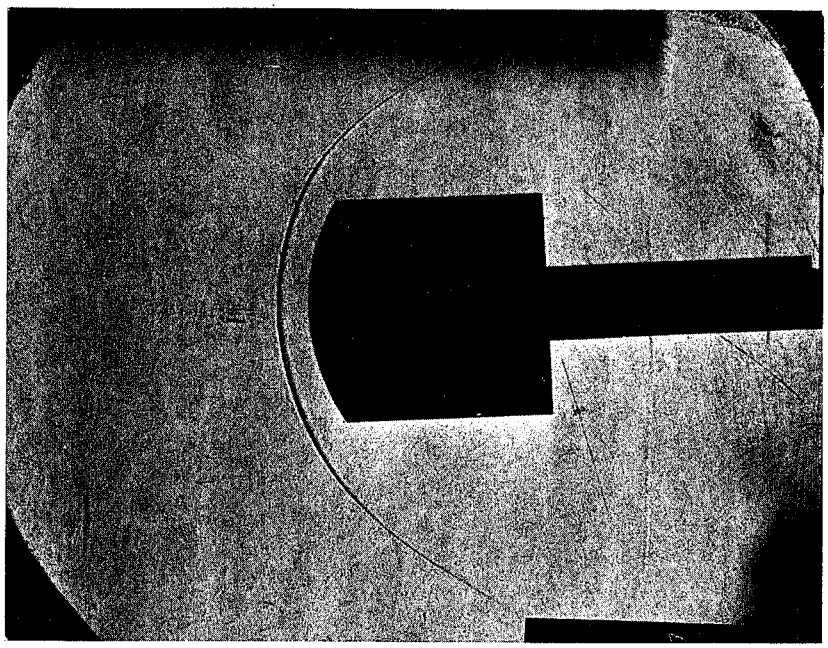

FIG. 25

SCHLIEREN PHOTOGRAPH OF ROUND NOSED BLUNT BODY (R/D = 0.920) AT 4 DEGREES ANGLE OF YAW, M = 5.8.

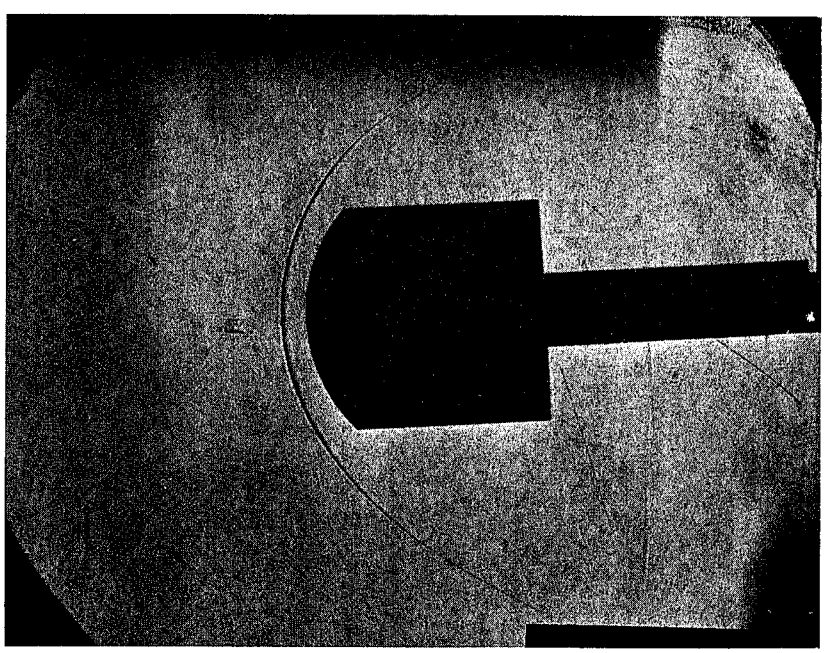

FIG. 26

SCHLIEREN PHOTOGRAPH OF ROUND NOSED BLUNT BODY (R/D = 0.727) AT 4 DEGREES ANGLE OF YAW, M = 5.8.

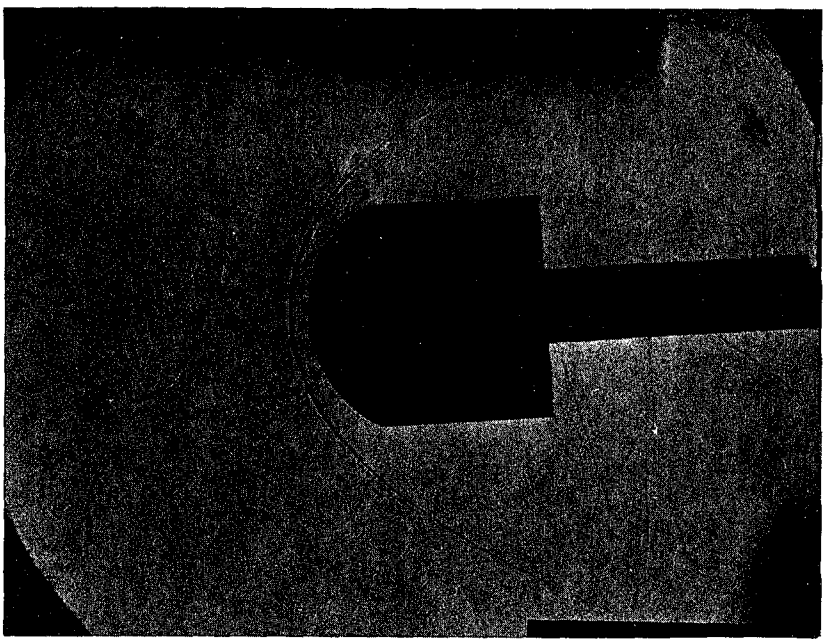

FIG. 27

SCHLIEREN PHOTOGRAPH OF ROUND NOSED BLUNT BODY (R/D = 0.567) AT 4 DEGREES ANGLE OF YAW, M = 5.8.

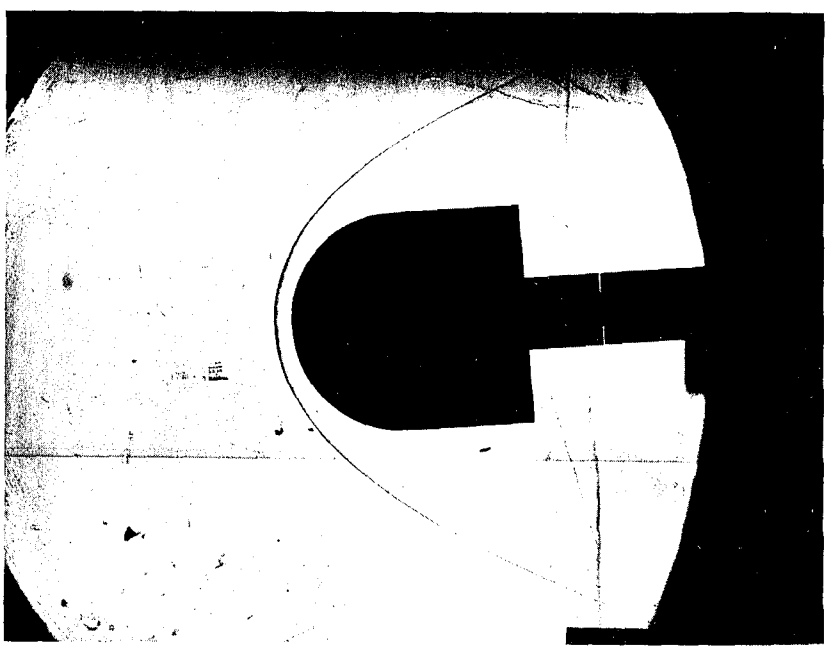

FIG. 28

SCHLIEREN PHOTOGRAPH OF ROUND NOSED BLUNT BODY (R/D = 0.500) (HEMISPHERE) AT 4 DEGREES ANGLE OF YA M = 5.8.

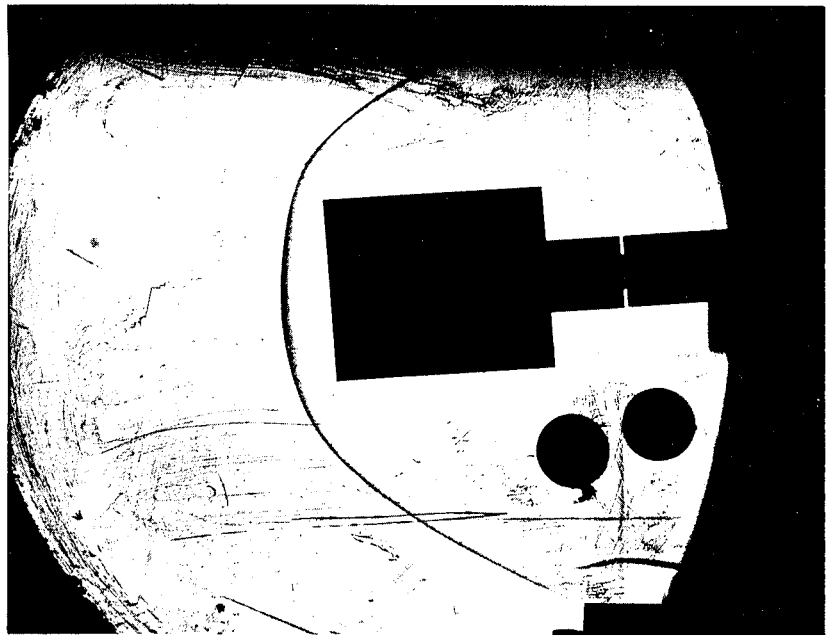

FIG. 29

SCHLIEREN PHOTOGRAPH OF CONCAVE NOSED BLUNT BODY (R/D = 0.800) AT 4 DEGREES ANGLE OF YAW, M = 5.8.

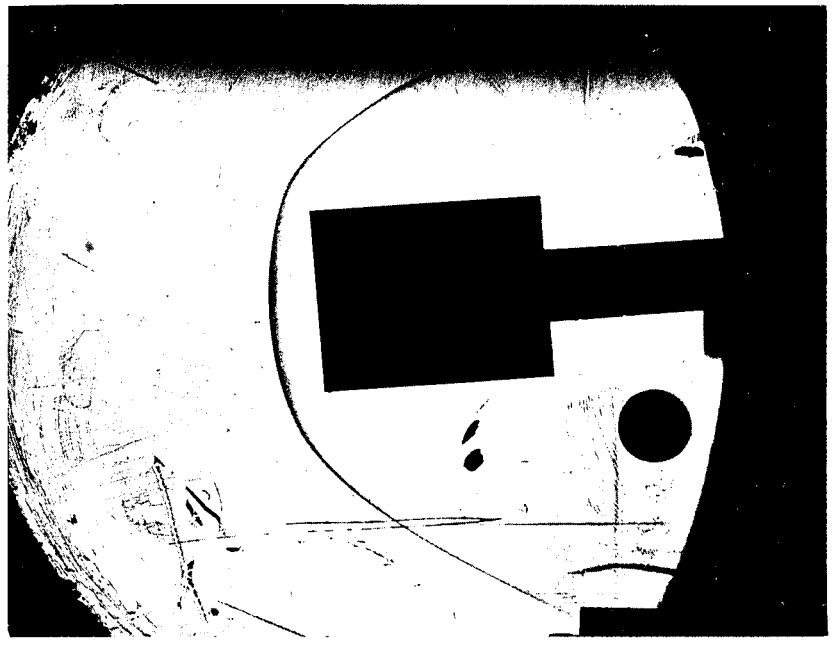

FIG. 30

SCHLIEREN PHOTOGRAPH OF CONCAVE NOSED BLUNT BODY (R/D = 1.600) AT 4 DEGREES ANGLE OF YAW, M = 5.8.

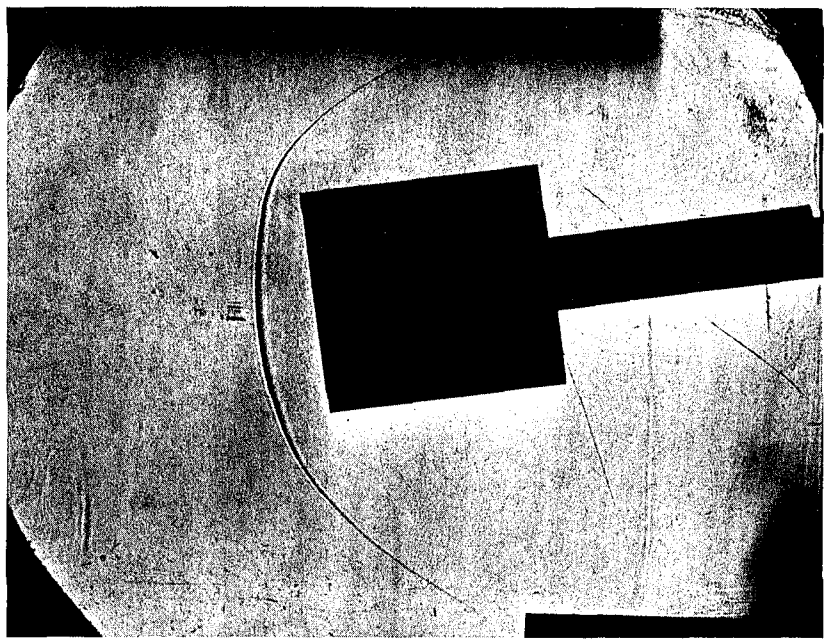

FIG. 31

SCHLIEREN PHOTOGRAPH OF FLAT FACED BLUNT BODY ($R/D = \infty$) AT 8 DEGREES ANGLE OF YAW, $M = 5.8$.

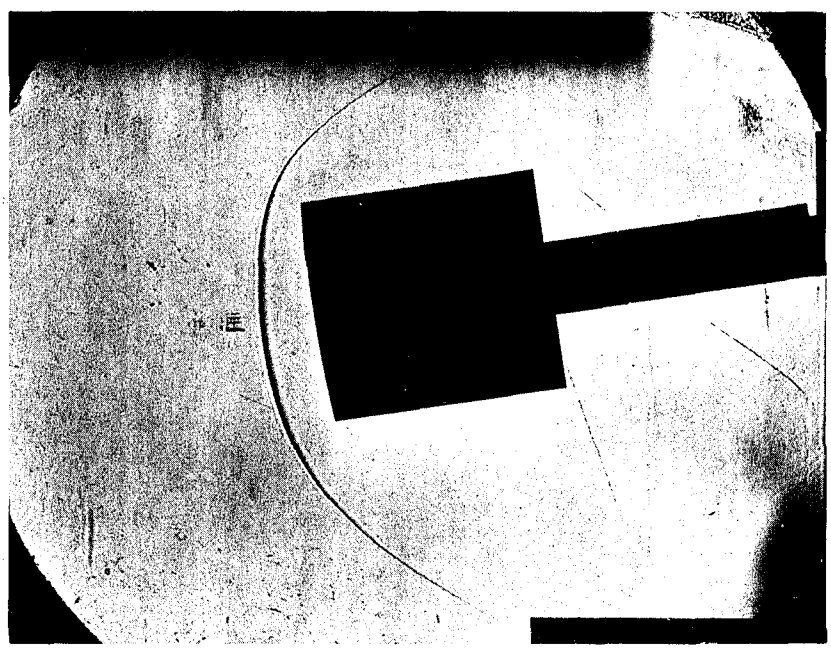

FIG. 32

SCHLIEREN PHOTOGRAPH OF ROUND NOSED BLUNT BODY ($R/D = 5.733$) AT 8 DEGREES ANGLE OF YAW, $M = 5.8$.

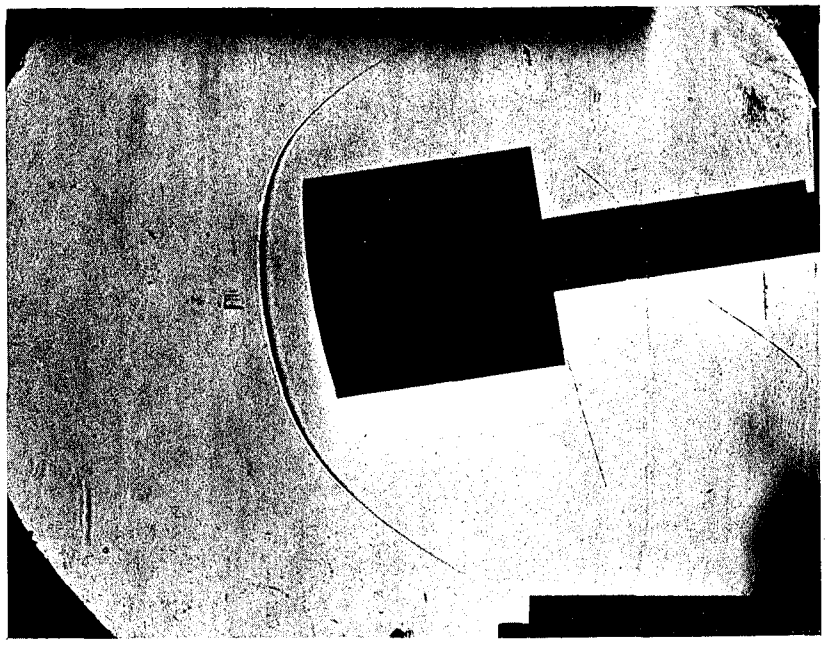

FIG. 33

SCHLIEREN PHOTOGRAPH OF ROUND NOSED BLUNT BODY (R/D = 2.880) AT 8 DEGREES ANGLE OF YAW, M = 5.8.

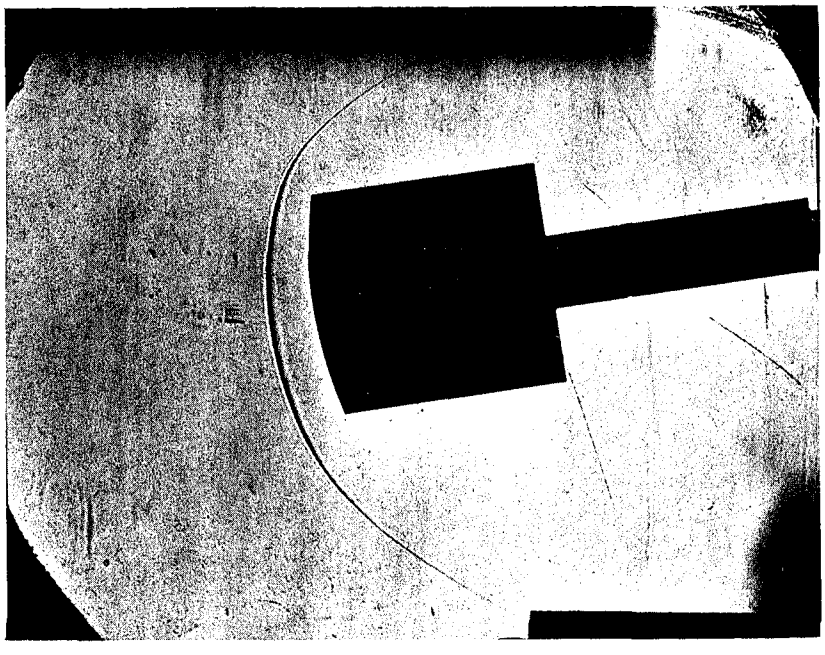

FIG. 34

SCHLIEREN PHOTOGRAPH OF ROUND NOSED BLUNT BODY (R/D = 1.907) AT 8 DEGREES ANGLE OF YAW, M = 5.8.

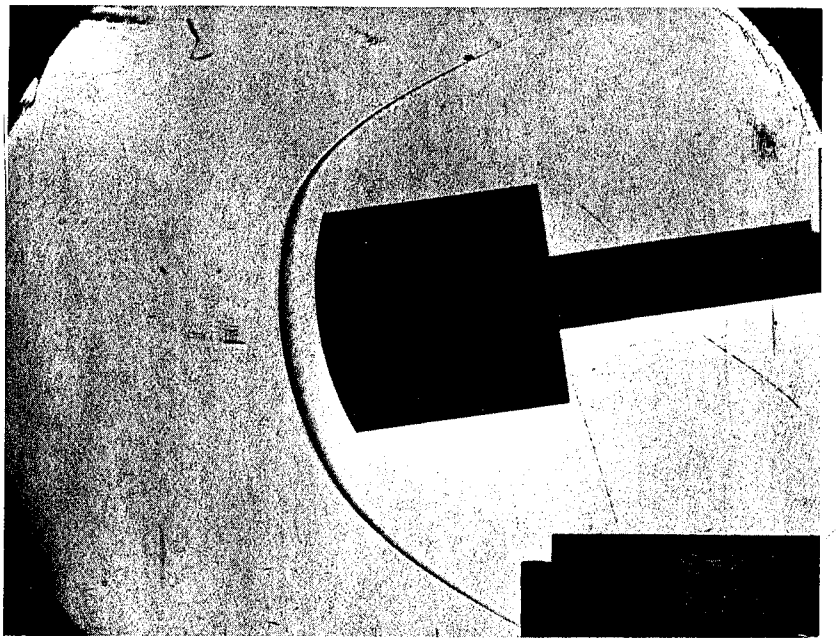

FIG. 35

SCHLIEREN PHOTOGRAPH OF ROUND NOSED BLUNT BODY (R/D = 1.300) AT 8 DEGREES ANGLE OF YAW, M = 5.8.

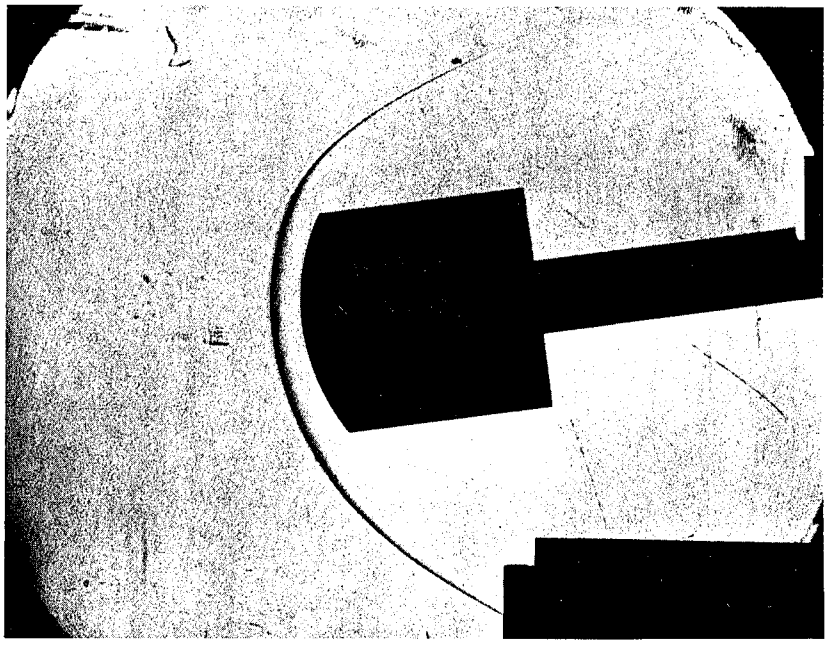

FIG. 36

SCHLIEREN PHOTOGRAPH OF ROUND NOSED BLUNT BODY (R/D = 0.920) AT 8 DEGREES ANGLE OF YAW, M = 5.8.

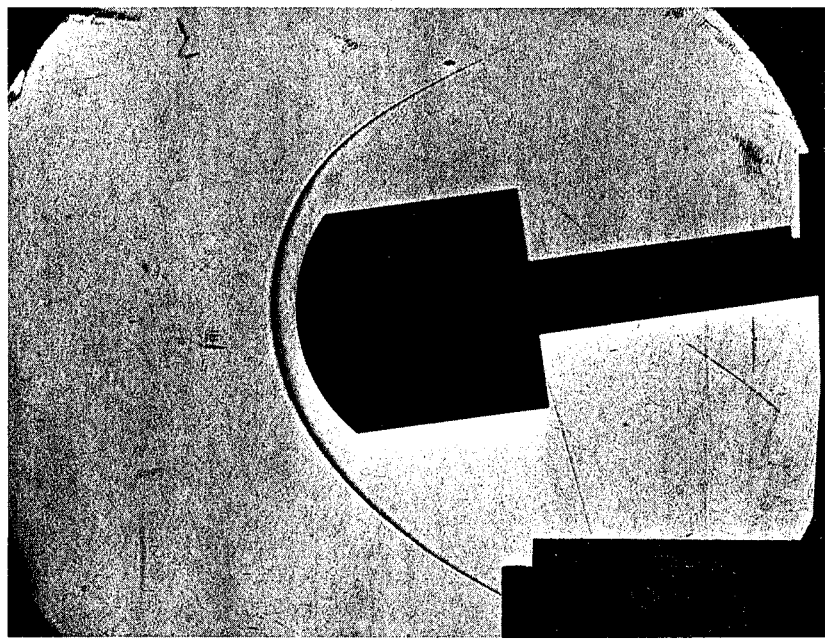

FIG. 37

SCHLIEREN PHOTOGRAPH OF ROUND NOSED BLUNT BODY (R/D = 0.727) AT 8 DEGREES ANGLE OF YAW, M = 5.8.

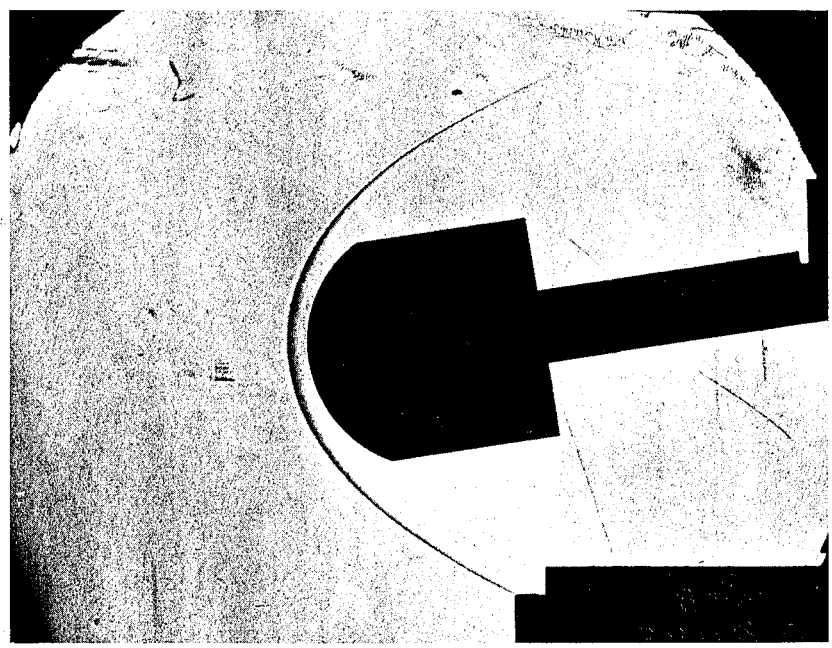

FIG. 38

SCHLIEREN PHOTOGRAPH OF ROUND NOSED BLUNT BODY (R/D = 0.567) AT 8 DEGREES ANGLE OF YAW, M = 5.8.

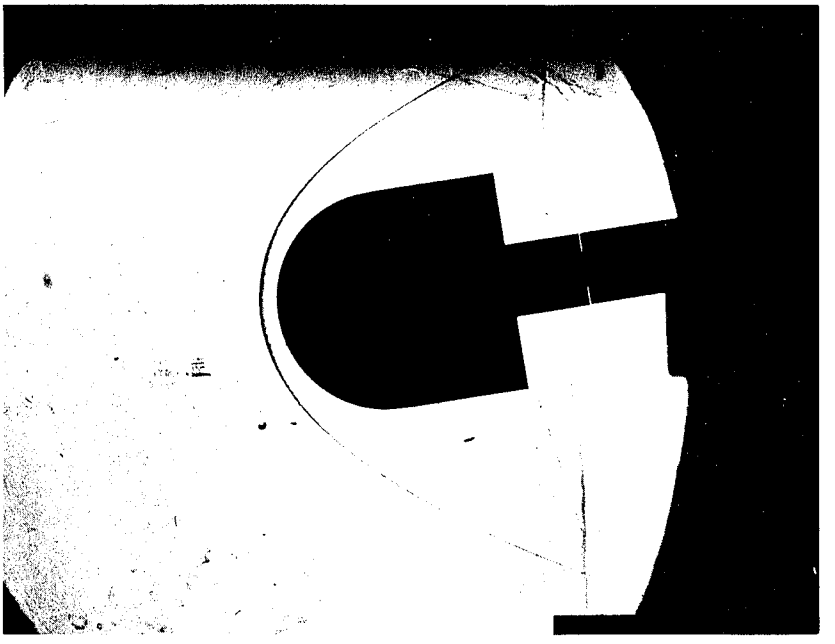

FIG. 39

SCHLIEREN PHOTOGRAPH OF ROUND NOSED BLUNT BODY (R/D = 0.500) (HEMISPHERE) AT 8 DEGREES ANGLE OF YAW M = 5.8.

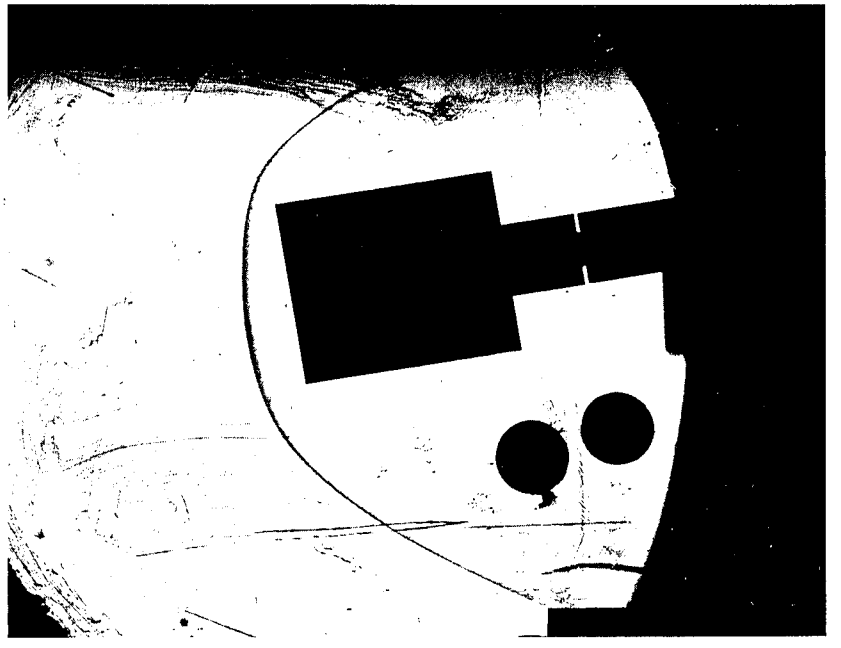

FIG. 40

SCHLIEREN PHOTOGRAPH OF CONCAVE NOSED BLUNT BODY (R/D = 0.800) AT 8 DEGREES ANGLE OF YAW, M = 5.8.

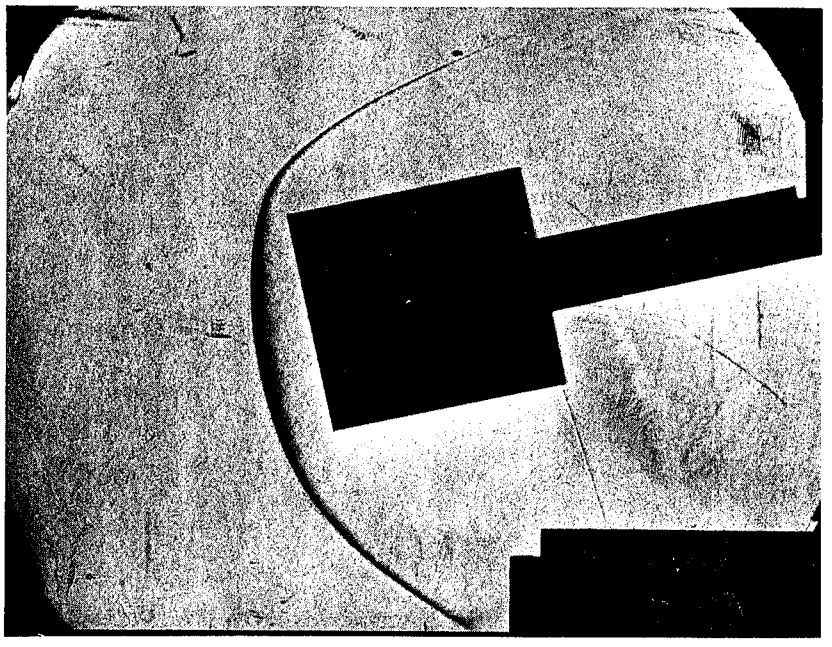

FIG. 41

SCHLIEREN PHOTOGRAPH OF FLAT FACED BLUNT BODY (R/D = ∞) AT 12 DEGREES ANGLE OF YAW, M = 5.8.

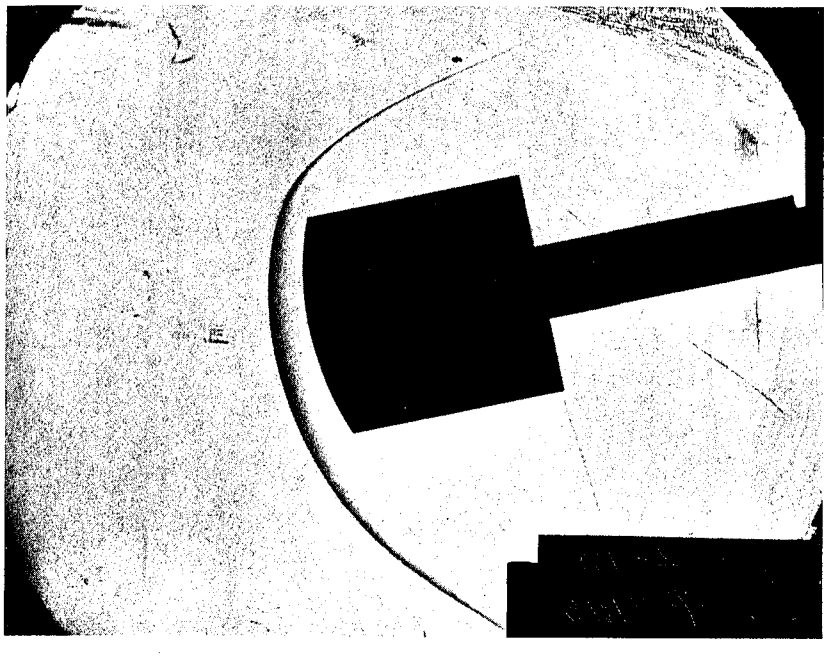

FIG. 42

SCHLIEREN PHOTOGRAPH OF ROUND NOSED BLUNT BODY (R/D) = 1.300 AT 12 DEGREES ANGLE OF YAW, M = 5.8.

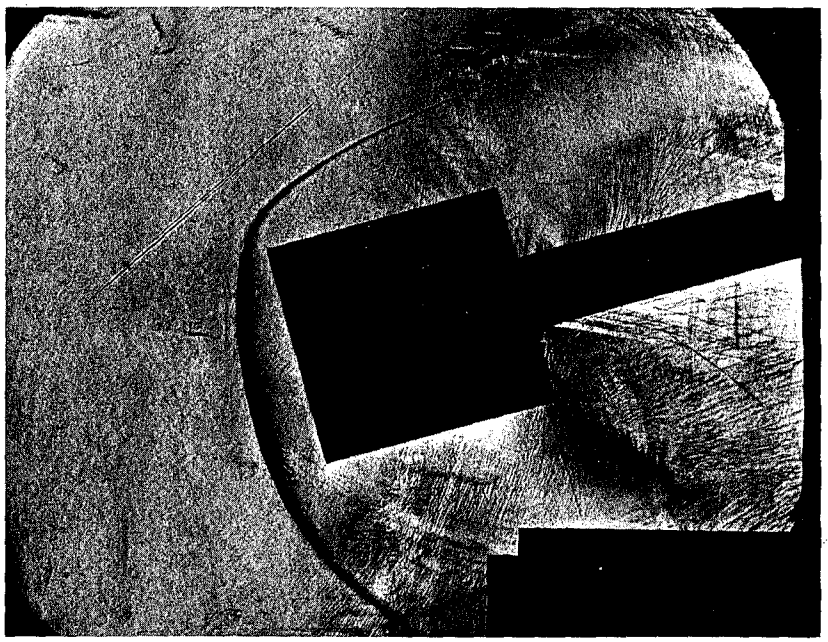

FIG. 43

SCHLIEREN PHOTOGRAPH OF FLAT FACED BLUNT BODY (R/D = ∞) AT 16 DEGREES ANGLE OF YAW, M = 5.8.

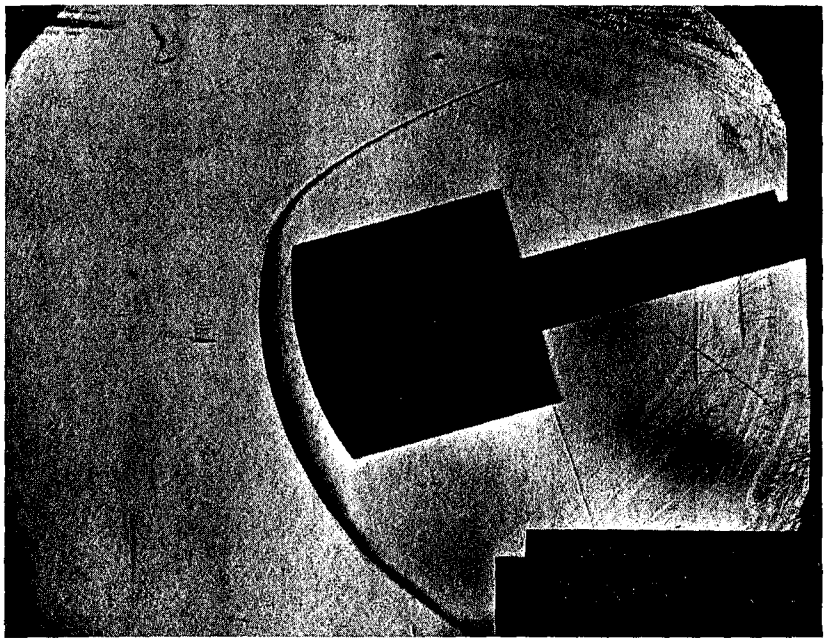

FIG. 44

SCHLIEREN PHOTOGRAPH OF ROUND NOSED BLUNT BODY (R/D = 1.300) AT 16 DEGREES ANGLE OF YAW, M = 5.8.

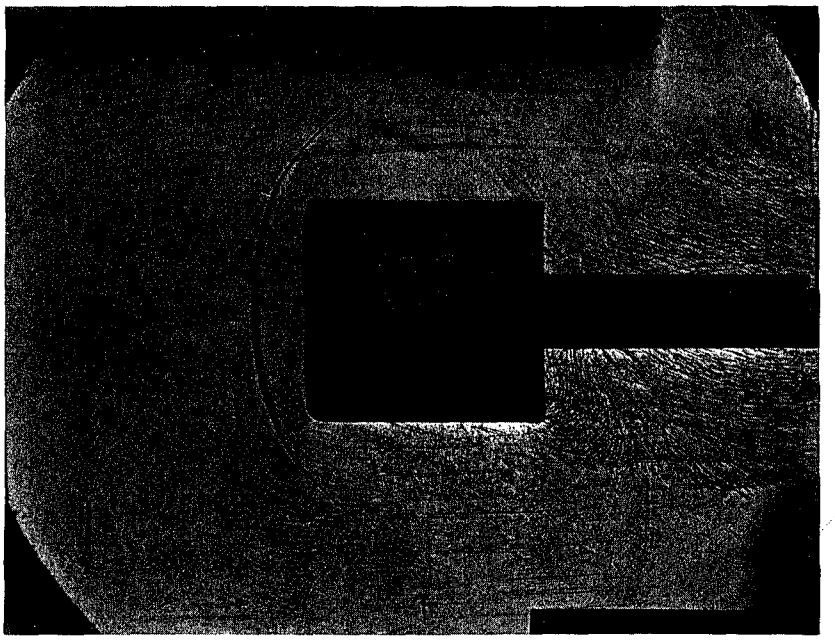

FIG. 45

SCHLIEREN PHOTOGRAPH OF FLAT FACED BLUNT BODY (R/D = ∞) WITH 1/8 INCH ROUNDED SHOULDER (R/D = 0.083) AT ZERO DEGREES ANGLE OF YAW, M = 5.8.

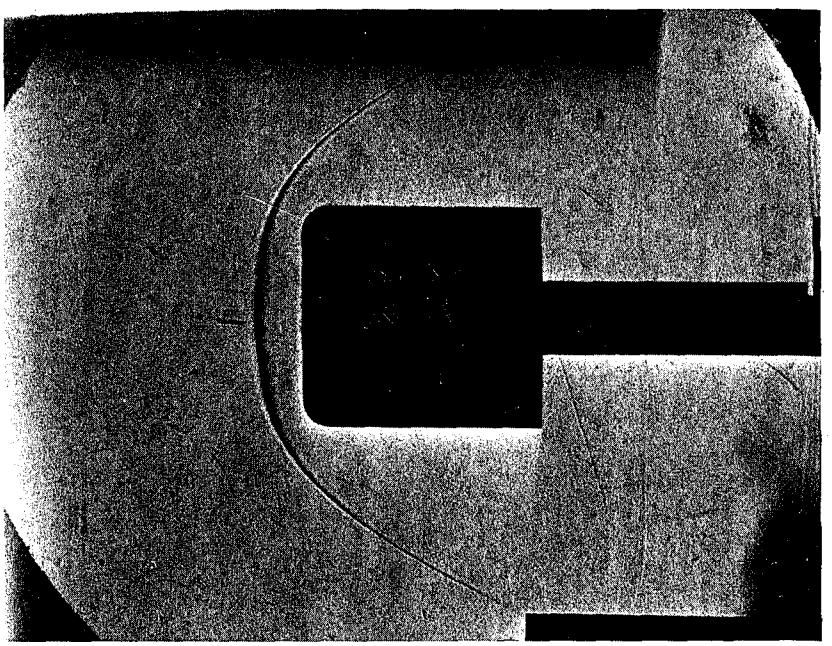

FIG. 46

SCHLIEREN PHOTOGRAPH OF FLAT FACED BLUNT BODY (R/D = ∞) WITH 3/16 INCH ROUNDED SHOULDER (r/D = 0.125) AT ZERO DEGREES ANGLE OF YAW, M = 5.8.

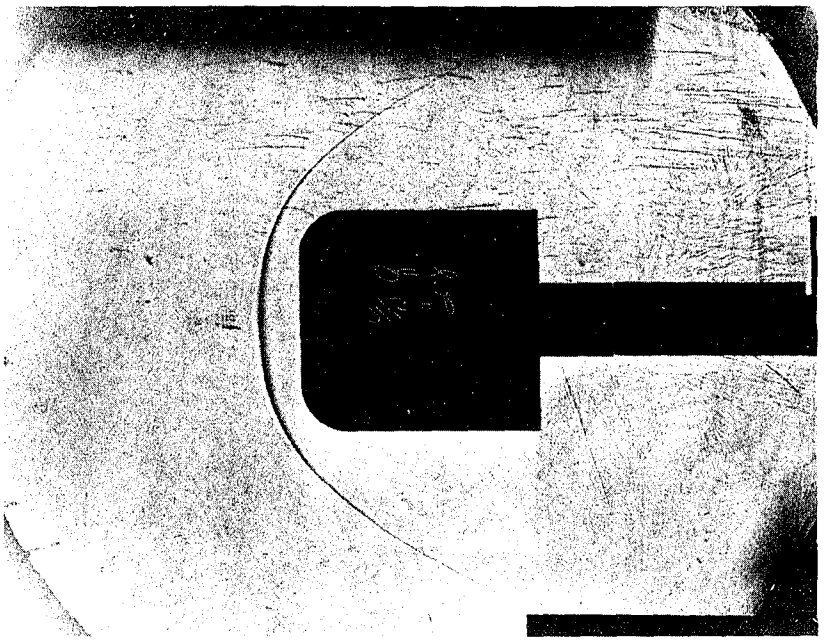

FIG. 47

SCHLIEREN PHOTOGRAPH OF FLAT FACED BLUNT BODY (R/D = ∞) WITH 5/16 INCH ROUNDED SHOULDER (r/D = 0.208) AT ZERO DEGREES ANGLE OF YAW, M = 5.8.

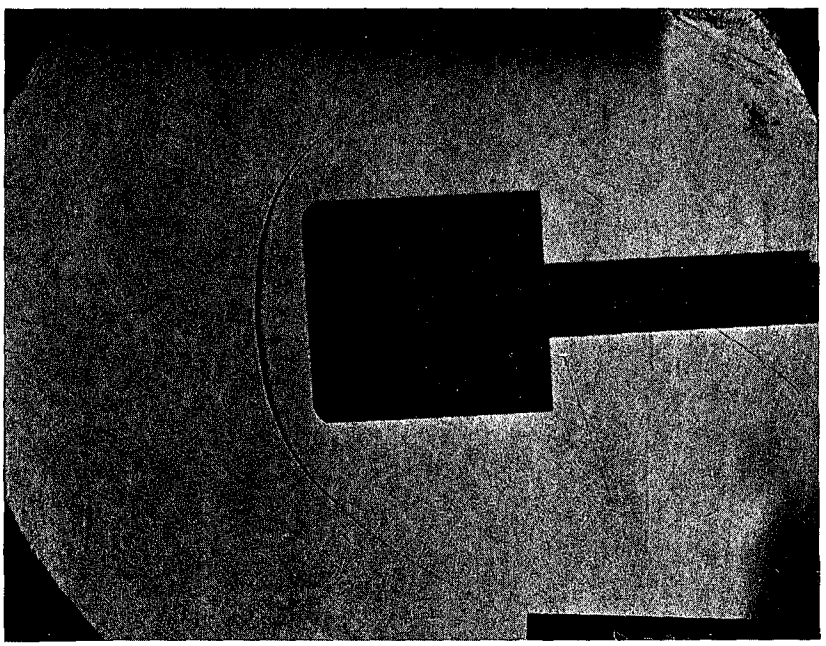

FIG. 48

SCHLIEREN PHOTOGRAPH OF FLAT FACED BLUNT BODY (R/D = ∞) WITH 1/8 INCH ROUNDED SHOULDER (r/D = 0.083) AT 4 DEGREES ANGLE OF YAW, M = 5.8.

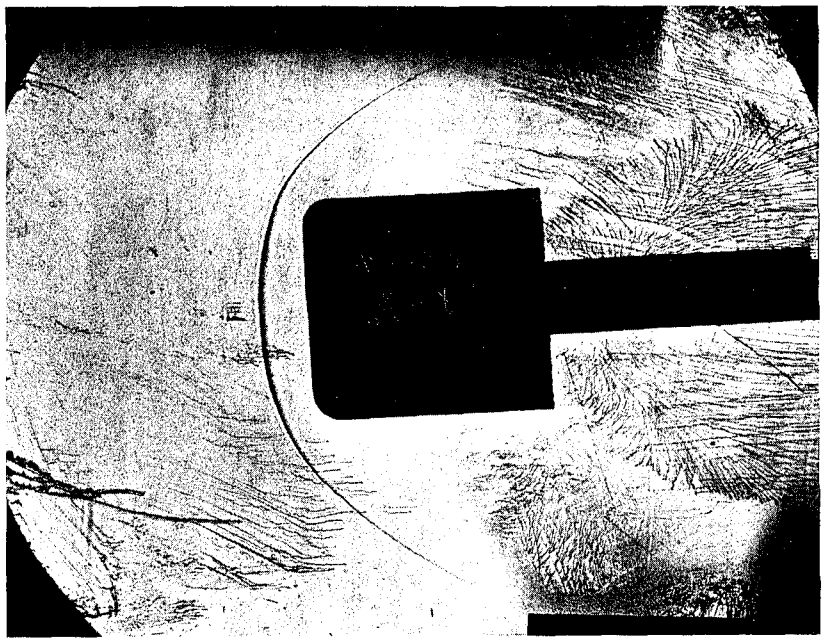

FIG. 49

SCHLIEREN PHOTOGRAPH OF FLAT FACED BLUNT BODY
(R/D = ∞) WITH 3/16 INCH ROUNDED SHOULDER (r/D = 0.125)
AT 4 DEGREES ANGLE OF YAW, M = 5.8.

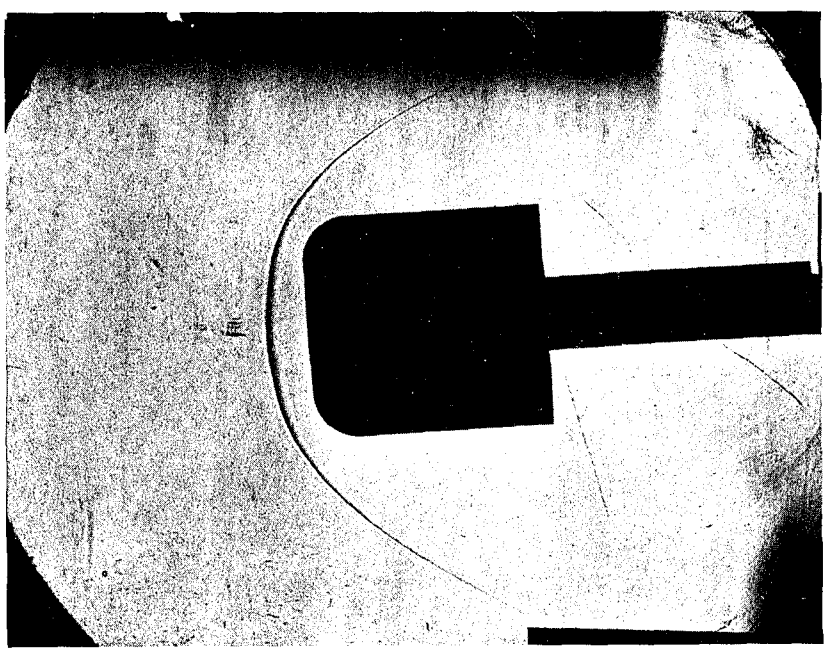

FIG. 50

SCHLIEREN PHOTOGRAPH OF FLAT FACED BLUNT BODY
(R/D = ∞) WITH 5/16 INCH ROUNDED SHOULDER (r/D = 0.208)
AT 4 DEGREES ANGLE OF YAW, M = 5.8.

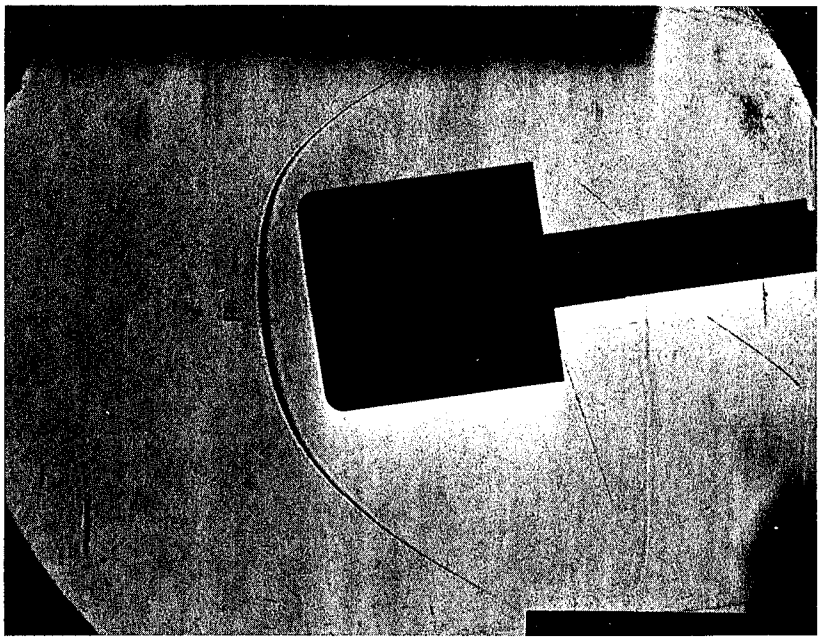

FIG. 51

SCHLIEREN PHOTOGRAPH OF FLAT FACED BLUNT BODY ($R/D = \infty$) WITH 1/8 INCH ROUNDED SHOULDER ($r/D = 0.083$) AT 8 DEGREES ANGLE OF YAW, $M = 5.8$.

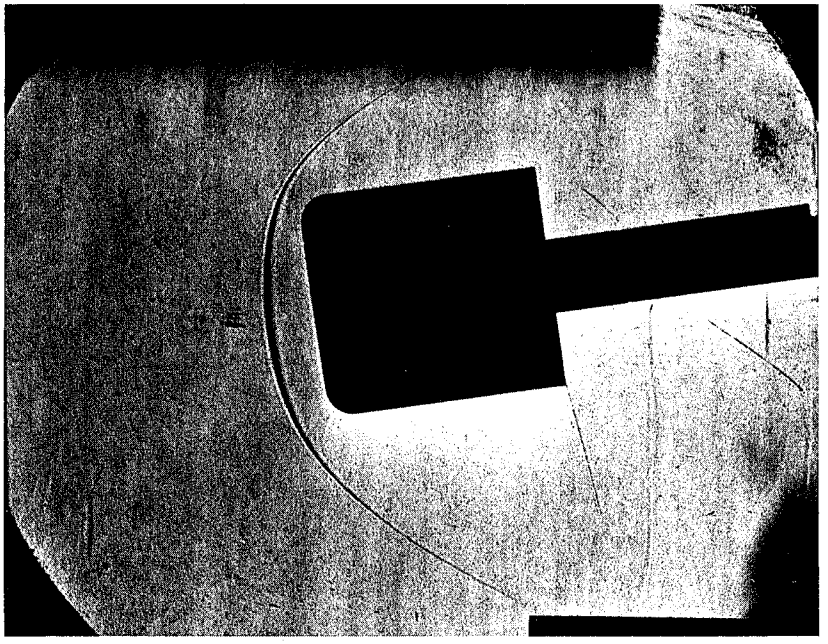

FIG. 52

SCHLIEREN PHOTOGRAPH OF FLAT FACED BLUNT BODY ($R/D = \infty$) WITH 3/16 INCH ROUNDED SHOULDER ($r/D = 0.125$) AT 8 DEGREES ANGLE OF YAW, $M = 5.8$.

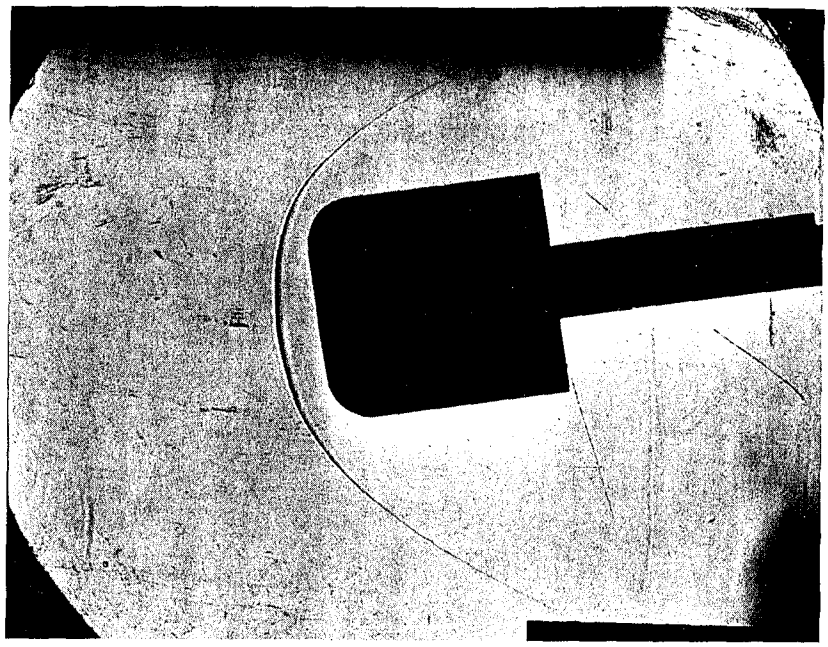

FIG. 53

SCHLIEREN PHOTOGRAPH OF FLAT FACED BLUNT BODY ($R/D = \infty$) WITH 5/16 INCH ROUNDED SHOULDER ($r/D = 0.208$) AT 8 DEGREES ANGLE OF YAW, $M = 5.8$.

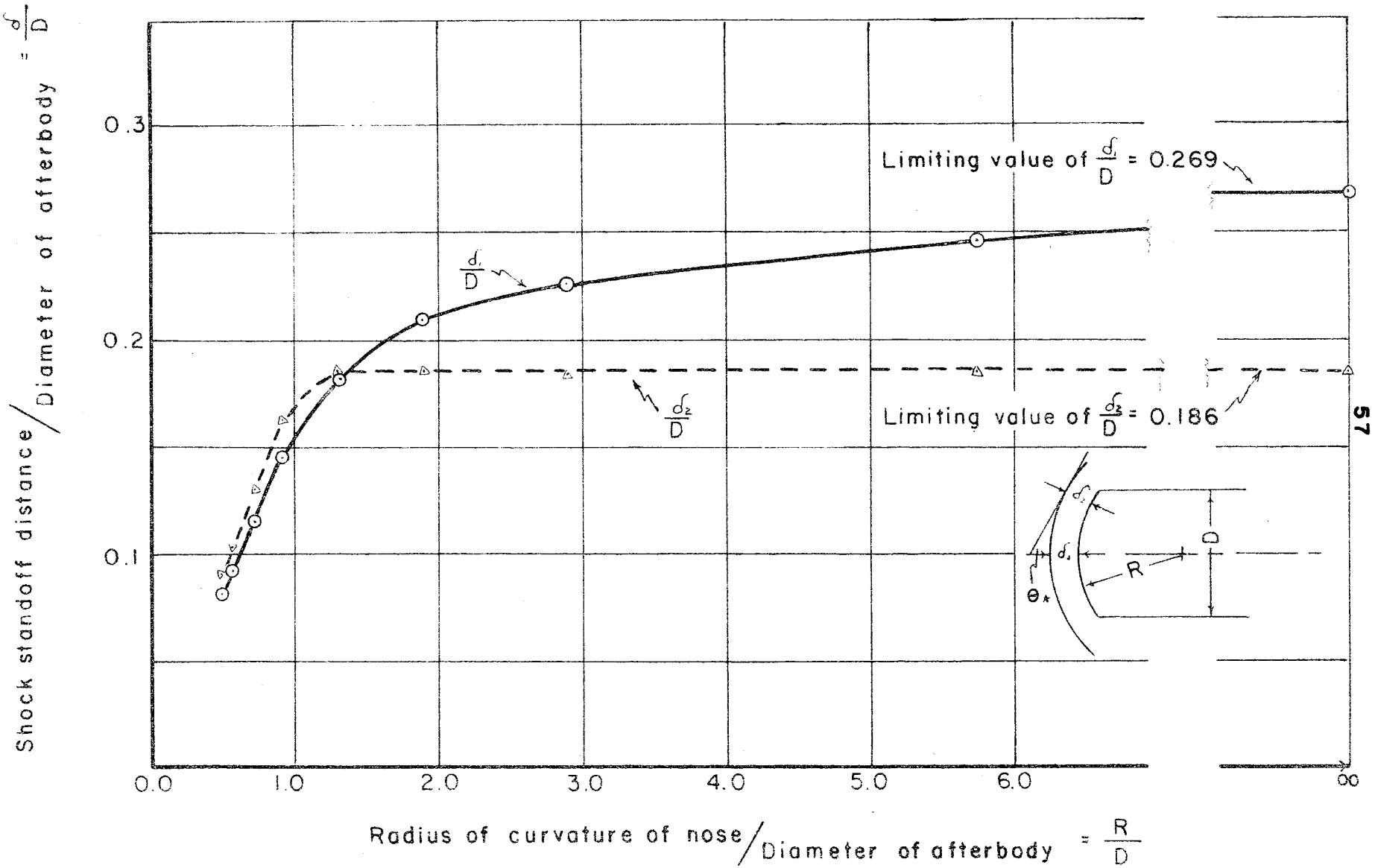

FIG. [illegible] SHOCK STANDOFF DISTANCE vs. NOSE RADIUS

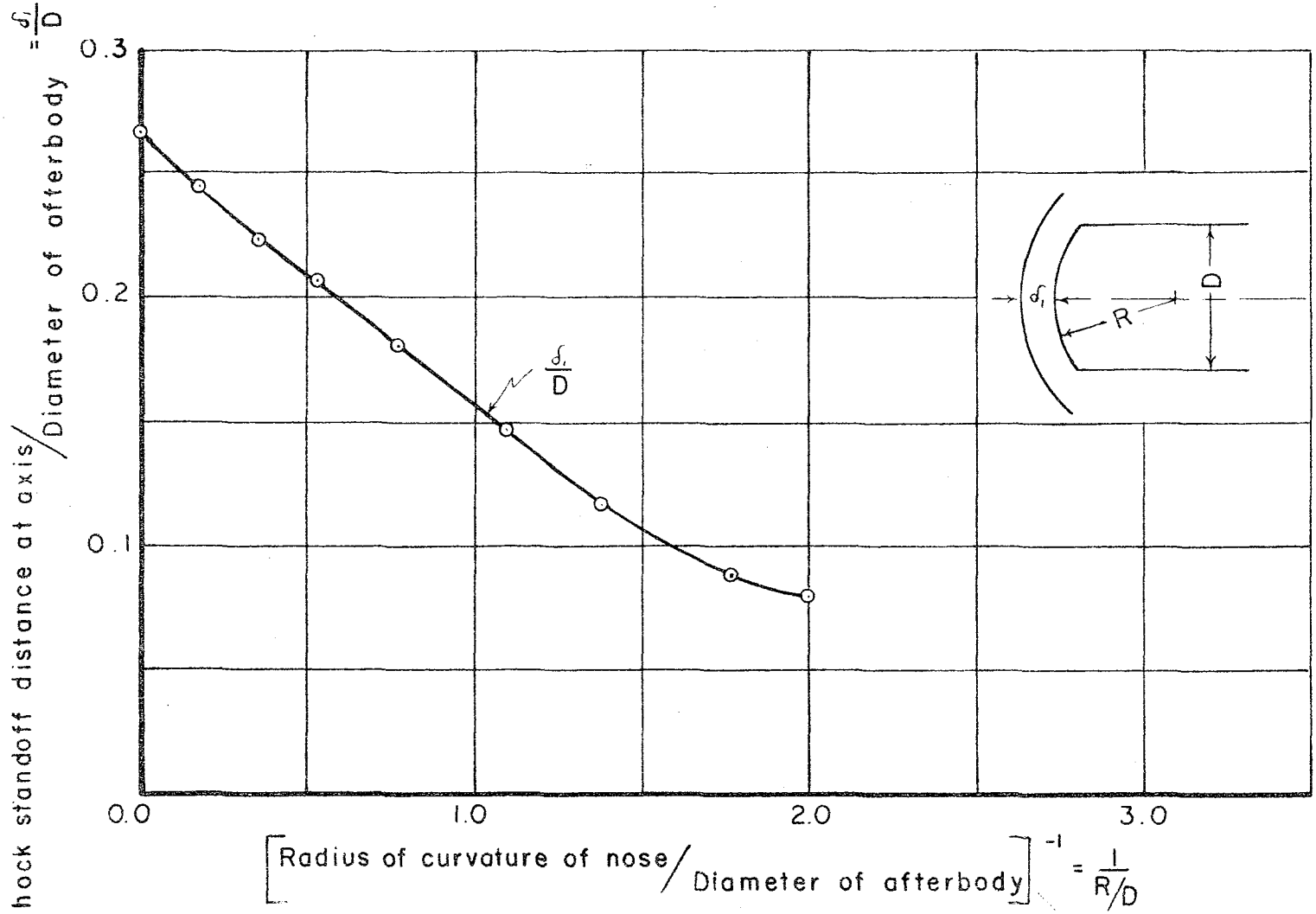

FIG.55. SHOCK STANDOFF DISTANCE vs. RECIPROCAL OF NOSE RADIUS

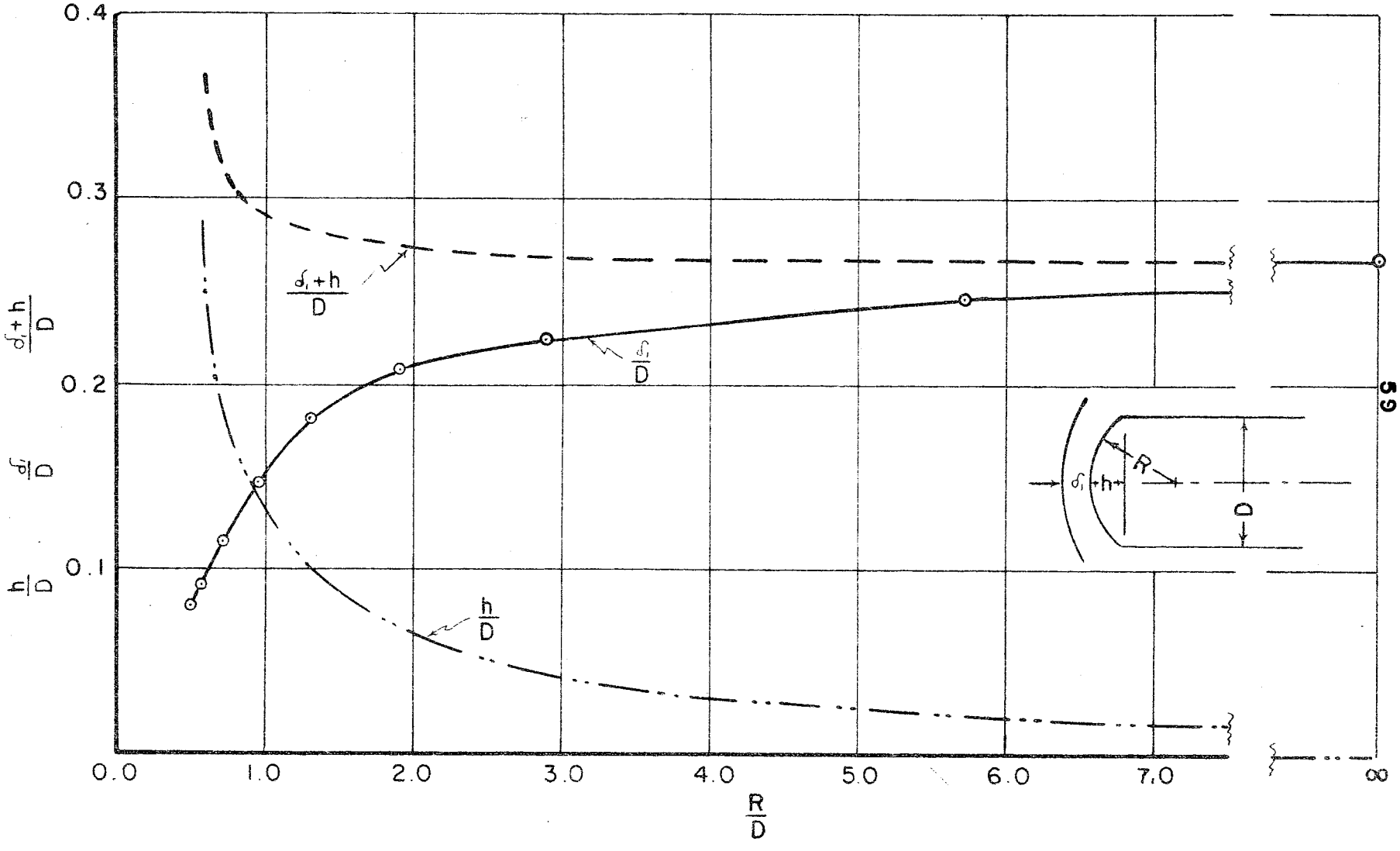

FIG. 53. EFFECT OF ADDING STANDOFF DISTANCE TO NOSE RISE

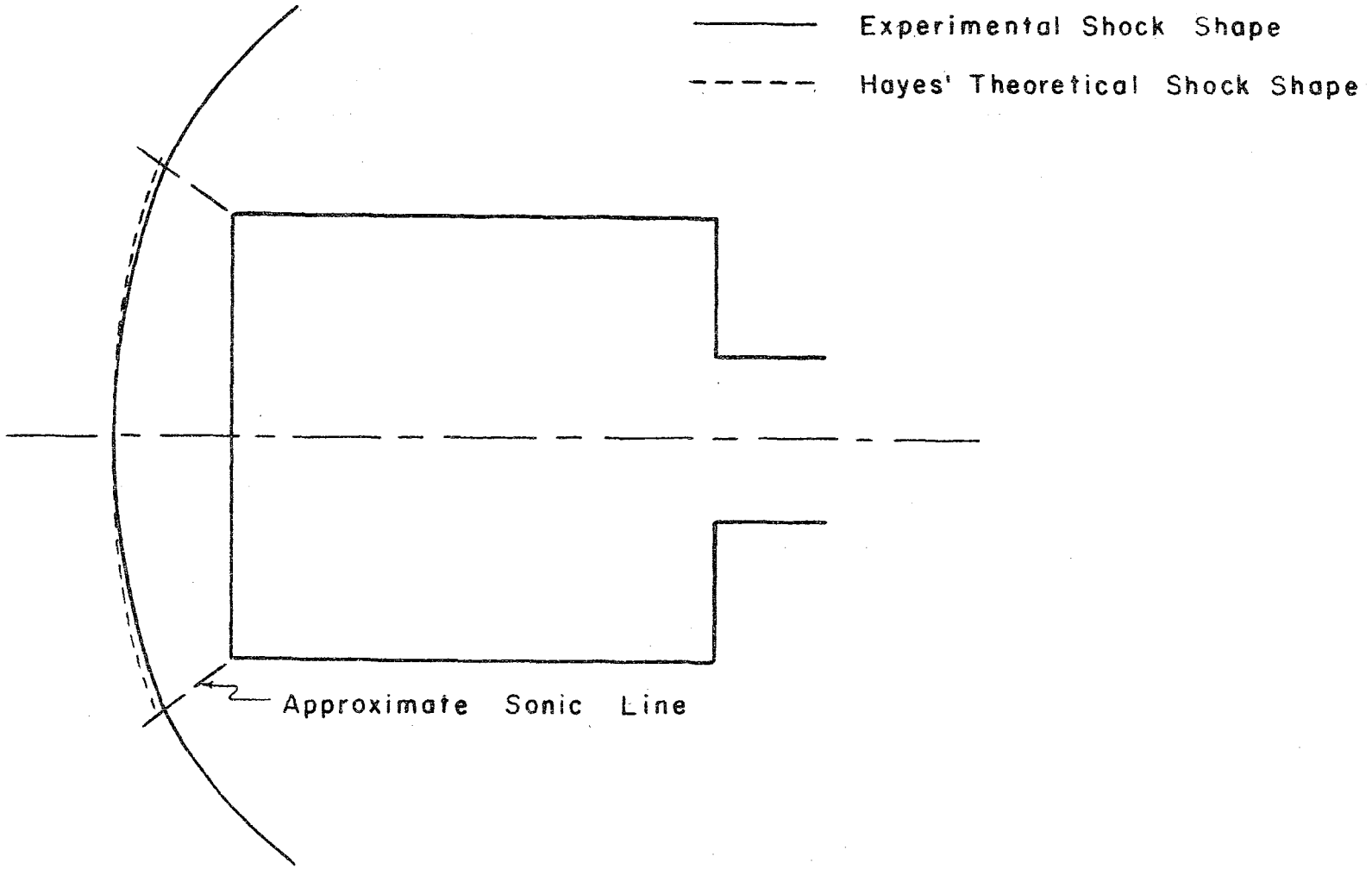

FIG. 58. COMPARISON OF EXPERIMENTAL SHOCK SHAPE WITH HAYES' THEORETICAL APPROXIMATION, $R/D = \infty$, $\alpha = 0$.

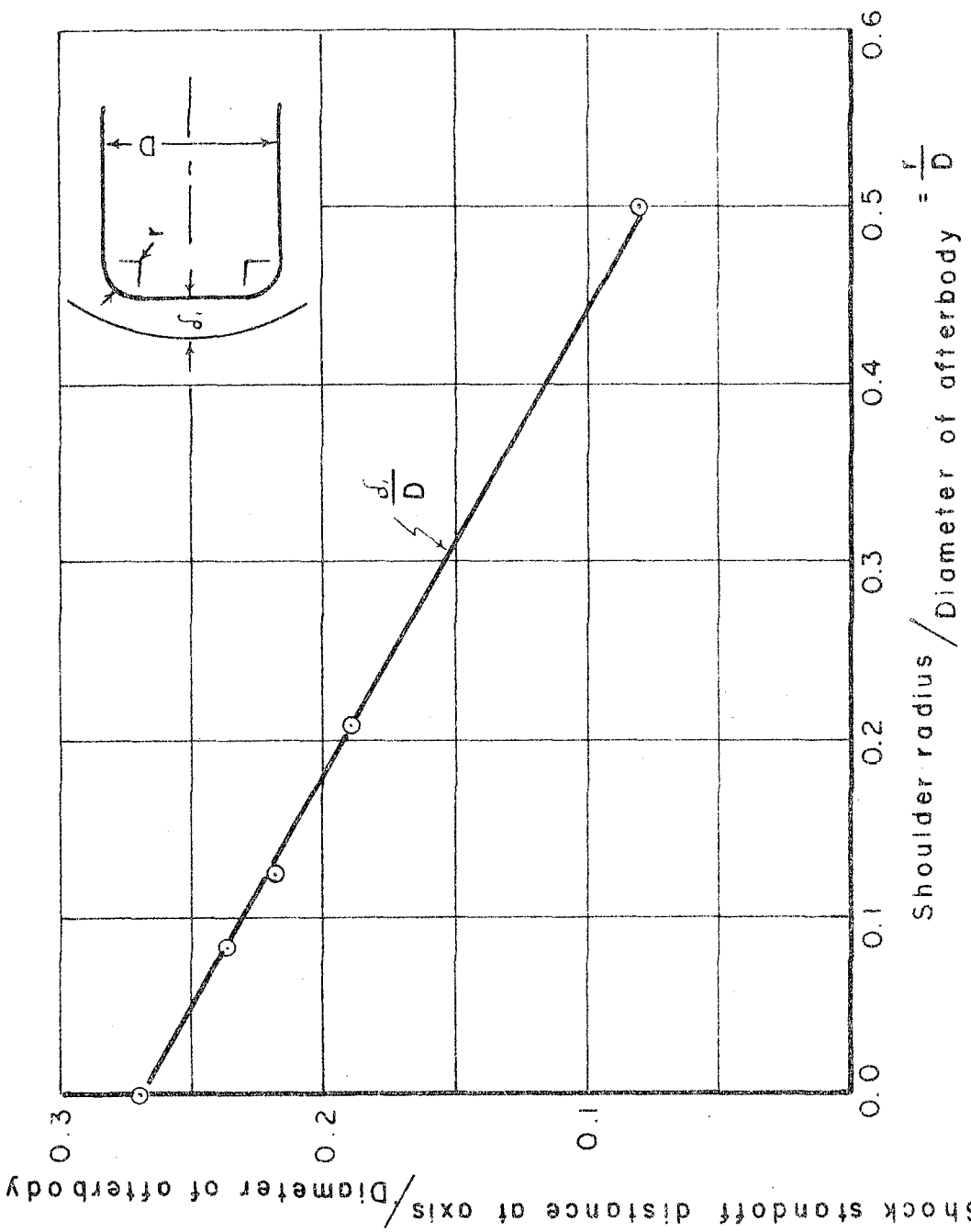

FIG. SHOCK STANDOFF DISTANCE vs. SHOULDER RADIUS

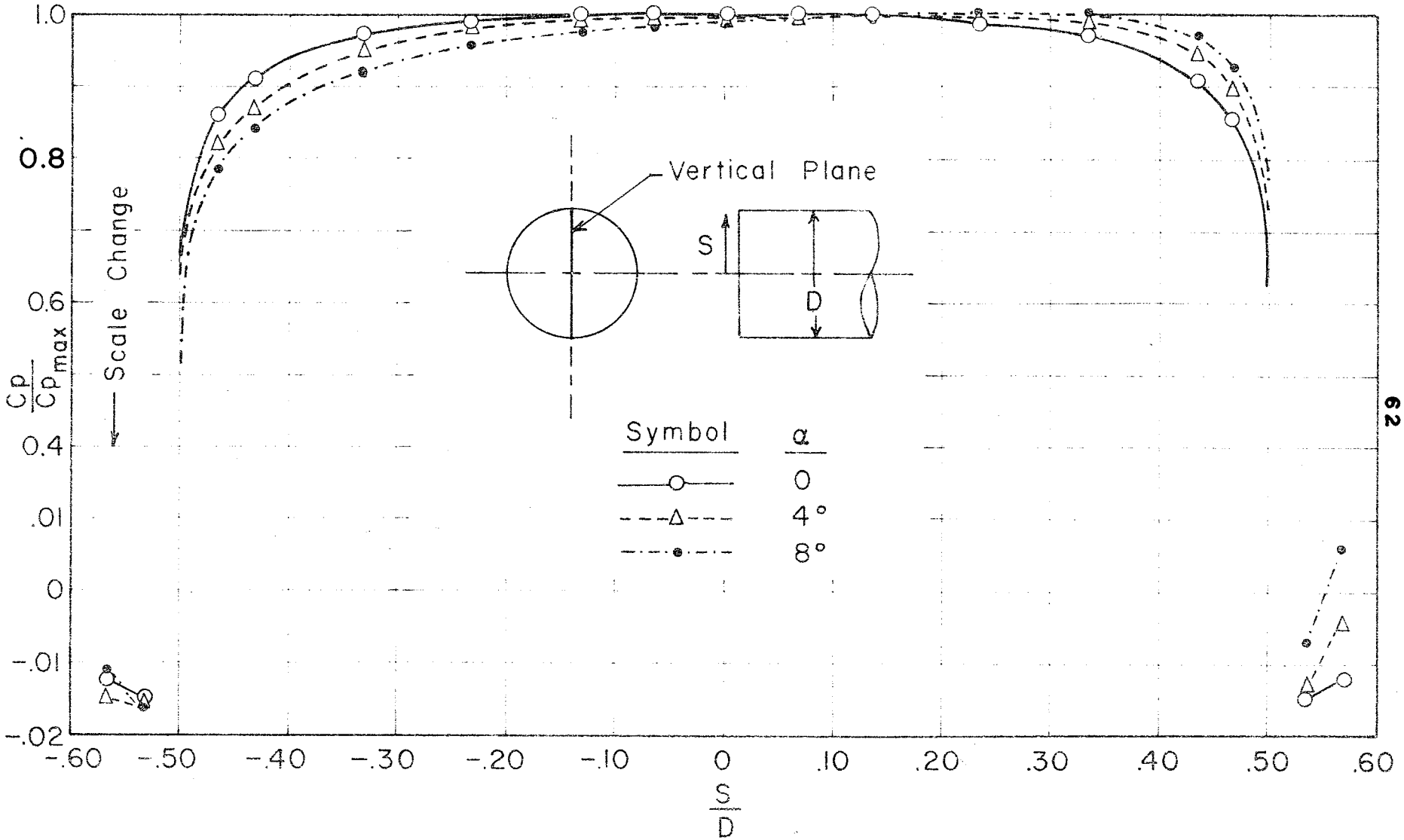

FIG. 59. SURFACE PRESSURE, VERTICAL PLANE, $\frac{R}{D} = \infty$, $\alpha = 0, 4°, 8°$

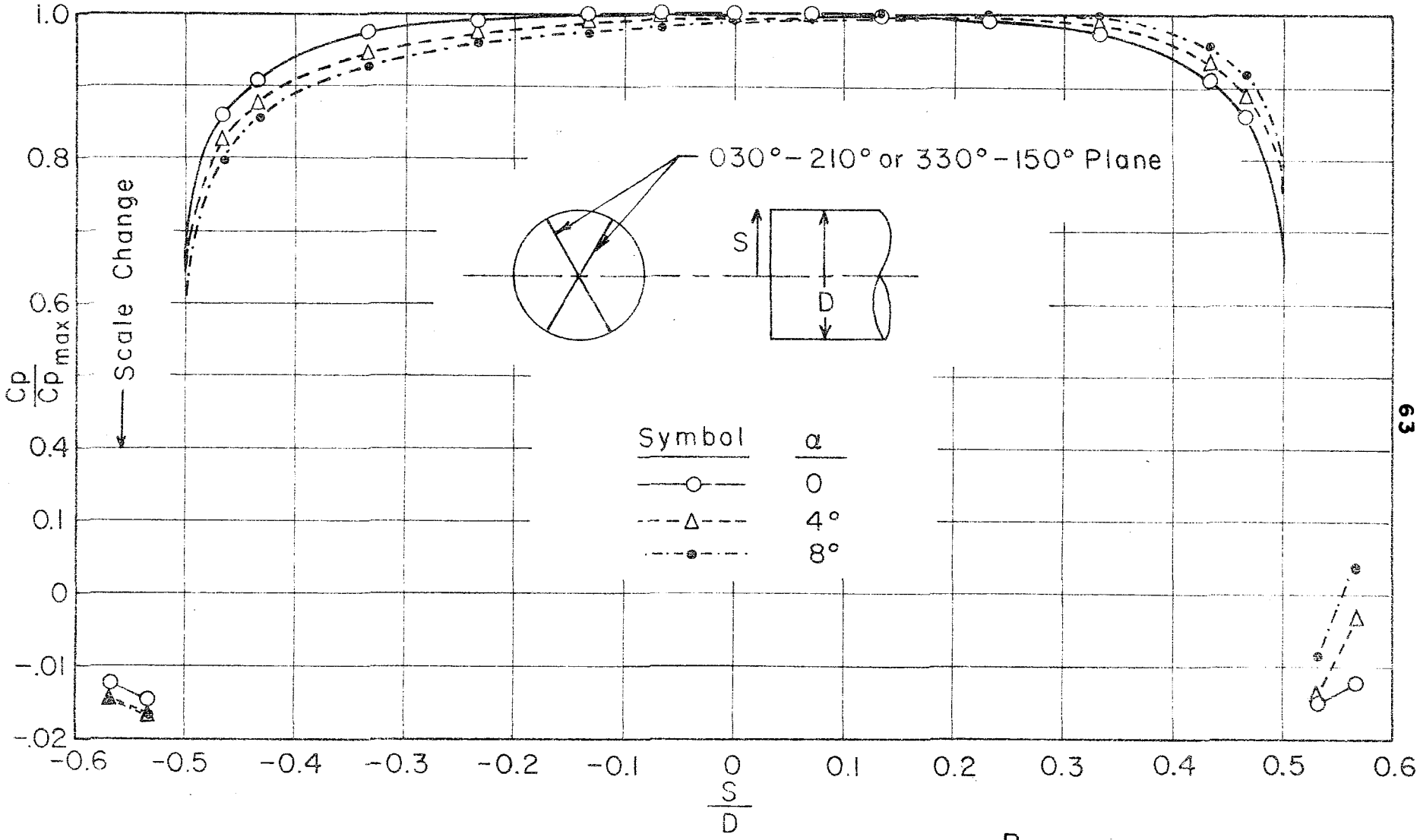

FIG. 60. SURFACE PRESSURE 030°-210° PLANE, $\frac{R}{D} = \infty$, $\alpha = 0, 4°, 8°$.

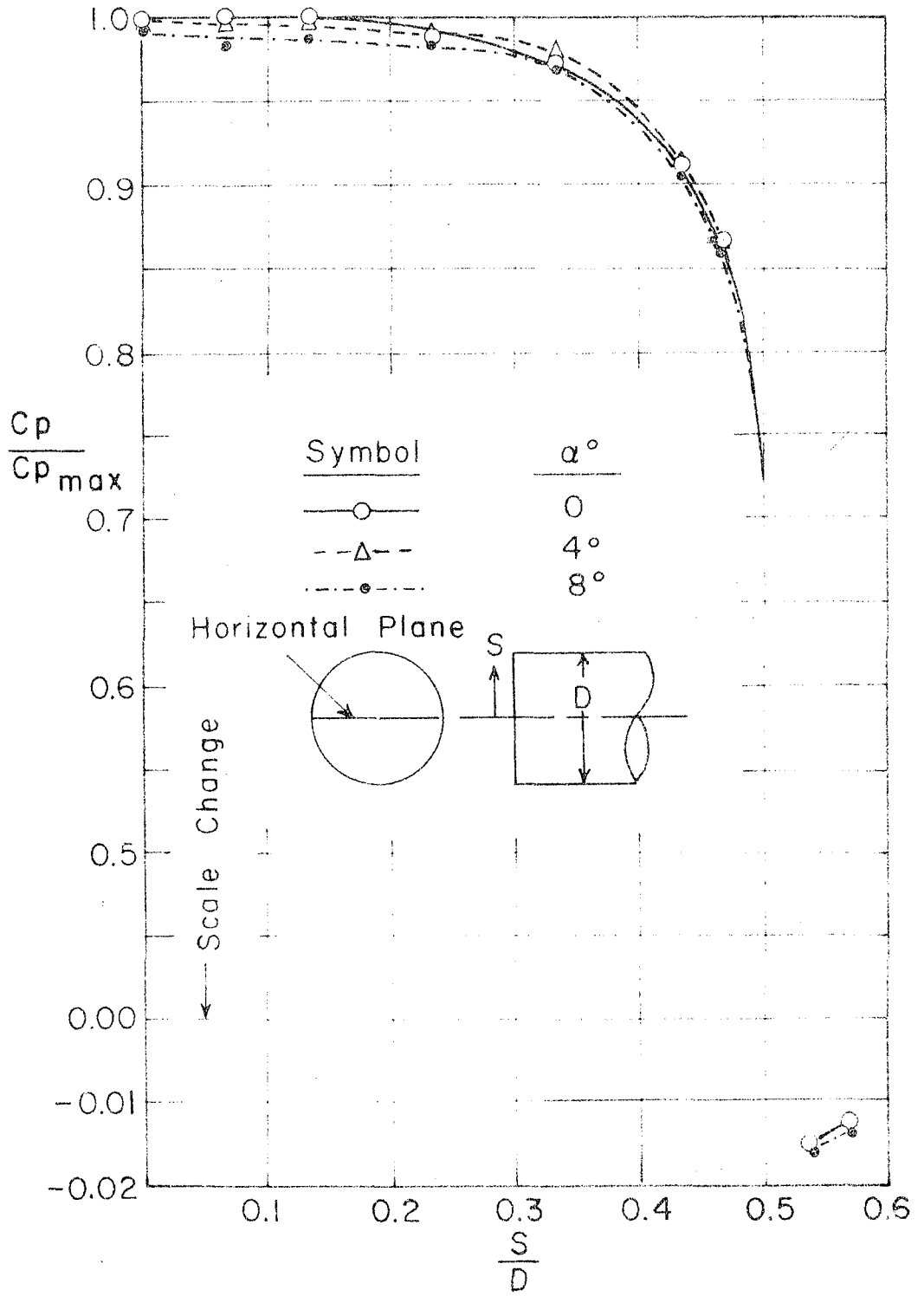

FIG. 1. SURFACE PRESSURES, HORIZONTAL PLANE, R/D = ∞, α = 0°, 4° & 8°.

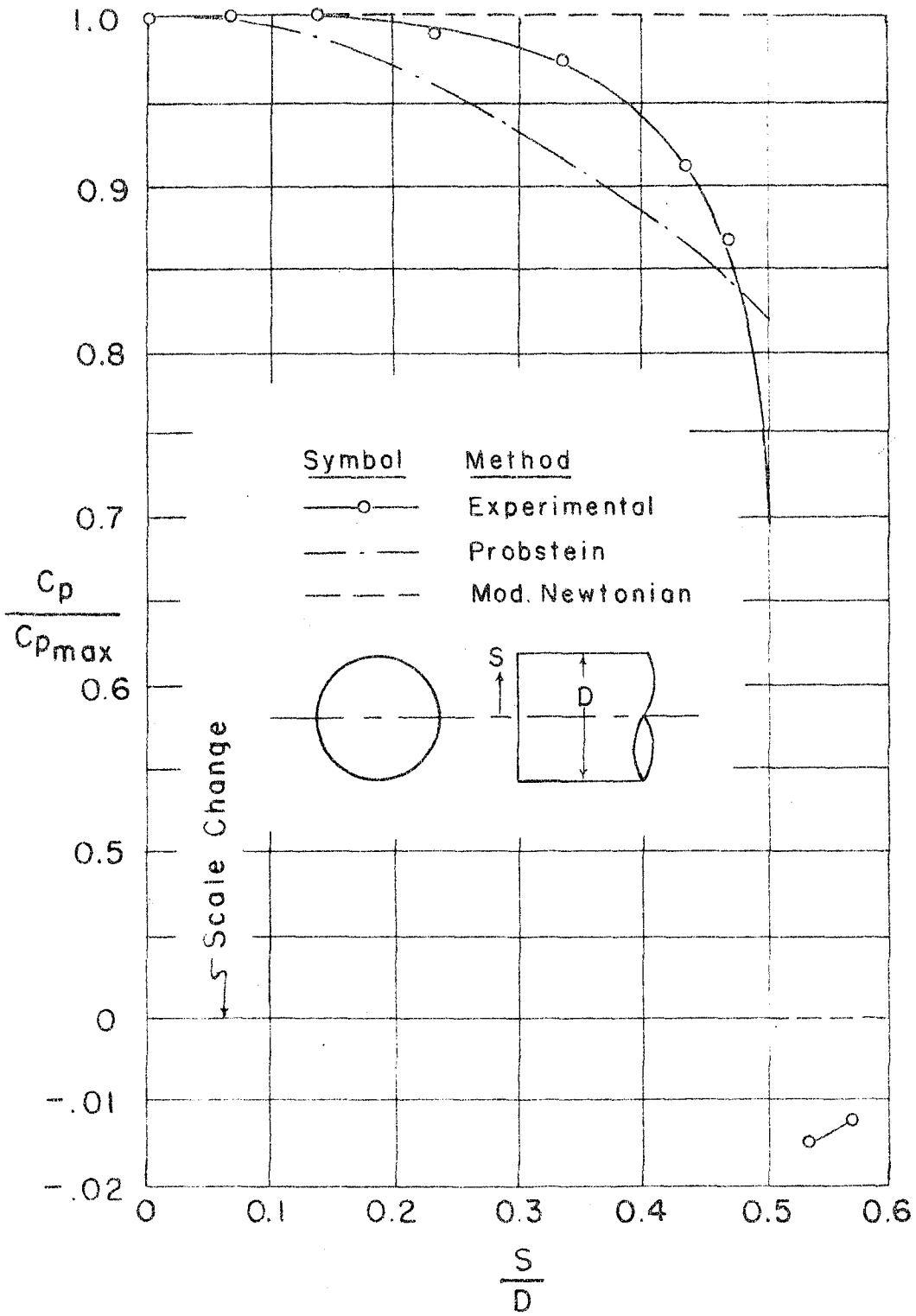

FIG. [illegible] COMPARISON OF EXPERIMENTAL SURFACE PRESSURE DISTRIBUTION WITH THEORETICAL APPROXIMATIONS, $R/D = \infty$, $\alpha = 0$.

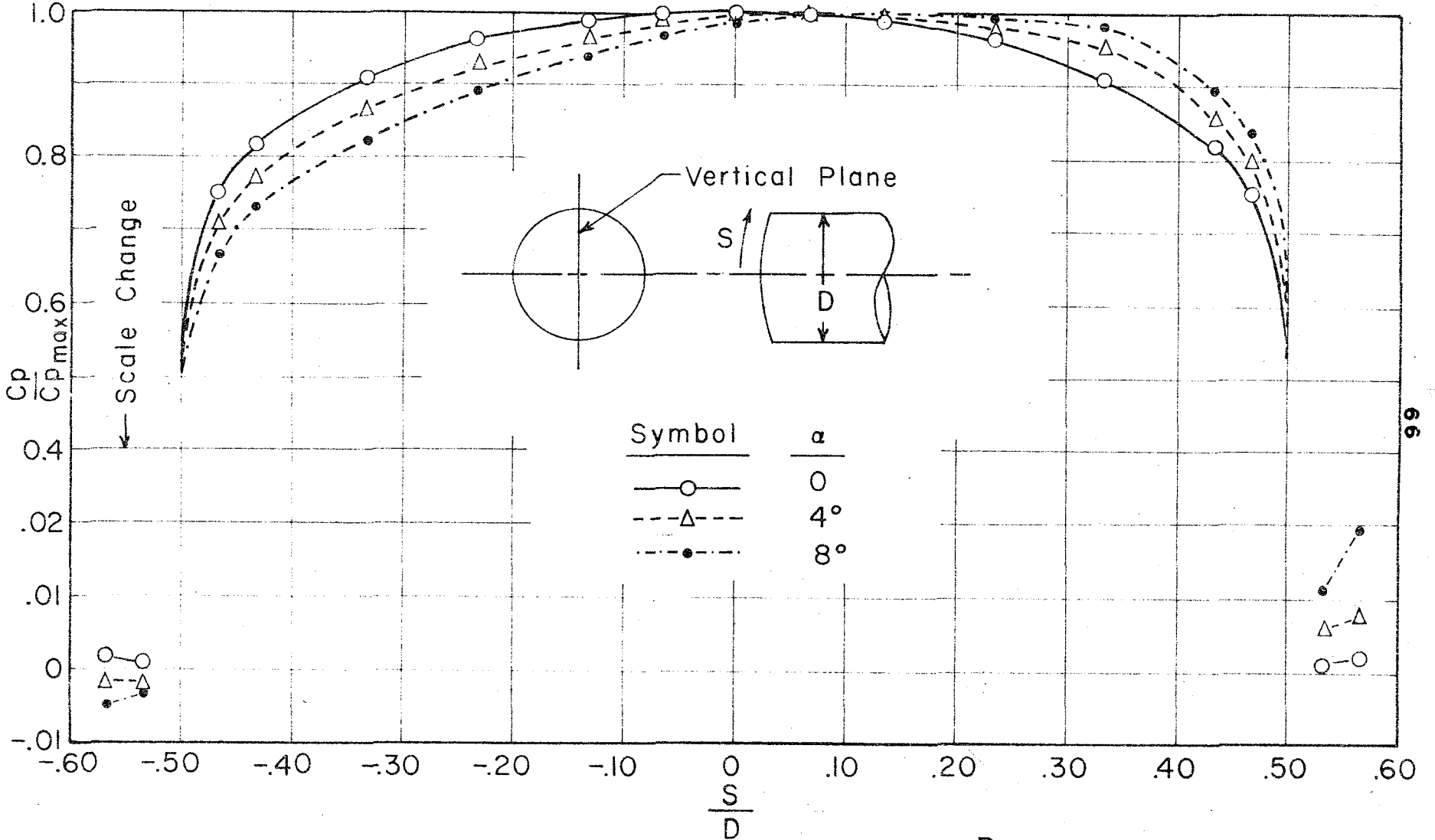

FIG. 63. SURFACE PRESSURE, VERTICAL PLANE, $\frac{R}{D} = 1.3$, $\alpha = 0, 4°, 8°$

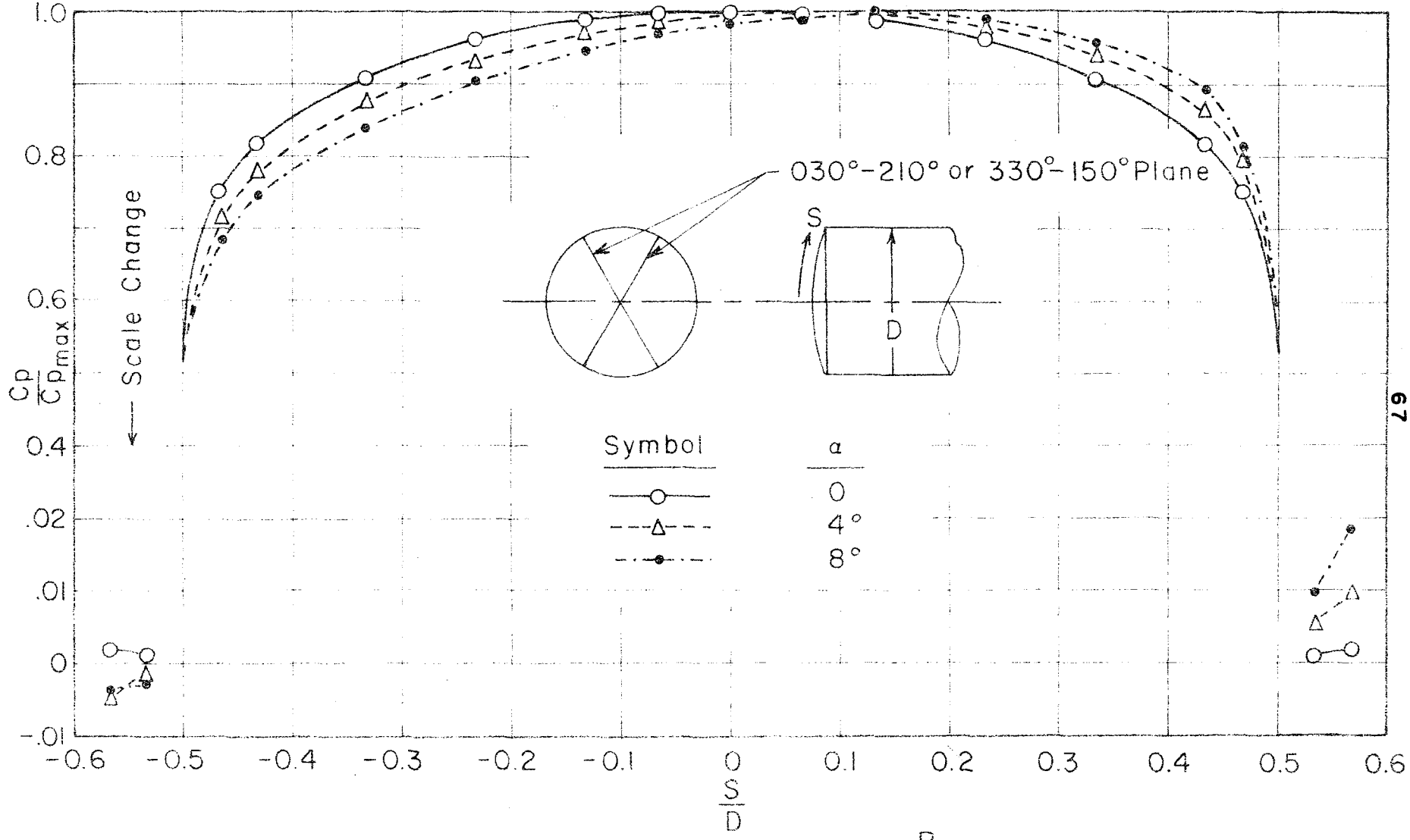

FIG. 4. SURFACE PRESSURES 030° - 210°, $\frac{R}{D} = 1.30$, $\alpha = 0, 4°, 8°$

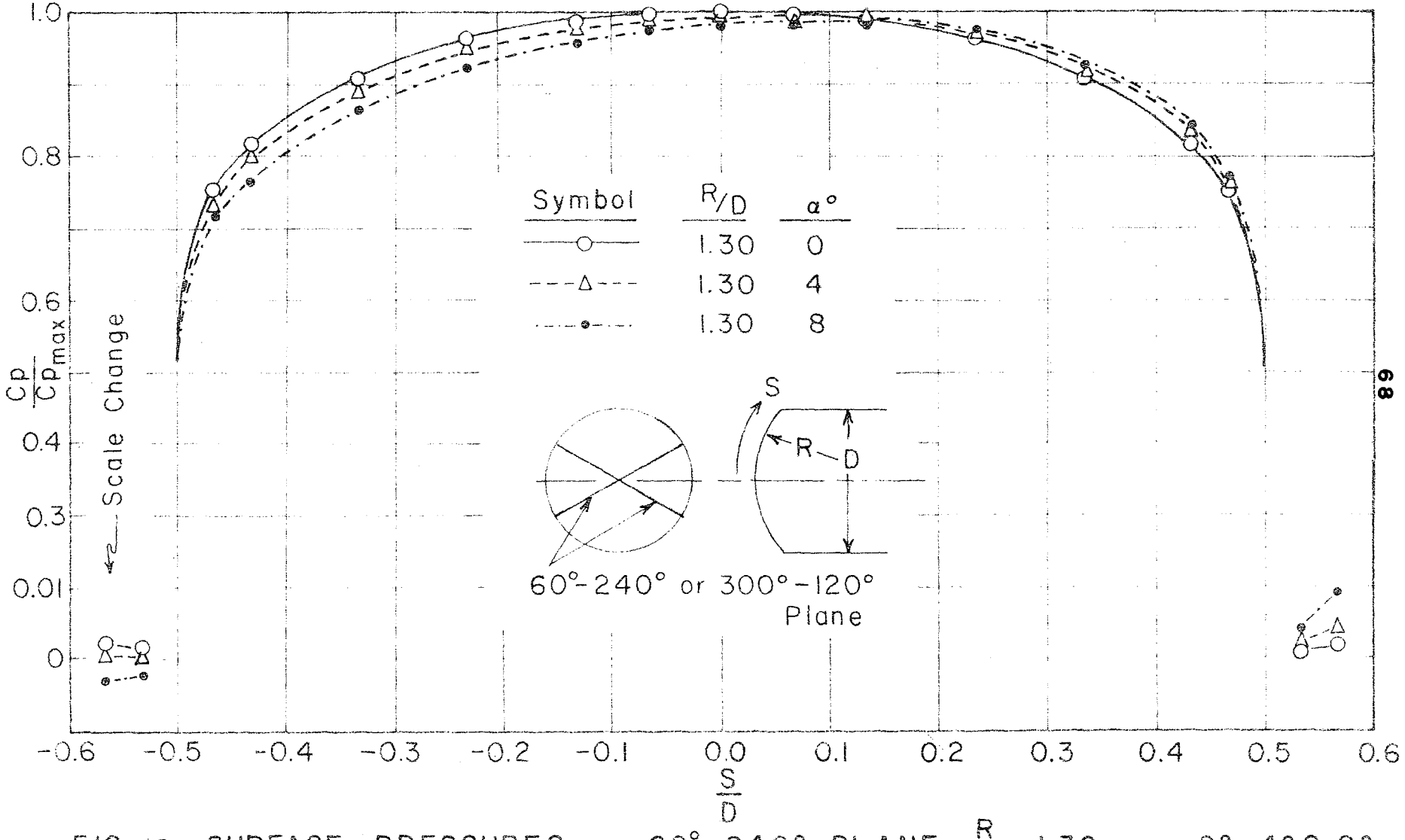

FIG. 55. SURFACE PRESSURES, 60°-240° PLANE, $\frac{R}{D}$ = 1.30, α = 0°, 4° & 8°

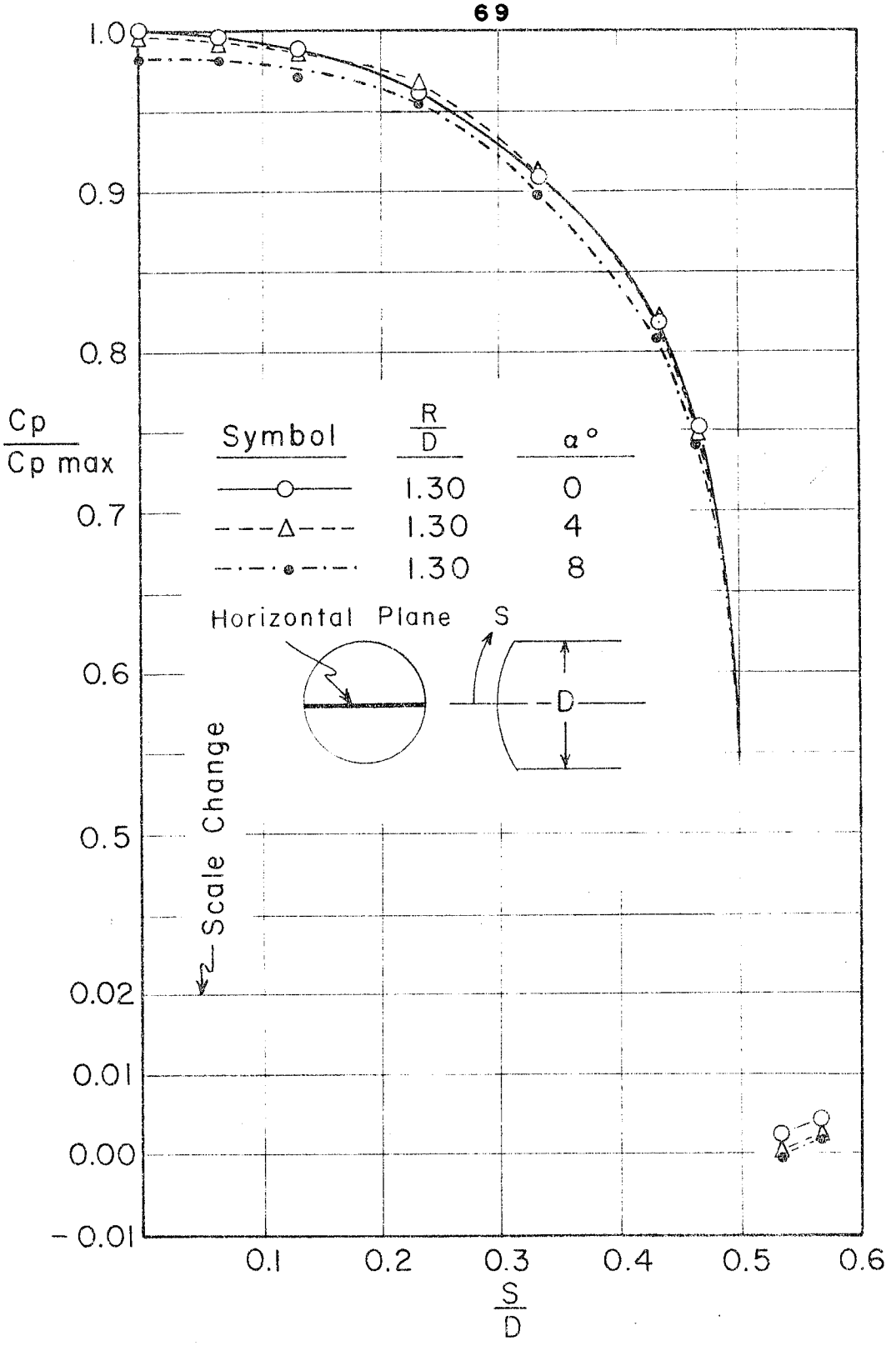

FIG. 38. SURFACE PRESSURE, HORIZONTAL PLANE, R/D = 1.30, α = 0°, 4° & 8°

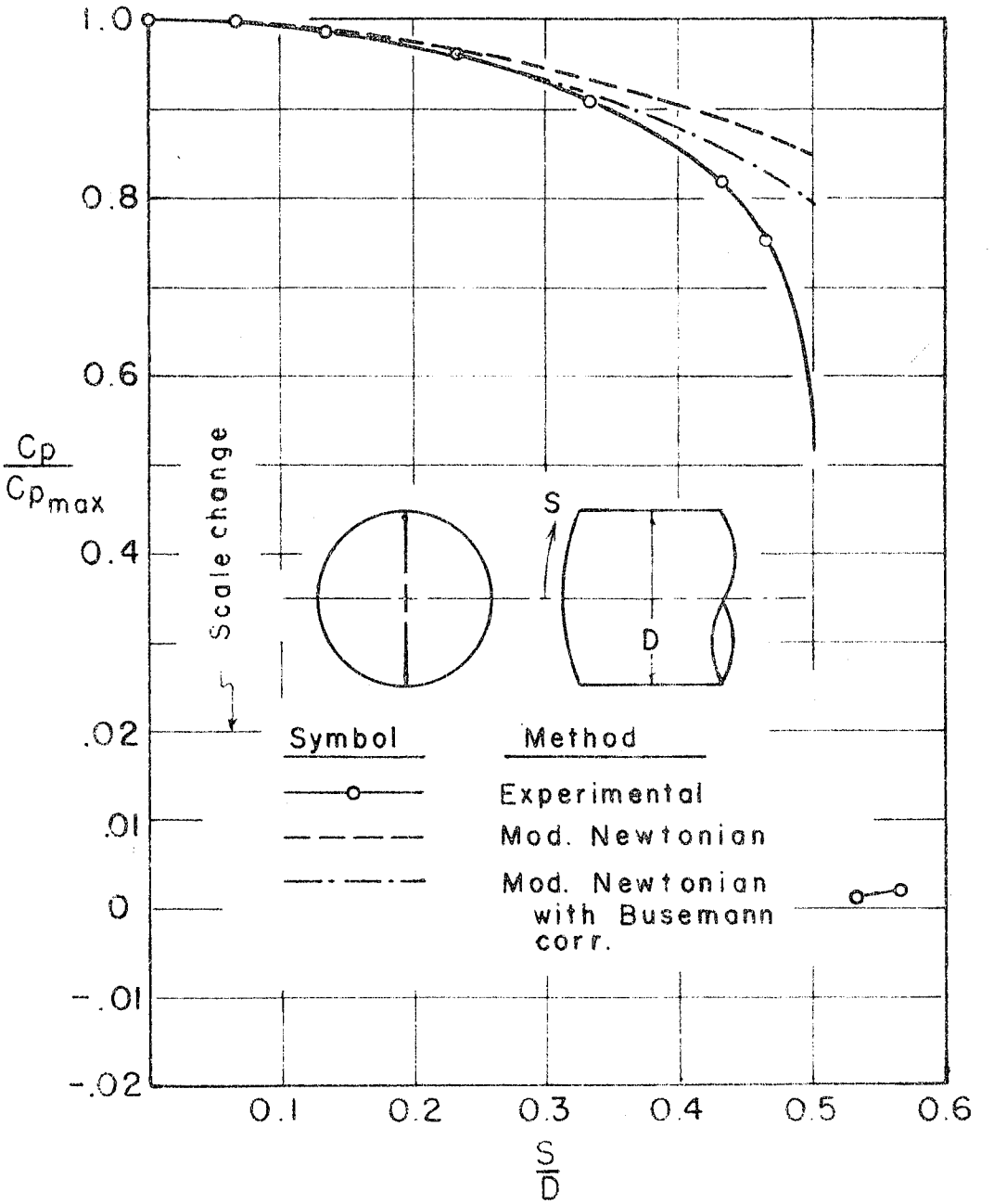

FIG. . COMPARISON OF EXPERIMENTAL SURFACE PRESSURE DISTRIBUTION WITH THEORETICAL APPROXIMATIONS, $\frac{R}{D}$ = 1.30, α = 0.

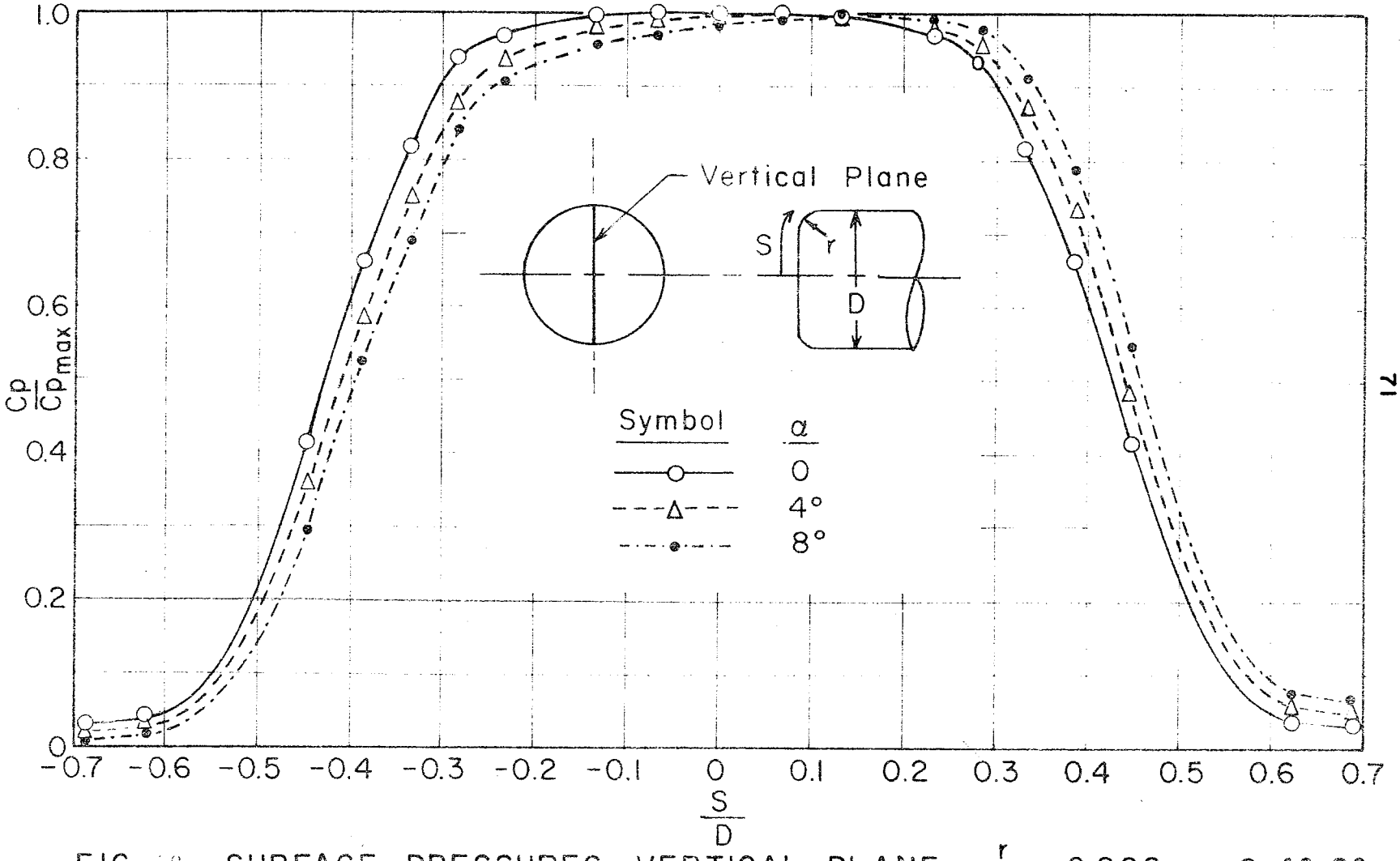

FIG. 68. SURFACE PRESSURES, VERTICAL PLANE, $\frac{r}{D} = 0.208, \alpha = 0, 4°, 8°$.

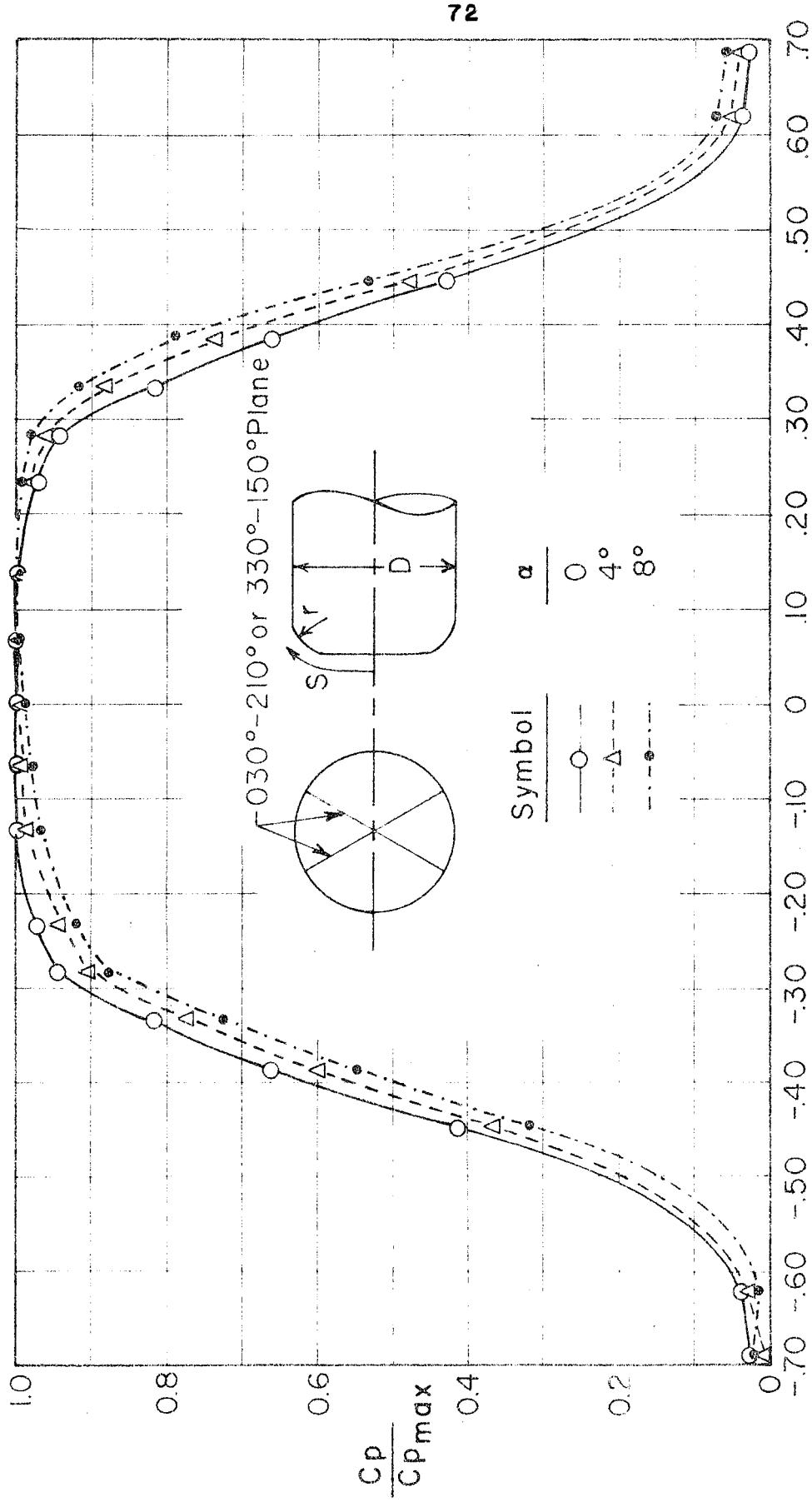

FIG. 49. SURFACE PRESSURES 030°-210° PLANE, $\frac{R}{D}$, $\alpha = 0, 4°, 8°$

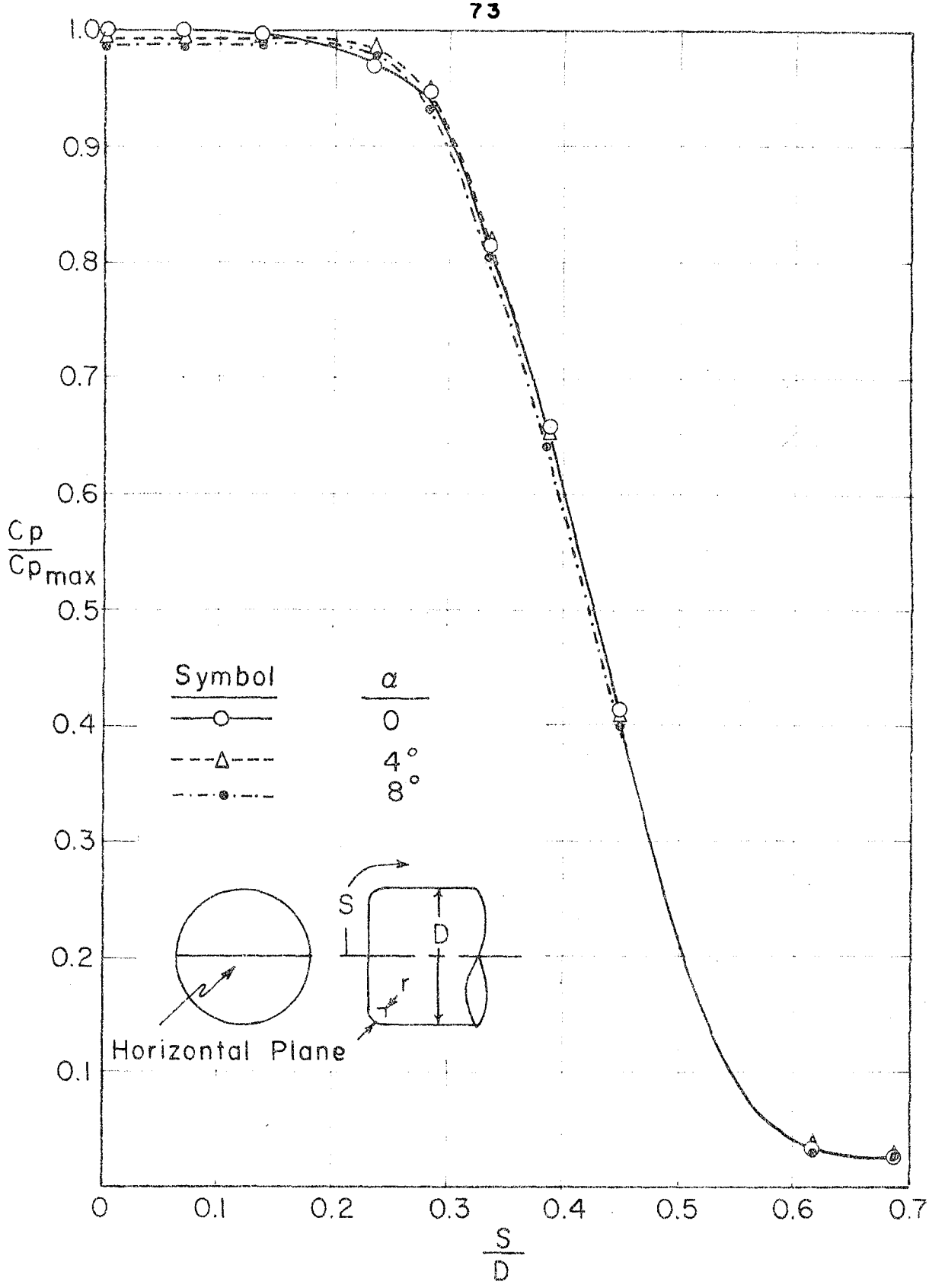

FIG. 70. SURFACE PRESSURES, HORIZONTAL PLANE, $\frac{R}{D} = \infty$, $\frac{r}{D} = 0.208$, $\alpha = 0°, 4°, 8°$.

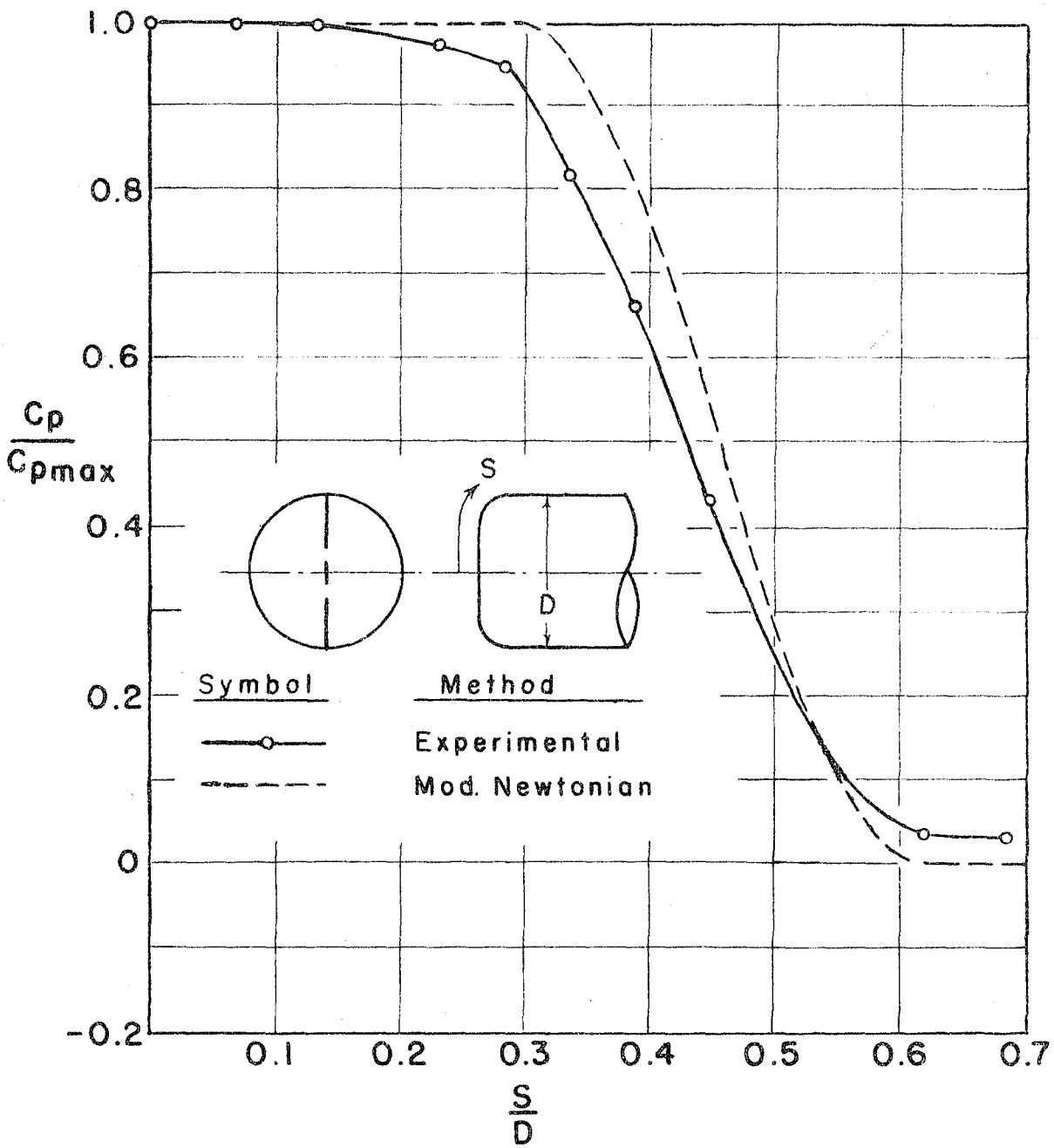

FIG. 71. COMPARISON OF EXPERIMENTAL SURFACE PRESSURE DISTRIBUTION WITH THEORETICAL APPROXIMATIONS, $r/D = 0.208$, $\alpha = 0$.

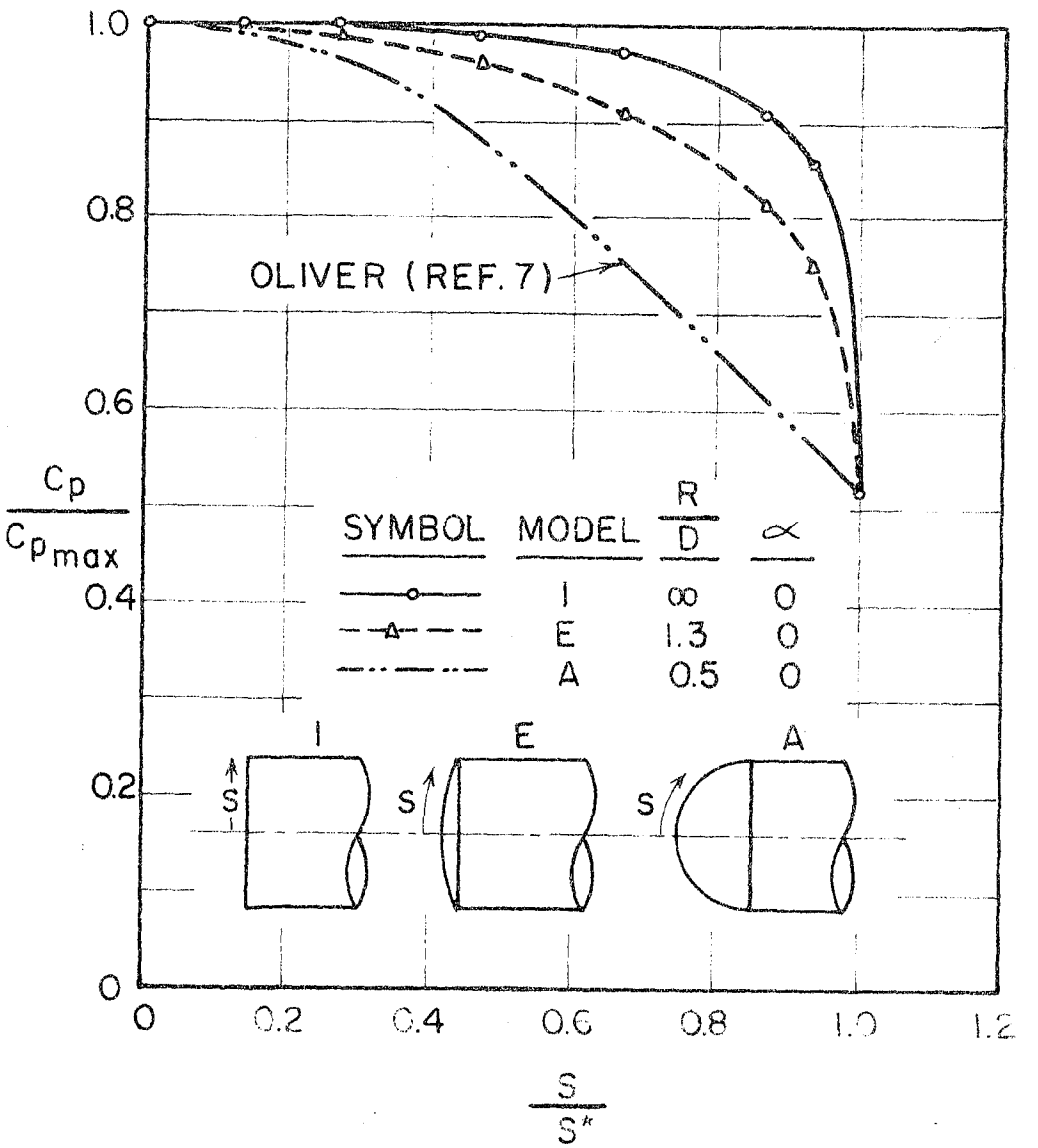

FIG. 72. COMPARISON OF SURFACE PRESSURE DISTRIBUTIONS ON SEVERAL BLUNT NOSED BODIES, M = 5.8.

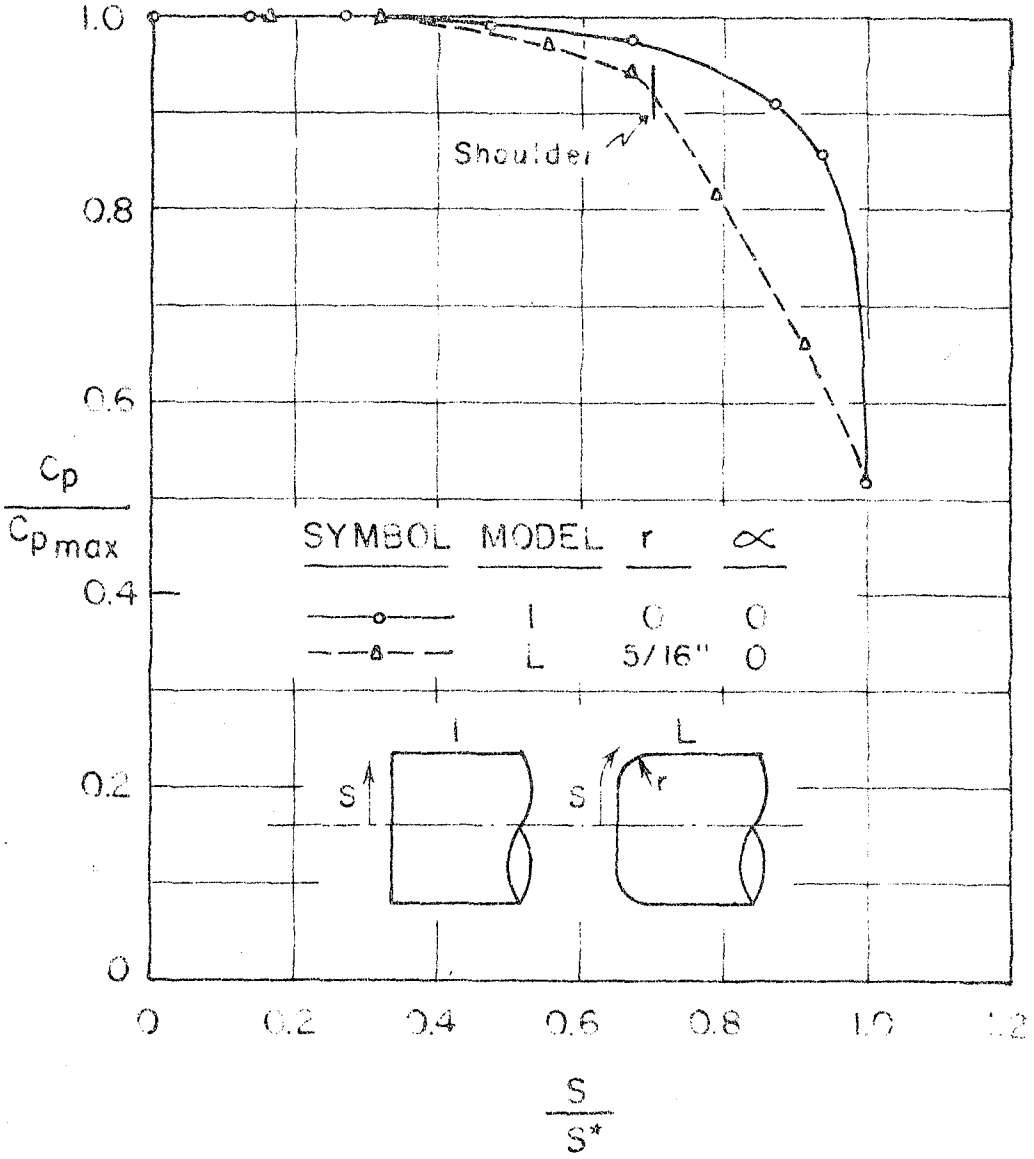

FIG. 13. COMPARISON OF SURFACE PRESSURE DISTRIBUTIONS SHOWING EFFECT OF ROUNDED SHOULDER.